THE ROLE OF URED IN NICKEL UREASE MATURATION AND SPECTROSCOPIC INVESTIGATIONS INTO THE IRON UREASE

By

Mark Anthony Farrugia

A DISSERTATION

Submitted to
Michigan State University
in partial fulfillment of the requirements
for the degree of

Biochemistry and Molecular Biology – Doctor of Philosophy

2015

ABSTRACT

THE ROLE OF URED IN NICKEL UREASE MATURATION AND SPECTROSCOPIC INVESTIGATIONS INTO THE IRON UREASE

By

Mark Anthony Farrugia

Urease catalyzes the hydrolysis of urea into ammonia and carbamic acid, with the latter compound decomposing into a second molecule of ammonia and carbonic acid. The enzyme from *Klebsiella aerogenes* is composed of three subunits (UreA, UreB, and UreG) and assembles into a trimer of heterotrimers $(UreABC)_3$. The *in vivo* formation of its di-nickel, carbamylated lysine-bridged active site requires four accessory proteins: UreD, UreE, UreF, and UreG. The sequential binding of UreD, UreF, and UreG to urease or the binding of an accessory protein complex consisting of UreD:UreF:UreG primes the enzyme for activation by nickel that is delivered by UreE. Two of my projects focused on determining the role of UreD in this activation process and characterizing the properties of a soluble UreD:UreF:UreG accessory protein complex.

I characterized a soluble, urease accessory protein complex containing a translational fusion of the maltose binding protein with UreD (MBP-UreD), UreF, and UreG (termed MBP-UreDFG) that was formed *in vivo*. This complex bound nickel weakly and existed as a dimer of heterotrimers in solution, with two UreF protomers located at the interfacial site. $(MBP\text{-}UreDFG)_2$ dissociated to the heterotrimer as it bound to urease apoprotein or holoenzyme. The interaction with the apoprotein was disrupted by the presence of nickel and $(UreG)_2$ dissociated from $(MBP\text{-}UreDFG)_2$ in buffer containing GTP, magnesium, and nickel.

I used mutagenesis approaches to examine the interaction of UreD with both urease and UreF and to explore the function of this protein in the transfer of nickel into the active site of

urease. On the basis of a multiple sequence alighnment and a UreD homology model I generated from the *Helicobacter pylori* UreH:UreF:UreG crystal structure (UreH is homologous to UreD), 26 residues were selected for substitution. None of the variants were affected in their urease:UreD and UreD:UreF interactions *in vivo*. *In vivo* activation studies using UreD variants produced in the context of the complete urease gene cluster identified the D63A, D63Q, S85K, D142A, E176A, and E176Q UreD variants as being deficient in urease activation. The substituted residues mapped to a buried water tunnel identified *in silico* which originates at the putative UreF:UreD interface and exits at the opposite face of UreD. Purified urease activated *in vivo* by these variants contained substoichiometric amounts of nickel and varied amounts of zinc and iron per UreABC.

My final project focused on characterization of the iron-containing urease from *Helicobacter mustelae*, UreA2B2, by resonance Raman spectroscopy. Previous studies showed the diferrous active site of this enzyme is rendered inactive in the presence of O_2, yielding a μ-oxo bridged, diferric metallocenter. In contrast to earlier results, I observed downshifts of the ν_s and ν_{as}(Fe-O-Fe) following anaerobic reduction in $H_2{}^{18}O$ and subsequent chemical oxidation relative to analysis of enzyme in $H_2{}^{16}O$, consistent with exchange of the μ-oxo atom. The ν_s(Fe-O-Fe) was downshifted by 10 cm^{-1} when the enzyme was incubated with urea or the slow-binding substrate phenyl phosphorodiamidate, but not following incubation with the inhibitor acetohydroxamic acid or the chaotropic agent guanidinium chloride. Rapid bulk-solvent exchange studies identified a urea- and solvent-sensitive mode at ~ 530 cm^{-1} which downshifted to ~511 cm^{-1} in D_2O or $H_2{}^{18}O$ and upshifted by 10 cm^{-1} in the presence of urea. This result was consistent with a terminal Fe-OH stretch where the hydroxyl group is not displaced on substrate binding. I also identified a slow substrate-binding form of UreA2B2.

I dedicate this dissertation to my father, Michael Farrugia, for his unending love and support. Through his sacrifice and example he made me the man I am today, and for that I owe him the world.

ACKNOWLEDGEMENTS

I thank my mentor and role-model, Robert Hausinger, for his guidance, support, patience, and for the numerous professional advancements he has helped me achieve, including my premier first author-paper and several scholarship and fellowship awards.I thank my family for providing me a wonderful network of love and support throughout my life and for always showing interest in my work by asking "What *exactly* do you *do*, again?" *constantly*. I thank my collaborators Drs. Kristin Parent, Brandon Ruotolo, Denis Proshlyakov, Roman Davydov, and Edward Solomon, as well as their undergraduate and graduate students for their assistance and input. Dr. Hausinger provided me the opportunity to mentor several undergraduate students, Sneha Grandhis, Evan Hsueh, and Adib Abdullah, whose assistance was greatly appreciated. A special thanks goes out to my lab colleagues, Scott Mulrooney, Tina Müller, Lee Macomber, Jodi Boer, and Eric Carter, whose insight and inspiration was invaluable. I thank my wife, Cynthia Lucidi, for her patience and support during my graduate career. Finally, I offer thanks to the DuVall fellowship for helping to support my graduate education.

TABLE OF CONTENTS

LIST OF TABLES

LIST OF FIGURES

KEY TO ABBREVIATIONS

BS^3, bis(sulfosuccinimidyl)suberate

CD, circular dichroism

CID, collision induced dissociation

CHES, 2-(cyclohexylamino)ethanesulfonic acid

EDTA, ethylenediaminetetraacetic acid

EPR, electron paramagnetic resonance spectroscopy

HEPES, 4-(2-hydroxyethyl)piperazine-1-ethanesulfonic acid

GTP, guanosine-5'-phosphate

ICP-AES, inductively coupled plasma-atomic emission spectroscopy

IPTG, isopropyl β-D-1-thiogalactopyranoside

MALDI-TOF MS, matrix-assisted laser desorption ionization time of flight mass spectrometry

MBP, maltose binding protein

MCD, magnetic circular dichroism

MES, 2-(N-morpholino)ethanesulfonic acid

MME, monomethyl ether

MPD, 2-Methyl-2,4-pentanediol

PEG, polyethylene glycol

TAPS, N-tris(hydroxymethyl)methyl-3-aminopropanesulfonic acid

Tris, 2-amino-2-(hydroxymethyl)-1,3-propanediol or (tris(hydroxymethyl)aminomethane)

SDS-PAGE, sodium dodecyl sulfate-polyacrylamide gel electrophoresis

SPG, succinic acid-phosphate-glycine

VTVH, variable-temperature, variable-field

U, µmol of urea degraded min^{-1}

UTR, untranslated region

CHAPTER 1

Introduction

Sections of this chapter were adapted from the publication "Biosynthesis of the Urease Metallocenter" in *The Journal of Biological Chemistry* 288:13178-13185 by Mark A. Farrugia, Lee Macomber, and Robert P. Hausinger.

The metalloenzyme urease catalyzes the first step in urea hydrolysis, the conversion of substrate to ammonia and carbamic acid, with the latter compound spontaneously decomposing to a second molecule of ammonia and bicarbonate (12, 19). This enzyme is found in all plants as well as a few Archaea and selected species of bacteria, fungi, and algae (18, 41, 53). Urease from jack bean seeds was the first enzyme to be crystallized (59) and the first enzyme shown to contain nickel that is essential to catalysis (19). Because urease activity is associated with several pathogenic microorganisms, studies related to its inhibition have the potential to yield advances in human health (6, 28, 40). Similarly, since urea is an important metabolite in plants and is often used as a nitrogen fertilizer, the inhibition of urease from plants and in soils has important impacts on agriculture (41, 60). In addition to studies of the enzyme itself, investigations into the activation of urease have highlighted a network of accessory proteins involved in the cellular uptake (27) and delivery of nickel into the urease active site (9, 35, 43-45). At the beginning of my studies, the general protein network for urease *in vivo* maturation and the kinetic properties and roles of urease in a variety of systems had already been determined (12, 42, 55). The following paragraphs summarize pertinent aspects of this prior set of knowledge and selected examples of more recent findings.

Urease Structure and Mechanism. Ureases from several organisms have been studied in detail (22, 32, 37) including crystallographically-characterized examples from *Klebsiella aerogenes* (30, 49, 50) and *Sporosarcina* (formerly *Bacillus*) *pasteurii* (4, 5) (each containing three subunits in a $(UreABC)_3$ configuration, Figure 1.1A), *Helicobacter pylori* (29) (for which a fusion of genes corresponding to *K. aerogenes ureA* and *ureB* results in only two subunits yielding a $((UreAB)_3)_4$ structure, Figure 1.1B), and the jack bean enzyme (1) (with a single subunit representing a fusion of all three bacterial subunits and forming back-to-back

homotrimers, $((\alpha)_3)_2$, Figure 1.1C). The metallocenter structures of these proteins are identical (Figure 1.1D), with two Ni^{2+} ions bridged by a carbamylated Lys residue and water; one metal (Ni#1) additionally coordinates two His residues and a terminal water molecule, while the second Ni^{2+} ion (Ni#2) coordinates to two His residues, one Asp residue, and a terminal water molecule. Aspects of the enzyme mechanism remain controversial (10, 12, 20, 21, 62), but most proposals suggest that the urea carbonyl oxygen displaces the terminal water from the Ni#1 while a second Ni^{2+}-bound water molecule (generally thought to be the bridging solvent) acts as a nucleophile to achieve catalysis. The tetrahedral intermediate then decays, with a nearby His residue serving as a general acid according to some proposals (50).

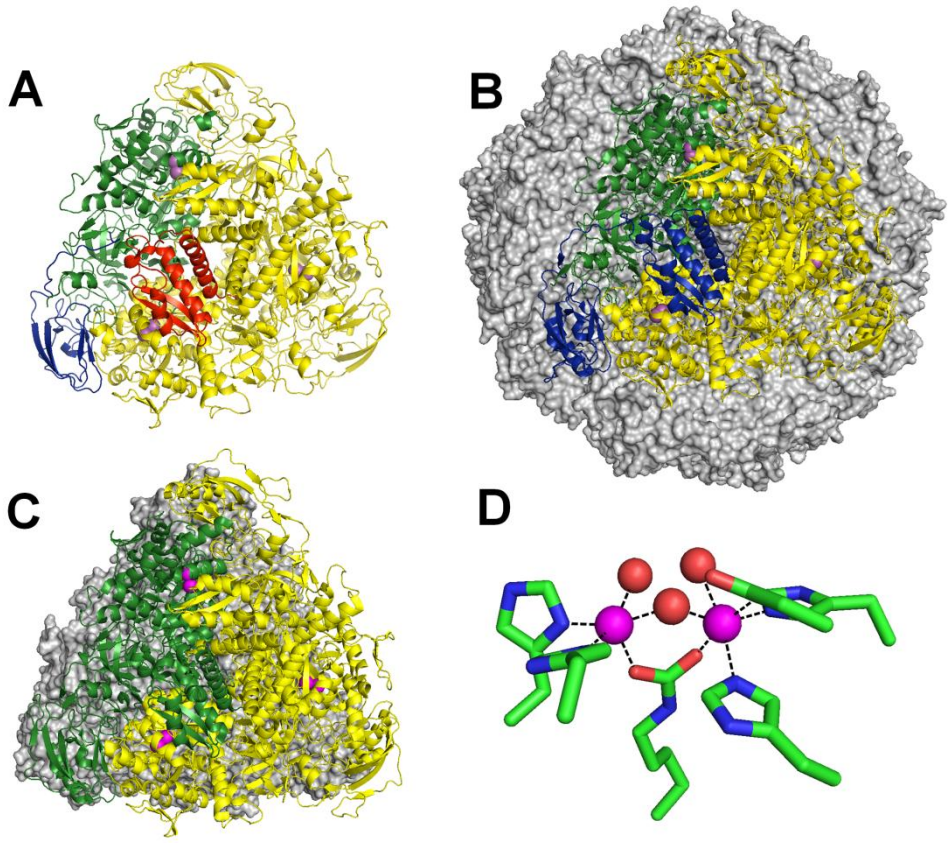

Figure 1.1: Urease structures. (A) Three-subunit bacterial ureases (UreA, *red*; UreB, *blue*; UreC, *green*; with two more copies, *yellow*) assemble into a trimer of trimers (Protein Data Bank code 1FWJ). (B) Two-subunit *Helicobacter* ureases (a fusion of the two small domains, *blue*; large subunit, *green*; with two more copies, *yellow*) form a trimer of dimers, which interacts with three more trimers (*gray* surface view) to form a dodecamer of dimers (code 1E9Z). (C) Single

Figure 1.1 (cont'd): subunit urease of fungi and plants (a fusion of all three domains, *green*; with two more copies, *yellow*) forms a trimer that stacks back-to-back with a second trimer (*gray* surface view) (code 3LA4). (D) Dinuclear Ni^{2+} metallocenter of urease (Ni^{2+}, *magenta*; solvent, *red*).

OVERVIEW OF UREASE ACTIVATION.

Our understanding of urease activation predominantly comes from investigations involving the heterologous expression of *K. aerogenes* urease genes in *Escherichia coli.* The *K. aerogenes* urease gene cluster (*ureDABCEFG*) encodes the urease structural enzyme subunits UreA, UreB, and UreC along with the accessory proteins UreD, UreE, UreF, and UreG (35). The accessory proteins are required for proper insertion of the two divalent nickel ions into each nascent active site, which is located within UreC (24). Complete maturation of the active site also includes carbamylation of a conserved lysine positioned between the two Ni^{2+} ions, though it is unclear whether this process is driven by the accessory proteins (47). Both the unmetallated and metallated forms of *K. aerogenes* urease (termed apo- and holourease or apo- and holoUreABC, respectively) associate as a trimer of heterotrimers $(UreABC)_3$ (30, 31). The roles of the urease accessory proteins in synthesis of the enzyme's buried metallocenters are described below.

UreD (UreH). UreD forms a soluble complex with apourease *in vivo* (45). Two-dimensional gel electrophoresis showed this complex exists with zero to three UreD bound per $(UreABC)_3$, with this association being lost upon activation (45). *In vitro* studies on the apoUreABC:UreD complex highlighted a role for UreD in enhancing activation, as incubation of apoUreABC with CO_2/bicarbonate plus Ni^{2+} yields urease specific activity that is only ~15% of that for wild-type holoUreABC whereas activity corresponding to ~30% of wild-type levels is obtained for similar incubation of apoUreABC:UreD (45, 48). Chemical cross-linking (16) and

small angle X-ray scattering studies (51) demonstrated that UreD interacts with UreC and UreB at the vertices of the trimer of heterotrimers. *In vitro* analysis of isolated UreD initially was stymied by its insolubility when produced in the absence of the structural subunits, but this issue was overcome by fusing it to maltose-binding protein (MBP) (13). *In vitro* equilibrium dialysis studies using this fusion construct showed UreD binds Ni^{2+} independent of its association with the structural subunits of urease (13). Finally, while no crystal structure of the *K. aerogenes* UreD exists, structures for the homologous UreH protein from *H. pylori* have been obtained in complex with the cognate UreF or with both UreF and UreG bound (25, 26). Overall, previous studies with UreD led to its hypothetical role as a scaffold protein that forms a complex with apourease and binds the distal accessory proteins, altogether allowing for nickel transfer into the nascent urease active site. The structural and functional roles of UreD in protein complexes with urease are investigated further in Chapter 3 of this dissertation.

UreF. Similar to UreD, *K. aerogenes* UreF is insoluble when produced heterologously in *E. coli* (43). The MBP-UreF (34) and UreE-UreF fusion proteins have been shown to be soluble, with the latter protein used in studies detailing its role in the cellular activation of urease and in interacting with UreABC:UreD (33). A complex containing UreABC:UreD:UreF can be directly isolated from cells expressing the corresponding genes (43). Native gel electrophoresis of UreABC:UreD:UreF revealed multiple species consistent with zero to three pairs of UreD:UreF bound per $(UreABC)_3$. Small angle x-ray scattering experiments suggested a close proximity between UreD and UreF, with both accessory proteins binding in the vicinity of UreB (51). Chemical cross-linking results support this configuration and also provide evidence for a conformational change in urease within the UreABC:UreD:UreF complex (16); specifically, UreB is proposed to undergo a hinge-like motion that enhances access to the nascent active site

(11). Following the *in vitro* activation of UreABC:UreD:UreF by incubation with CO_2/bicarbonate and Ni^{2+}, the urease specific activity is similar to that obtained by activation of UreABC:UreD; however, much lower concentrations of bicarbonate are required (43). UreF also serves as the binding site for the UreG GTPase within the UreABC:UreD:UreF complex. Mutagenesis studies of UreF were used to gauge its role as a GTPase activating protein and gave evidence that the protein instead acts to gate the GTPase activity of UreG so as to promote efficient coupling of GTP hydrolysis and metallocenter biosynthesis, thereby enhancing the fidelity of urease activation (7). Whereas no evidence has been obtained for nickel binding to *K. aerogenes* UreF, isothermal titration calorimetry studies using *H. pylori* UreF that was produced heterologously in *E. coli* provided evidence of a nickel-binding role for UreF, suggesting a potential role in nickel transfer into urease (61). In summary, UreF functions in urease activation by connecting UreD to UreG and by regulating the GTPase activity of the latter protein to facilitate nickel transfer into urease.

UreG. In contrast to *K. aerogenes* UreD and UreF, UreG is soluble in this and other organisms, and the protein has been characterized from several sources (8, 44, 52, 63-65). *K. aerogenes* UreG is a monomer that binds one equivalent of nickel or zinc (K_d ~5 μM for either metal) (8), whereas the *H. pylori* protein dimerizes in the presence of zinc (K_d ~0.3 μM, 1/dimer), but not with nickel which binds weakly (K_d ~10 μM, 1.8/monomer). X-ray absorption spectroscopy of the zinc-bound *H. pylori* protein reveals a trigonal bipyramidyl site including two His and two Cys residues (36). This site is buried between the homodimers of UreG and UreF in the $(UreH:UreF:UreG)_2$ crystal structure from *H. pylori* (26). As expected from sequence analysis, UreG is a GTPase; however, the free protein exhibits slow (52, 63, 64) or no (44, 65) GTPase activity. Substituting a key residue in the P-loop motif of UreG from *K.*

aerogenes or *H. pylori* abolishes the cell's ability to make active urease (38, 44), demonstrating the importance of this GTPase activity when UreG is present in urease activation complexes. A UreABC:UreD:UreF:UreG complex forms in *E. coli* cultures expressing the *K. aerogenes* urease gene cluster in the absence of nickel (46).

UreD(UreH):UreF:UreG. As an alternative to sequentially adding each accessory protein to the urease apoenzyme, the UreD:UreF:UreG heterotrimer may bind as a unit to urease. A UreD:UreF:UreG complex forms *in vivo* when the corresponding *K. aerogenes* genes are expressed independently of the structural components (44); however, this species is poorly soluble and not well characterized. This solubility problem is overcome in the MBP-UreD:UreF:UreG complex, and this species has been shown to bind urease (11, 23). MBP-UreD:UreF:UreG contains two copies of each protomer according to gel filtration and mass spectrometric studies (23). The properties of this complex, including its interactions with urease and stability in various urease activation conditions, are detailed further in Chapter 2 and Chapter 5 of this dissertation. The structure of the analogous $(UreH:UreF:UreG)_2$ complex from *H. pylori* reveals two UreG promoters binding to one face of the UreF dimer, with each UreG interacting with both UreF protomers, and with each UreH interacting with a single UreF (Figure 1.2) (26). GDP is bound opposite of UreF within each UreG, confirming that the former protein is not a typical GTPase-activating protein. A potential nickel-binding site is deeply buried and bridges the two UreG molecules, with each protomer providing His and Cys residues. Analysis of this structure reveals a potential water tunnel extending from the buried nickel-binding site of UreG through UreF and exiting at UreH, with the authors hypothesizing the tunnel functions in nickel transfer (61).

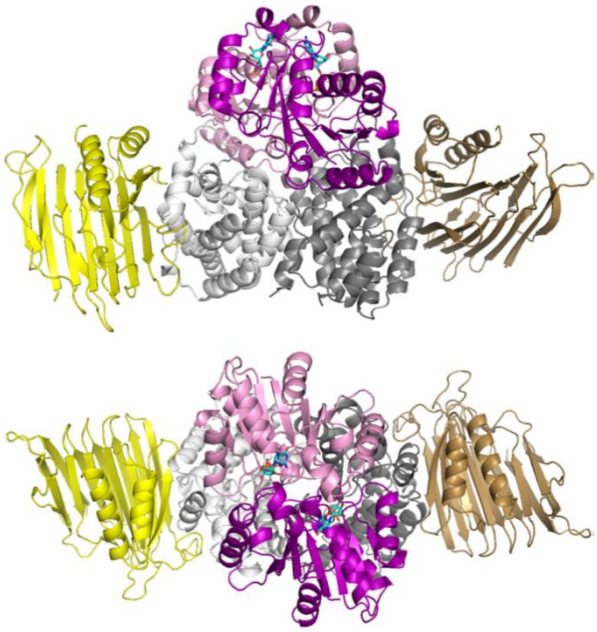

Figure 1.2: Structure of UreH:UreF:UreG. Shown are two views of the $(UreH:UreF:UreG)_2$ complex from *H. pylori* (UreH, UreF and UreG in shades of *yellow*, *gray* and *magenta*, respectively). A GDP molecule (*cyan*) is located in each UreG.

UreE. Finally, the nickel metallochaperone UreE has been characterized from several organisms (2, 3, 9, 17). A crystal structure of a functional, truncated form of *K. aerogenes* UreE revealed three copper-binding sites per dimer, two sites composed of His110 and His112 within each protomer and a third interfacial site composed of His96 from each protomer (9, 56). These copper-binding sites are thought to also bind the relavent target metal: nickel. Mutagenesis studies demonstrated that only the interfacial site is required for UreE function (17). *S. pasteurii* UreE's crystal structure also highlights a dimeric quaternary structure with a Zn-occupied interfacial site (presumably substituting for Ni^{2+}) (4, 57). Structures of several forms of *H. pylori* UreE are known, including the nickel-bound species (codes 3NYO and 3TJ8) (2, 54) for which the Ni^{2+} is coordinated at the interfacial site with an additional His residue provided by the *C*-terminus. Overall, the highly soluble UreE proteins are proposed to bind metal ions in the

cytoplasm and specifically deliver nickel to urease within the complex of other accessory proteins.

In addition to the independent protein species, UreE forms UreG:UreE and UreABC:UreD:UreF:UreG:UreE complexes that may be functionally important. For the *H. pylori* components, two UreG protomers bind the UreE dimer, with the interaction stabilized by Zn^{2+}, but not Ni^{2+} (3). In contrast, one UreG monomer from *K. aerogenes* binds to its cognate UreE dimer, with the interaction stabilized by either Zn^{2+} or Ni^{2+} (8). NMR studies on a complex of *S. pasteurii* UreG and UreE were used to map the interaction face, leading to the suggestion that the UreG binding sites for UreF and UreEare shared (39). Alternatively, using the *K. aerogenes* system, a UreABC:UreD:UreF:UreG:UreE complex can be directly isolated from cells that synthesize a G11P UreB variant (51) or a *Strep* II-tagged variant of UreG when the culture contains Ni^{2+} (8). From this abundance of information on the urease activation machinery the current hypothetical pathway for urease activation can be illustrated (Figure 1.3).

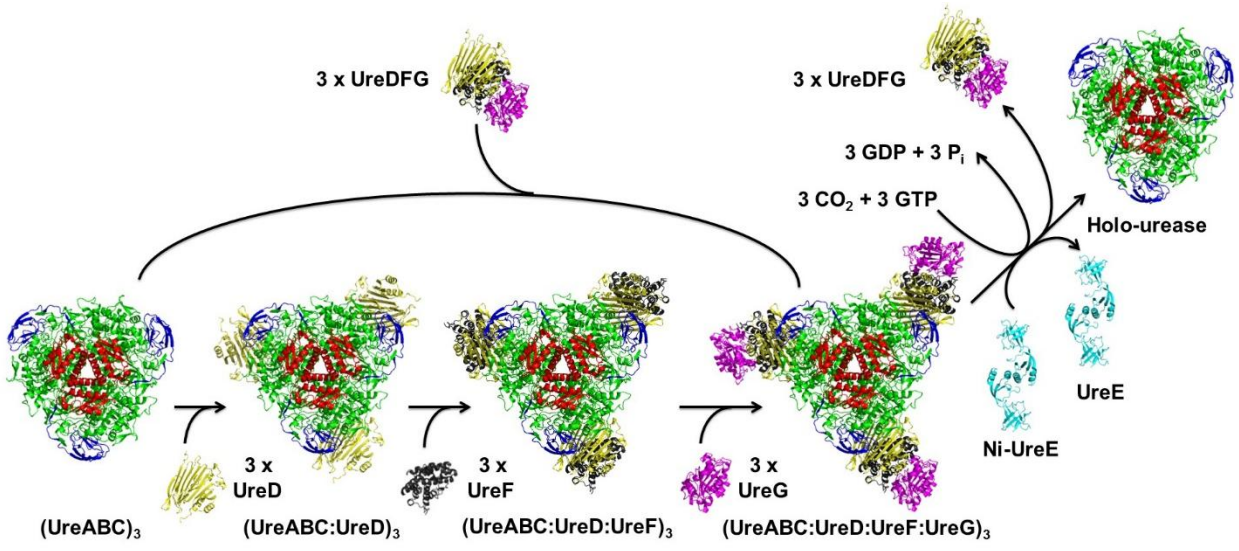

Figure 1.3: Hypothetical model of urease activation for *K. aerogenes* urease. The trimer-of-trimers urease apoprotein (UreA, *red*; UreB, *blue*; UreC, *green*) either sequentially binds UreD (*yellow*), UreF (*gray*), and UreG (*magenta*) or binds the UreDFG complex (only one protomer of

Figure 1.3 (cont'd): each protein is shown, but the isolated complex contains two protomers of each). UreD and UreF protomers depicted are homology models derived from the *H. pylori* UreH:UreF crystal structure (PDB 3SF5) while UreG is a homology model derived from *Methanocaldococcus jannaschii* HypB (PDB 2HF9). The coordinates were generously provided by Dr. Célia Carlini for use in this figure. Formation of the active enzyme requires CO_2 to carbamylate Lys217 at the native active site, GTP binding and hydrolysis by UreG, and nickel delivery by dimeric UreE (*cyan*). It remains unclear whether the accessory proteins are released as a UreDFG unit or as individual proteins.

Iron-Containing Urease. A new tool for characterizing urease came in the form of an iron-containing protein, UreA2B2, from *Helicobacter mustelae* (15). This organism contains a conventional *H. pylori*-like urease gene cluster (*ureABEDFGH*) which is induced by nickel ions and a separate two-gene cluster (*ureA2B2*) that lacks nearby genes coding for accessory proteins and is inversely regulated by nickel (58). Although the sequences of UreA and UreB are 57% and 70% identical to UreA2 and UreB2 in *H. mustelae*, the former protein contains nickel and the latter possesses divalent iron – thus accounting for its oxygen sensitivity. The crystal structure of UreA2B2 reveals that its active site residues are conserved with those of the nickel enzymes (15). Using the oxidized, inactive enzyme, ultraviolet-visible and resonance Raman spectroscopic studies identified a diferric species with a putative μ-oxo bridge (14, 15). In particular, resonance Raman studies identified a Fe(III)-O-Fe(III) symmetric vibrational mode that was shown to be sensitive to the presence of urea, with the bridging oxygen also being exchange inert to bulk solvent over a long timeframe (> days) (14). Overall, the inactive form of iron urease allowed for the use of spectroscopic techniques that were previously unavailable for use in the catalytically active, spectroscopically silent, nickel enzyme. My studies further characterizing the iron urease are detailed in Chapter 4 and Chapter 5.

BIBLIOGRAPHY

BIBLIOGRAPHY

1. **Balasubramanian, A., and Ponnuraj, K.** 2010. Crystal structure of the first plant urease from jack bean: 83 years of journey from its first crystal to molecular structure. J. Mol. Biol. **400**: 274-283.

2. **Banaszak, K., Martin-Diaconescu, V., Bellucci, M., Zambelli, B., Rypniewski, W., Maroney, M. J., and Ciurli, S.** 2012. Crystallographic and X-ray absorption spectroscopic characterization of *Helicobacter pylori* UreE bound to Ni^{2+} and Zn^{2+} reveals a role for the disordered C-terminal arm in metal trafficking. Biochem. J. **441**: 1017-1026.

3. **Bellucci, M., Zambelli, B., Musiani, F., Turano, P., and Ciurli, S.** 2009. *Helicobacter pylori* UreE, a urease accessory protein: specific Ni^{2+}- and Zn^{2+}-binding properties and interaction with its cognate UreG. Biochem. J. **422**: 91-100.

4. **Benini, S., Rypniewski, W. R., Wilson, K. S., Ciurli, S., and Mangani, S.** 2001. Structure-based rationalization of urease inhibition by phosphate: novel insights into the enzyme mechanism. J. Biol. Inorg. Chem. **6**: 778-790.

5. **Benini, S., Rypniewski, W. R., Wilson, K. S., Miletti, S., Ciurli, S., and Mangani, S.** 1999. A new proposal for urease mechanism based on the crystal structures of the native and inhibited enzyme from *Bacillus pasteurii*: why urea hydrolysis costs two nickels. Structure **7**: 205-216.

6. **Blaser, M. J., and Atherton, J. C.** 2004. *Helicobacter pylori* persistence: biology and disease. J. Clin. Invest. **113**: 321-333.

7. **Boer, J. L., and Hausinger, R. P.** 2012. *Klebsiella aerogenes* UreF: identification of the UreG binding site and role in enhancing the fidelity of urease activation. Biochemistry **51**: 2298-2308.

8. **Boer, J. L., Quiroz-Valenzuela, S., Anderson, K. L., and Hausinger, R. P.** 2010. Mutagenesis of *Klebsiella aerogenes* UreG to probe nickel binding and interactions with other urease-related proteins. Biochemistry **49**: 5859-5869.

9. **Brayman, T. G., and Hausinger, R. P.** 1996. Purification, characterization, and functional analysis of a truncated *Klebsiella aerogenes* UreE urease accessory protein lacking the histidine-rich carboxyl terminus. J. Bacteriol. **178**: 5410-5416.

10. **Carlsson, H., and Nordlander, E.** 2010. Computational modeling of the mechanism of urease. Bioinorg. Chem. Appl. **2010**.

11. **Carter, E. L., Boer, J. L., Farrugia, M. A., Flugga, N., Towns, C. L., and Hausinger, R. P.** 2011. Function of UreB in *Klebsiella aerogenes* urease. Biochemistry **50**: 9296-9308.

12. **Carter, E. L., Flugga, N., Boer, J. L., Mulrooney, S. B., and Hausinger, R. P.** 2009. Interplay of metal ions and urease. Metallomics **1**: 207-221.

13. **Carter, E. L., and Hausinger, R. P.** 2010. Characterization of the *Klebsiella aerogenes* urease accessory protein UreD in fusion with the maltose binding protein. J. Bacteriol. **192**: 2294-2304.

14. **Carter, E. L., Proshlyakov, D. A., and Hausinger, R. P.** 2012. Apoprotein isolation and activation, and vibrational structure of the *Helicobacter mustelae* iron urease. J. Inorg. Biochem. **111**: 195-202.

15. **Carter, E. L., Tronrud, D. E., Taber, S. R., Karplus, P. A., and Hausinger, R. P.** 2011. Iron-containing urease in a pathogenic bacterium. Proc. Natl. Acad. Sci. U.S.A. **108**: 13095-13099.

16. **Chang, Z., Kuchar, J., and Hausinger, R. P.** 2004. Chemical cross-linking and mass spectrometric identification of sites of interaction for UreD, UreF, and urease. J. Biol. Chem. **279**: 15305-15313.

17. **Colpas, G. J., Brayman, T. G., Ming, L. J., and Hausinger, R. P.** 1999. Identification of metal-binding residues in the *Klebsiella aerogenes* urease nickel metallochaperone, UreE. Biochemistry **38**: 4078-4088.

18. **Cox, G. M., Mukherjee, J., Cole, G. T., Casadevall, A., and Perfect, J. R.** 2000. Urease as a virulence factor in experimental cryptococcosis. Infect. Immun. **68**: 443-448.

19. **Dixon, N. E., Gazzola, T. C., Blakeley, R. L., and Zermer, B.** 1975. Jack bean urease (EC 3.5.1.5). A metalloenzyme. A simple biological role for nickel? J. Am. Chem. Soc. **97**: 4131-4133.

20. **Estiu, G., and Merz, K. M., Jr.** 2006. Catalyzed decomposition of urea. Molecular dynamics simulations of the binding of urea to urease. Biochemistry **45**: 4429-4443.

21. **Estiu, G., and Merz, K. M., Jr.** 2007. Competitive hydrolytic and elimination mechanisms in the urease catalyzed decomposition of urea. J. Phys. Chem. B. **111**: 10263-10274.

22. **Evans, D. J., Jr., Evans, D. G., Kirkpatrick, S. S., and Graham, D. Y.** 1991. Characterization of the *Helicobacter pylori* urease and purification of its subunits. Microb. Pathog. **10**: 15-26.

23. **Farrugia, M. A., Han, L., Zhong, Y., Boer, J. L., Ruotolo, B. T., and Hausinger, R. P.** 2013. Analysis of a soluble $(UreD:UreF:UreG)_2$ accessory protein complex and its interactions with *Klebsiella aerogenes* urease by mass spectrometry. J. Am. Soc. Mass. Spectrom. **24**: 1328-1337.

24. **Farrugia, M. A., Macomber, L., and Hausinger, R. P.** 2013. Biosynthesis of the urease metallocenter. J. Biol. Chem. **288**: 13178-13185.

25. **Fong, Y. H., Wong, H. C., Chuck, C. P., Chen, Y. W., Sun, H., and Wong, K. B.** 2011. Assembly of preactivation complex for urease maturation in *Helicobacter pylori*: crystal structure of UreF-UreH protein complex. J. Biol. Chem. **286**: 43241-43249.

26. **Fong, Y. H., Wong, H. C., Yuen, M. H., Lau, P. H., Chen, Y. W., and Wong, K. B.** 2013. Structure of UreG/UreF/UreH complex reveals how urease accessory proteins facilitate maturation of *Helicobacter pylori* urease. PLoS Biol. **11**: e1001678.

27. **Ge, R. G., Wang, D. X., Hao, M. C., and Sun, X. S.** 2013. Nickel trafficking system responsible for urease maturation in *Helicobacter pylori*. World J. Gastroenterol. **19**: 8211-8218.

28. **Griffith, D. P., Musher, D. M., and Itin, C.** 1976. Urease. The primary cause of infection-induced urinary stones. Invest. Urol. **13**: 346-350.

29. **Ha, N. C., Oh, S. T., Sung, J. Y., Cha, K. A., Lee, M. H., and Oh, B. H.** 2001. Supramolecular assembly and acid resistance of *Helicobacter pylori* urease. Nat. Struct. Biol. **8**: 505-509.

30. **Jabri, E., Carr, M. B., Hausinger, R. P., and Karplus, P. A.** 1995. The crystal structure of urease from *Klebsiella aerogenes*. Science **268**: 998-1004.

31. **Jabri, E., and Karplus, P. A.** 1996. Structures of the *Klebsiella aerogenes* urease apoenzyme and two active-site mutants. Biochemistry **35**: 10616-10626.

32. **Kim, J. K., Mulrooney, S. B., and Hausinger, R. P.** 2005. Biosynthesis of active *Bacillus subtilis* urease in the absence of known urease accessory proteins. J. Bacteriol. **187**: 7150-7154.

33. **Kim, J. K., Mulrooney, S. B., and Hausinger, R. P.** 2006. The UreEF fusion protein provides a soluble and functional form of the UreF urease accessory protein. J. Bacteriol. **188**: 8413-8420.

34. **Kim, K. Y., Yang, C. H., and Lee, M. H.** 1999. Expression of the recombinant *Klebsiella aerogenes* UreF protein as a MalE fusion. Arch. Pharm. Res. **22**: 274-278.

35. **Lee, M. H., Mulrooney, S. B., Renner, M. J., Markowicz, Y., and Hausinger, R. P.** 1992. *Klebsiella aerogenes* urease gene cluster: sequence of *ureD* and demonstration that

four accessory genes (*ureD*, *ureE*, *ureF*, and *ureG*) are involved in nickel metallocenter biosynthesis. J. Bacteriol. **174**: 4324-4330.

36. **Martin-Diaconescu, V., Bellucci, M., Musiani, F., Ciurli, S., and Maroney, M. J.** 2012. Unraveling the *Helicobacter pylori* UreG zinc binding site using X-ray absorption spectroscopy (XAS) and structural modeling. J. Biol. Inorg. Chem. **17**: 353-361.

37. **McCoy, D. D., Cetin, A., and Hausinger, R. P.** 1992. Characterization of urease from *Sporosarcina ureae*. Arch. Microbiol. **157**: 411-416.

38. **Mehta, N., Benoit, S., and Maier, R. J.** 2003. Roles of conserved nucleotide-binding domains in accessory proteins, HypB and UreG, in the maturation of nickel-enzymes required for efficient *Helicobacter pylori* colonization. Microb. Pathog. **35**: 229-234.

39. **Merloni, A., Dobrovolska, O., Zambelli, B., Agostini, F., Bazzani, M., Musiani, F., and Ciurli, S.** 2014. Molecular landscape of the interaction between the urease accessory proteins UreE and UreG. Biochim. Biophys. Acta **1844**: 1662-1674.

40. **Mobley, H. L.** 1996. The role of *Helicobacter pylori* urease in the pathogenesis of gastritis and peptic ulceration. Aliment. Pharmacol. Ther. **10 Suppl 1**: 57-64.

41. **Mobley, H. L., and Hausinger, R. P.** 1989. Microbial ureases: significance, regulation, and molecular characterization. Microbiol. Rev. **53**: 85-108.

42. **Mobley, H. L., Island, M. D., and Hausinger, R. P.** 1995. Molecular biology of microbial ureases. Microbiol. Rev. **59**: 451-480.

43. **Moncrief, M. B., and Hausinger, R. P.** 1996. Purification and activation properties of UreD-UreF-urease apoprotein complexes. J. Bacteriol. **178**: 5417-5421.

44. **Moncrief, M. B., and Hausinger, R. P.** 1997. Characterization of UreG, identification of a UreD-UreF-UreG complex, and evidence suggesting that a nucleotide-binding site in UreG is required for *in vivo* metallocenter assembly of *Klebsiella aerogenes* urease. J. Bacteriol. **179**: 4081-4086.

45. **Park, I. S., Carr, M. B., and Hausinger, R. P.** 1994. *In vitro* activation of urease apoprotein and role of UreD as a chaperone required for nickel metallocenter assembly. Proc. Natl. Acad. Sci. U.S.A. **91**: 3233-3237.

46. **Park, I. S., and Hausinger, R. P.** 1995. Evidence for the presence of urease apoprotein complexes containing UreD, UreF, and UreG in cells that are competent for *in vivo* enzyme activation. J. Bacteriol. **177**: 1947-1951.

47. **Park, I. S., and Hausinger, R. P.** 1995. Requirement of carbon dioxide for *in vitro* assembly of the urease nickel metallocenter. Science **267**: 1156-1158.

48. **Park, I. S., and Hausinger, R. P.** 1996. Metal ion interaction with urease and UreD-urease apoproteins. Biochemistry **35**: 5345-5352.

49. **Pearson, M. A., Michel, L. O., Hausinger, R. P., and Karplus, P. A.** 1997. Structures of Cys319 variants and acetohydroxamate-inhibited *Klebsiella aerogenes* urease. Biochemistry **36**: 8164-8172.

50. **Pearson, M. A., Park, I. S., Schaller, R. A., Michel, L. O., Karplus, P. A., and Hausinger, R. P.** 2000. Kinetic and structural characterization of urease active site variants. Biochemistry **39**: 8575-8584.

51. **Quiroz-Valenzuela, S., Sukuru, S. C., Hausinger, R. P., Kuhn, L. A., and Heller, W. T.** 2008. The structure of urease activation complexes examined by flexibility analysis, mutagenesis, and small-angle X-ray scattering. Arch. Biochem. Biophys. **480**: 51-57.

52. **Real-Guerra, R., Staniscuaski, F., Zambelli, B., Musiani, F., Ciurli, S., and Carlini, C. R.** 2012. Biochemical and structural studies on native and recombinant *Glycine max* UreG: a detailed characterization of a plant urease accessory protein. Plant Mol. Biol. **78**: 461-475.

53. **Rees, T. A., and Bekheet, I. A.** 1982. The role of nickel in urea assimilation by algae. Planta **156**: 385-387.

54. **Shi, R., Munger, C., Asinas, A., Benoit, S. L., Miller, E., Matte, A., Maier, R. J., and Cygler, M.** 2010. Crystal structures of apo and metal-bound forms of the UreE protein from *Helicobacter pylori*: role of multiple metal binding sites. Biochemistry **49**: 7080-7088.

55. **Sirko, A., and Brodzik, R.** 2000. Plant ureases: roles and regulation. Acta Biochim. Pol. **47**: 1189-1195.

56. **Song, H. K., Mulrooney, S. B., Huber, R., and Hausinger, R. P.** 2001. Crystal structure of *Klebsiella aerogenes* UreE, a nickel-binding metallochaperone for urease activation. J. Biol. Chem. **276**: 49359-49364.

57. **Stola, M., Musiani, F., Mangani, S., Turano, P., Safarov, N., Zambelli, B., and Ciurli, S.** 2006. The nickel site of *Bacillus pasteurii* UreE, a urease metallo-chaperone, as revealed by metal-binding studies and X-ray absorption spectroscopy. Biochemistry **45**: 6495-6509.

58. **Stoof, J., Breijer, S., Pot, R. G., van der Neut, D., Kuipers, E. J., Kusters, J. G., and van Vliet, A. H.** 2008. Inverse nickel-responsive regulation of two urease enzymes in the gastric pathogen *Helicobacter mustelae*. Environ. Microbiol. **10**: 2586-2597.

59. **Sumner, J. B.** 1926. The isolation and crystallization of the enzyme urease. J. Biol. Chem. **69**: 435-441.

60. **Witte, C. P.** 2011. Urea metabolism in plants. Plant Sci. **180**: 431-438.

61. **Zambelli, B., Berardi, A., Martin-Diaconescu, V., Mazzei, L., Musiani, F., Maroney, M. J., and Ciurli, S.** 2014. Nickel binding properties of *Helicobacter pylori* UreF, an accessory protein in the nickel-based activation of urease. J. Biol. Inorg. Chem. **19**: 319-334.

62. **Zambelli, B., Musiani, F., Benini, S., and Ciurli, S.** 2011. Chemistry of Ni^{2+} in urease: sensing, trafficking, and catalysis. Acc. Chem. Res. **44**: 520-530.

63. **Zambelli, B., Musiani, F., Savini, M., Tucker, P., and Ciurli, S.** 2007. Biochemical studies on *Mycobacterium tuberculosis* UreG and comparative modeling reveal structural and functional conservation among the bacterial UreG family. Biochemistry **46**: 3171-3182.

64. **Zambelli, B., Stola, M., Musiani, F., De Vriendt, K., Samyn, B., Devreese, B., Van Beeumen, J., Turano, P., Dikiy, A., Bryant, D. A., and Ciurli, S.** 2005. UreG, a chaperone in the urease assembly process, is an intrinsically unstructured GTPase that specifically binds Zn^{2+}. J. Biol. Chem. **280**: 4684-4695.

65. **Zambelli, B., Turano, P., Musiani, F., Neyroz, P., and Ciurli, S.** 2009. Zn^{2+}-linked dimerization of UreG from *Helicobacter pylori*, a chaperone involved in nickel trafficking and urease activation. Proteins **74**: 222-239.

CHAPTER 2

Analysis of a Soluble (UreD:UreF:UreG)$_2$ Accessory Protein Complex and Its Interactions with *Klebsiella aerogenes* Urease by Mass Spectrometry

This chapter is modified from the *Journal of the American Society of Mass Spectrometry* 24(9): 1328-37 (2013) by Mark A. Farrugia, Linjie Han, Yueyang Zhong, Jodi L. Boer, Brandon T. Ruotolo, and Robert P. Hausinger. Linjie Han and Yueyang Zhong carried out ion mobility mass spectrometry in the Ruotolo laboratory and Jodi Boer provided protein samples.

ABSTRACT

Maturation of the nickel-containing urease of *Klebsiella aerogenes* is facilitated by the UreD, UreF, and UreG accessory proteins along with the UreE metallochaperone. A fusion of the maltose binding protein and UreD (MBP-UreD) was co-isolated with UreF and UreG in a soluble complex possessing a $(MBP\text{-}UreD:UreF:UreG)_2$ quaternary structure. Within this complex a UreF:UreF interaction was identified by chemical cross-linking of the amino termini of its two UreF protomers, as shown by mass spectrometry of tryptic peptides. A pre-activation complex was formed by the interaction of $(MBP\text{-}UreD:UreF:UreG)_2$ and urease. Mass spectrometry of intact protein species revealed a pathway for synthesis of the urease pre-activation complex in which individual hetero-trimer units of the $(MBP\text{-}UreD:UreF:UreG)_2$ complex bind to urease. Together, these data provide important new insights into the structures of protein complexes associated with urease activation.

INTRODUCTION

Urease, an enzyme that hydrolyzes urea to form ammonia and carbonic acid (10, 43), plays important roles in nitrogen cycling and pathogenesis (29, 42). Like most bacterial ureases, the *Klebsiella aerogenes* protein contains three subunits (UreA, UreB, and UreC) arranged in a $(UreABC)_3$ architecture with a dinuclear nickel active site in each of its UreC subunits (21). The enzyme is synthesized by an elaborate biosynthetic pathway that requires four accessory proteins (UreD, UreE, UreF, and UreG) along with carbon dioxide, GTP, and the metal ions (10, 14, 43). A working hypothesis for *K. aerogenes* urease activation (Figure 2.1) shows the $(UreABC)_3$ apoprotein (25) forming sequential complexes with UreD (32), UreF (30), and UreG (33) or binding a pre-formed complex of UreD, UreF, and UreG (UreDFG) (31). The resulting pre-activation urease complex carbamylates an active site lysine side chain to form a metal-binding ligand (34) and acquires nickel ions from the UreE metallo-chaperone (26) in a process driven by GTP hydrolysis (39). Completion of this process is accompanied by dissociation of the accessory proteins.

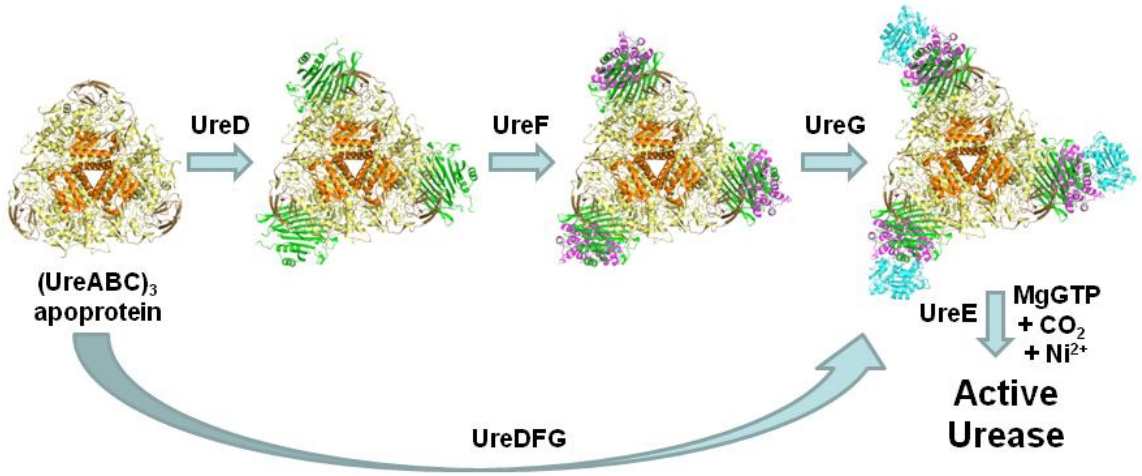

Figure 2.1: Working model of urease activation. The urease apoprotein (orange UreA, sand UreB, and yellow UreC) sequentially binds UreD (green), UreF (magenta), and UreG (cyan) or binds a complex of these three accessory proteins to form a pre-activation complex. Synthesis of active enzyme requires carbamylation of an active site lysine by CO_2, GTP hydrolysis by UreG,

Figure 2.1 (cont'd): and Ni^{2+} transfer from the UreE metallochaperone. Structures of the docked complexes are derived from computational models (27).

The protein complexes in the urease activation pathway have been studied to varying extents, but many questions about their structures and properties remain to be answered. Chemical cross-linking of $(UreABC)_3$:UreD followed by proteolysis and matrix-assisted laser-desorption ionization (MALDI) time-of-flight (TOF) mass spectrometry (MS) indicates that UreD binds to UreB and UreC (12). Small angle X-ray scattering (SAXS) data from this species are consistent with the UreD density being located at the vertices of the triangular urease apoprotein (35). Corresponding cross-linking/proteolysis/MALDI-TOF-MS and SAXS analyses of the $(UreABC)_3$:UreD:UreF species show a UreF linkage to UreB and yield similar positional results. Moreover, cross-linking and computational flexibility studies provide evidence that UreB is loosely associated with UreC in this complex and can move in a hinge-like motion that potentially enhances the nickel ions' access to the active site (12, 35). $(UreABC)_3$:UreD, $(UreABC)_3$:UreD:UreF, and $(UreABC)_3$:UreDFG exhibit multiple bands on native gels, and analysis of these bands on denaturing gels reveals peptide staining intensities consistent with varied numbers of UreD, UreF, and UreG bound to the $(UreABC)_3$ apoprotein. The structure of *K. aerogenes* urease apoprotein is known (22), but no urease:accessory protein complexes have been structurally elucidated. By contrast, the urease-free structures are known for *Helicobacter pylori* UreF (24) and the complex of UreF with UreH (the UreD homologue in *H. pylori*) (15), while UreG homology models have been generated by using the related HypB dimeric structure from *Methanocaldococcus jannaschii* (16).

Whereas the sequential protein binding urease activation model (Figure 2.1, top) depicts individual protomers of the accessory proteins binding to the urease apoprotein vertices, evidence from homologous systems suggests that the pre-formed accessory protein complex may

be dimeric. For example, *H. pylori* UreF and UreH:UreF each possess an overall dimeric structure (i.e., $(UreF)_2$, $(UreH:UreF)_2$) (15, 24). Furthermore, UreG is dimeric as purified from some microorganisms (44, 45), although the *K. aerogenes* protein is monomeric (7, 31). It is plausible that distinct quaternary structures of the urease accessory proteins are found in *K. aerogenes* and *H. pylori.* Alternatively, it is possible that *K. aerogenes* also produces a dimeric accessory protein complex, but it dissociates to the monomeric form when it binds to urease. In addition, it is feasible that the complexes obtained by sequential binding of accessory proteins are distinct from those generated by binding of UreDFG. To resolve these questions, I utilized chemical cross-linking/proteolysis/MS methods to characterize a soluble UreDFG complex from *K. aerogenes*, demonstrated that the accessory protein complex binds to urease, and used MS tuned to retain fragile non-covalent contacts to examine the intact structures of various urease complexes. The results obtained provide substantial support for the protein complex assembly model (Figure 2.1 lower path) and present new insights into the stability of various urease complexes.

MATERIALS AND METHODS

Preparation of Protein Samples. Urease holoenzyme was produced in *E. coli* BL21-Gold(DE3) cells containing pKK17 (the pKK223-3 vector with the complete *ureDABCEFG* gene cluster) that were grown in lysogeny broth (LB) with 300 μg ml^{-1} ampicillin plus 1 mM $NiCl_2$ and induced at an optical density (600 nm) of ~0.4 with 0.1 mM isopropyl β-thiogalactopyranoside. The protein was purified as previously described (11). The $(UreABC)_3$ apoprotein was purified in the same manner from the same *E. coli* cells that were grown in LB medium without added $NiCl_2$.

The *Strep*-tag II version of $(UreABC)_3$:UreDFG was formed in cells transformed with pKKG containing *ureDABCEFG* where *ureG* is fused to the codons for *Strep*-tag II (6). This complex was purified by use of a *Strep*-tactin column followed by Superdex 200 gel filtration chromatography, as previously described (6).

A hetero-trimeric MBP-UreDFG species, containing a maltose binding protein (MBP) fusion of UreD (MBP-UreD) along with UreF and UreG, was obtained from *E. coli* BL21-Gold(DE3) cells co-expressing pEC005 (with *ureFG* cloned into pACT3) and pEC002 (with *ureD* cloned into pASK-IBA3plus), as previously described (9, 11). The complex was isolated by sequential amylose, DEAE-Sepharose, and Superdex 200 column chromatography of cell-free extracts. A version of this species containing the K165A variant of UreF was purified by similar approaches using cells with pEC005-UreF-K165A (a modified pEC005) and pEC002 (6). MBP-UreDFG or its K165A UreF version was mixed with excess urease apoprotein or holoenzyme, incubated 60 min, and separated by chromatography on amylose resin to remove excess urease.

General Properties of MBP-UreDFG. The native molecular mass of MBP-UreDFG was assessed by Superdex 200 gel filtration chromatography in 20 mM Tris-HCl buffer (pH 7.5) containing 1 mM EDTA, 1 mM β-mercaptoethanol, and 25 mM NaCl and using thyroglobulin, γ-globulin, ovalbumin, and myoglobin (Bio-Rad) as molecular mass markers. The apparent molecular masses of denatured components in various samples were obtained by sodium dodecyl sulfate-polyacrylamide gel electrophoresis (SDS-PAGE; 12% running gels) (23), followed by staining with Coomassie brilliant blue. Integration of band intensities was assessed by gel scanning (Alpha Innotech Corp., using AlphaEase FC software).

Chemical Cross-Linking, Proteolysis, and MALDI-TOF-MS of MBP-UreDFG. MBP-UreDFG and its K165A UreF derivative were further characterized by a chemical cross-

linking approach. The samples (3.75 µM of the heterotrimer in 20 µl) were incubated with 160-fold excess (600 µM) Bis(sulfosuccinimidyl)suberate (BS^3) (Thermo Fisher Scientific) in 25 mM HEPES (4(-2-hydroxyethyl)-1-piperazineethanesulfonic acid, pH 7.4) buffer containing 1 mM EDTA, 1 mM dithiothreitol and 1% glycerol for one h, then quenched with 15 µl of 1 M glycine.

Untreated and BS^3 treated samples were subjected to SDS-PAGE (12% gel) and the protein bands of interest were excised with a clean razor blade and chopped into ~1-mm^3 pieces. The gel fragments were washed with 100 µl of 100 mM NH_4HCO_3 buffer (pH 8.4) for 5 min, dehydrated at room temperature in 50 µl of 100% acetonitrile, and rehydrated in 50 µl of 10 mM dithiothreitol in 100 mM NH_4HCO_3 at 56°C for one h. Dehydration and rehydration was repeated, with final rehydration in 50 µl of 55 mM iodoacetamide in 100 mM NH_4HCO_3. The mixtures were incubated at room temperature and in the dark for one h. Samples were repeatedly washed with 50 µl of 100 mM NH_4HCO_3, dehydrated, rehydrated in 20 µl 50 mM NH_4HCO_3 containing 15 ng/µl of sequencing grade trypsin (Promega), and incubated overnight at 37°C. Supernatants from the trypsin digest were saved, and the gel pieces were sonicated three times with 50 µl of 60% acetonitrile/1% trifluoroacetic acid in an ice water bath for 5 min followed by centrifugation. The solutions were pooled with the initial supernatant, dried to ~2 µl in a Speed Vac, and dissolved in 20 µl of 2% acetonitrile/0.1% trifluoroacetic acid. The final samples were desalted using C-18 pipette tip columns (Agilent Technologies).

MALDI-TOF MS was performed using a Shimadzu Axima plus instrument equipped with a nitrogen laser operating at 337 nm. Samples (5 µl) were mixed with 5 µl of a saturated α-cyano-4-hydroxycinnamic acid solution (Sigma) in 50% acetonitrile containing 0.1% trifluoroacetic acid. Aliquots (1 µl) were spotted on a MALDI plate and allowed to dry in a hood. Spectra were obtained in linear positive mode and externally calibrated with bradykinin fragment

(1-7, RPPGFSP, 756.86 Da), angiotensin I (1296.48 Da), and human ß-chain insulin (3495.95 Da). The mass values at the centroid peak positions are reported, i.e. the average value across the isotopic peaks.

MS Analysis of Intact Protein Complexes. Samples containing UreABC, MBP-UreDFG and its K165A UreF version, UreABC:MBP-UreDFG and its K165A UreF version, and UreABC:UreDFG (where UreG is fused to *Strep*-tag II) with protein concentrations of 0.5 mg/ml were buffer exchanged into 200 mM ammonium acetate buffer using Micro Bio-Spin 6 columns (Bio-Rad, Hercules, CA) just prior to MS analysis. A quadrupole-ion mobility (IM)-TOF MS instrument (Synapt G2 HDMS; Waters, Milford, MA) was used to collect the intact protein complex data. Protein ions were typically generated by nano-electrospray ionization (nESI) using a capillary voltage of 1.5-1.7 kV. Ions traveled through a mass-selective quadrupole and entered an ion trap constructed from a traveling wave ion guide, pressurized at 3×10^{-2} mbar of argon. Ions were then released from the trap cell into the IM separator pressurized with 2.7 mbar of N_2. Typical settings for the traveling waves within the IM drift region were 150 m/s wave velocity and a wave height of 15 V (46). Ions underwent *m*/*z* separation in a TOF mass analyzer, which was maintained at a vacuum of 1.7×10^{-6} mbar, and operated using a mass range of 500 to 25,000 *m*/*z*. All other instrument parameters were tuned to preserve fragile non-covalent protein interactions (8, 19, 36).

Tandem MS experiments were carried out to increase the confidence of the protein stoichiometries and compositions assigned from intact mass alone. Ions of interest were generated in the same fashion as above and then a single *m*/*z* was selected in the quadrupole mass filter. Charge states selected for such dissociation experiments varied from complex to complex, but typically those signals that presented the least overlap with other protein complex

ions having similar *m*/*z* and those with the greatest intensity values were chosen for tandem MS. Following isolation, ions were given excess kinetic energy upon accelerating into the ion trap region prior to the IM drift cell by increasing the acceleration voltage to 200 V. These data are presented with minimal smoothing and no background subtraction.

RESULTS AND DISCUSSION

Characterization of the MBP-UreDFG Complex. Of the protein complexes illustrated in Figure 2.1, the least well studied is UreDFG due to its insolubility (31). To overcome this hurdle, the maltose binding protein (MBP) fusion with UreD (MBP-UreD, known to be functional for urease activation in the cell) was used to obtain a soluble hetero-trimeric complex abbreviated here as MBP-UreDFG (9, 11). As an initial step in characterizing this species, the sample was digested with thrombin to remove the MBP tag; however, the resulting MBP-free urease subunits precipitated quickly after ($t < 1$ hr, data not shown), so further investigations focused on the properties of the intact MBP-UreDFG complex. SDS-PAGE analysis of purified sample (Figure 2.2A, lane 1) revealed the expected three bands (72,892, 25,222, and 21,944 Da, respectively, according to their sequences; note that UreG migrates anomalously during SDS-PAGE and is positioned above UreF), and division of the integrated band intensities by their relative masses indicated the components were present at nearly equivalent ratios. Gel filtration analysis provided an apparent relative mass of ~275 kDa (data not shown), consistent with a $(\text{MBP-UreDFG})_2$ quaternary structure (predicted sequence mass of 240,116 Da). Furthermore, there was no evidence of an equilibrium involving a single heterotrimeric species or of dissociation into the individual protein subunits.

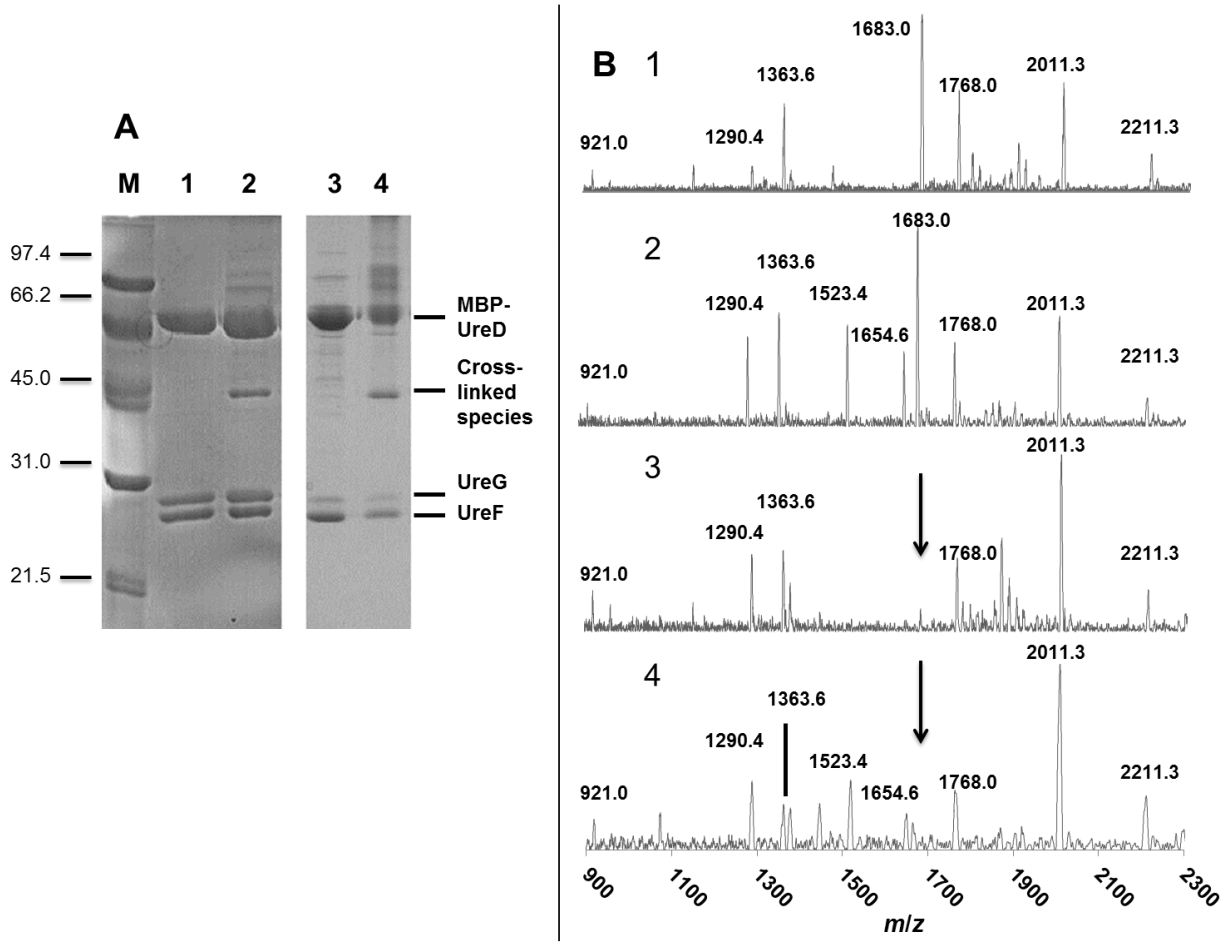

Figure 2.2: MALDI-TOF MS analysis of chemically cross-linked MBP-UreDFG. (A) SDS-PAGE analysis of samples. Lanes: M, molecular mass markers (in kDa); 1, MBP-UreDFG (19.2 µg); 2, MBP-UreDFG (19.2 µg) treated with BS_3 (0.9 µg); 3, MBP-UreD:UreF(K165A):UreG (9.0 µg); 4, MBP-UreD:UreF(K165A):UreG (9.0 µg) treated with BS_3 (6.9 µg). Note that UreG migrates anomalously slowly for its known mass. (B) MALDI-TOF MS of in-gel trypsin digests of bands from panel A. Spectra: 1, UreF; 2, ~45 kDa band from cross-linked MBP-UreDFG; 3, UreF(K165A); 4, ~45 kDa band of cross-linked MBP-UreD:UreF(K165A):UreG. Theoretical digest fragments of UreF include *m*/*z* 921.0 (residues 214-220), 1290.4 (70-81, carbamido-methylated), 1363.6 (181-191, carbamidomethylated), 1683.0 (166-180, absent in samples for K165A UreF), 1768.0 (109-122, carbamidomethylated), and 2010.3 (192-213). The fragment at *m*/*z* 2211.3 is from trypsin. Cross-links of UreF peptides 2-7 plus 2-7 and peptides 2-7 plus 1-7 have predicted *m*/*z* 1523.4 and 1654.6, respectively.

To further characterize the $(MBP\text{-}UreDFG)_2$ complex, purified sample was subjected to chemical cross-linking with the amine-specific reagent bis(sulfosuccinimidyl)suberate (BS^3) followed by trypsin proteolysis and MALDI-TOF-MS. SDS-PAGE analysis of the complex

treated with BS^3 demonstrated the formation of a species (~44 kDa) that was not present in the untreated sample (Figure 2.2A, lane 2). A mixture of additional less intense bands corresponding to intact protein masses greater than MBP-UreD were detected, but not further characterized. The apparent molecular mass of the ~44-kDa species could be explained by UreF-UreF, UreF-UreG, or UreG-UreG cross-links. Digestion of this band with trypsin and MALDI-TOF-MS analysis of the resulting peptides identified the species as arising solely from UreF, demonstrating a UreF-UreF cross-link. The MALDI-TOF-MS spectrum of tryptic peptides derived from untreated UreF was compared to that for BS^3-treated sample (Figure 2.2B, spectra 1 and 2). Both samples contained a fragment corresponding to residues 166-180 (*m/z* = 1683; LVPFGQQAAQQLILR) arising from cleavage after K165, the only lysine in this protein; thus, cross-linking did not involve this residue. The BS^3-treated sample gave rise to two new tryptic peptides that were both consistent with cross-linking that involves the amino-termini (with partial removal of the initial Met); a peak near *m/z* of 1523 corresponded to two peptides containing residues 2-7 (*m/z* = 692; STAEQR) and the linker region (*m/z* = 140) while that at *m/z* of 1655 linked residues 1-7 (*m/z* = 823) to residues 2-7. Confirmation of the amino-terminal linkages was obtained by similar studies with a variant complex containing K165A UreF, thus lacking free lysine residues. A ~44 kDa band derived from BS^3 cross-linking again was observed by SDS-PAGE (Figure 2.2A, lanes 3 and 4). MALDI-TOF-MS analysis (Figure 2.2B, spectra 3 and 4) again revealed the presence of fragments with *m/z* of 1523 and 1655, but a fragment with *m/z* of 1683 was absent, consistent with a lack of proteolytic cleavage after the altered residue. These results demonstrate a close juxtaposition of the amino termini of two UreF peptides in $(MBP\text{-}UreDFG)_2$.

The addition of excess urease holoenzyme or apoprotein to $(MBP\text{-}UreDFG)_2$ or its UreF(K165A) derivative led to the formation of pre-activation complexes that were separated from free urease by amylose affinity chromatography (Figure 2.3). This procedure allowed for further structural studies of the pre-activation complex.

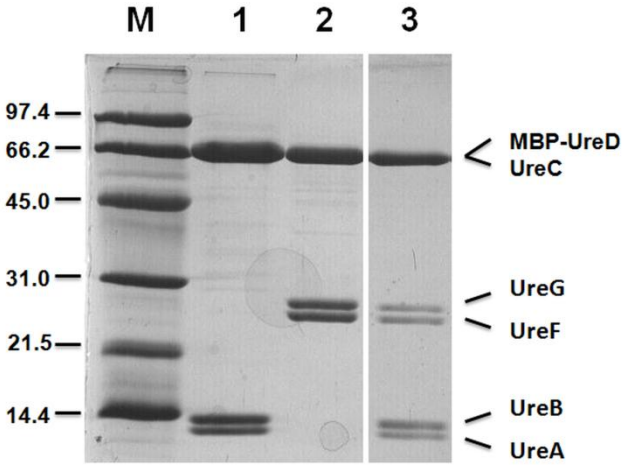

Figure 2.3: Interaction of MBP-UreDFG with urease. Lanes: M, molecular mass markers (in kDa); 1, Urease apoprotein (8.8 µg); 2, MBP-UreDFG (4.7 µg); 3, 1/20th of the elution fraction (10 mM maltose in 20 mM Tris buffer, pH 7.8, containing 85 mM NaCl and 1 mM EDTA) from an amylose resin after applying a mixture of urease apoprotein and MBP-UreDFG (207 µg and 41.6 µg, respectively; incubated 1 h, in the same buffer), washing with maltose-free buffer, and eluting with buffer containing maltose.

MS Analysis of Intact Urease Complexes. To examine the composition and connectivity of protein complexes along the urease activation pathway in more detail, MS measurements were conducted on numerous urease-related samples under conditions designed to retain fragile, non-covalent interactions in the gas-phase (4, 5, 18-20, 37, 40). Through the proper tuning of the nESI process, as well as the correct managing of both pressure and focusing potentials within the instrument, MS enables the measurement of heterogeneous multiprotein assemblies at low micromolar concentrations with unprecedented precision and accuracy (17). Errors in this mass measurement arise primarily from buffer material that adheres to the surface of protein ions created by gentle nESI, resulting in expected positive deviations between experimentally

determined and expected molecular masses of <3% (4, 28). Once sufficient signal intensity is achieved, tandem MS approaches, involving collision induced dissociation (CID), can be employed on multiprotein complex ions (2, 3, 38). The fragment ions produced typically take the form of highly-charged monomeric subunits and charge-reduced assemblies stripped of the aforementioned monomers (13). If these data are combined with ion mobility (IM) spectrometry, which enables the separation of protein complex ions based on their orientationally averaged size and shape, then closely-related assemblies can be individually analyzed and identified (36, 41, 47). While the data shown here were acquired in an IM-MS mode, and in many cases the IM data were used to guide the MS analysis and differentiate overlapping charge state distributions resulting from assemblies of similar intact mass, only the resulting MS data and its analysis are discussed here. Limited IM-MS data comparing the stability differences observed between holo-enzyme and apo-protein complexes are available in Figure 2.4, with complexes containing holo-enzymes demonstrating superior stability. Sample IM-MS data enabling a more-detailed analysis of the tandem MS datasets is displayed in Figure 2.5.

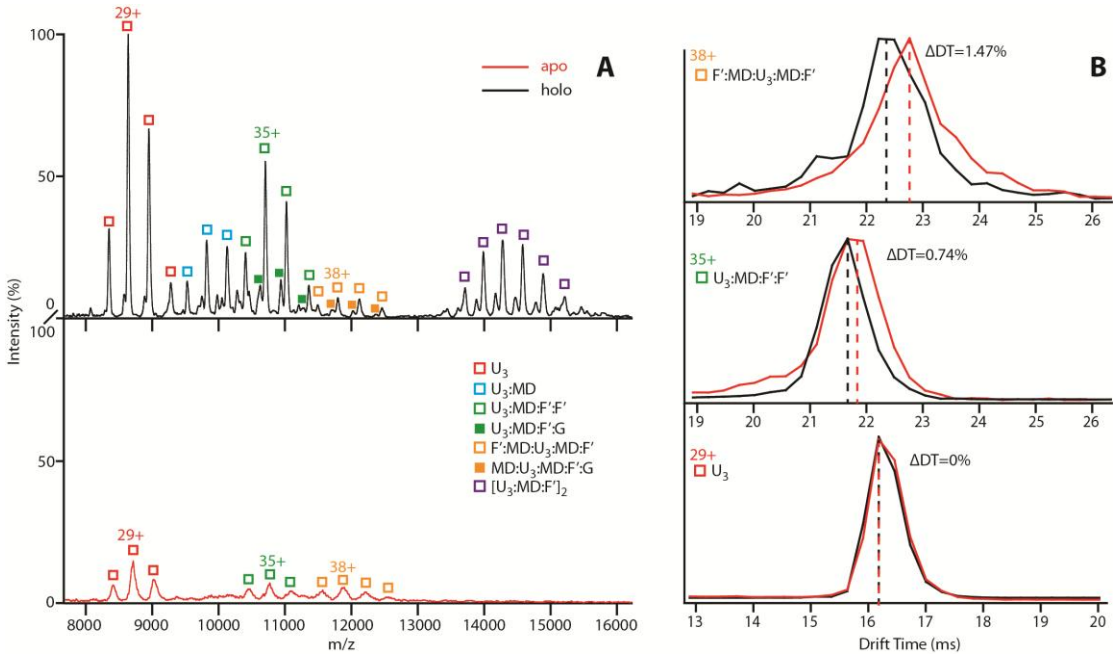

Figure 2.4: Comparing the stability and size differences observed between holo-enzyme and apo-protein complexes by IM-MS. (A) Mass spectra for holo-enzyme (top) and apo-protein (bottom) urease samples containing MBP-UreD:UreF(K165A):UreG indicate that complexes involving Ni^{2+} bound species show high signal intensity, demonstrating remarkably superior stability. (B) Drift time distributions of the equal charge state of holo-enzyme/apo-protein $(UreABC)_3$ alone and in accessory protein-bound complexes provide side-by-side comparisons of their sizes. Despite the slight difference in drift time (<1.5%), I observed a trend that the holo-protein complexes get increasingly more compact than the apo-protein forms upon binding of accessory proteins. While these differences are negligible for U_3 complexes (bottom panel) they are significant and reproducible for larger assemblies (top two panels). All centroid IM data shown are derived from Gaussian fits to the observed arrival time distributions and carry a relative standard deviation of 0.2%. Drift time, $(UreABC)_3$, MBP-UreD, UreF(K165A) and UreG are abbreviated as DT, U_3, MD, F' and G, respectively.

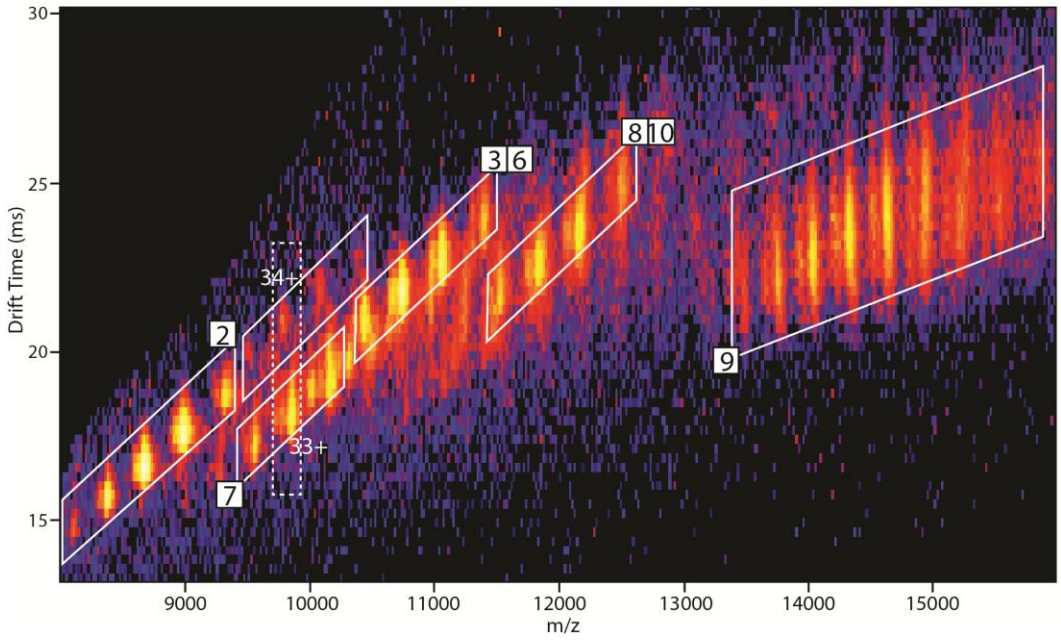

Figure 2.5: IM-MS data for the urease-related species that appear in Figure 2.6. A contour plot of *m/z* versus drift time is shown. A narrow window that contains 33^+ ions of $(UreABC)_3$:MBP-UreD (No. 7) and 34^+ ions of $(UreABC)_3$:MBP-UreD:UreF missing one UreB subunit is highlighted (dotted box). These two species have similar *m/z* (~5% difference) and thus were likely co-isolated in quadrupole during MS/MS acquisition.

To test if the accessory protein complex binds to urease as the dimeric species or whether one heterotrimer binds while the other dissociates, these components were incubated under conditions where urease was in three-fold excess and the products were analyzed by MS (Figures 2.6A-E). Figure 2.6E serves as a framework for describing the results. MBP-UreDFG (species No. 1) in a 200 mM ammonium acetate solution yielded the well-resolved charge state series in the mass spectrum of Figure 2.6D. This species had an intact mass corresponding to the expected value for $(MBP\text{-}UreDFG)_2$ (240,482 ±21 Da measured and 239,856 Da expected). No indication of a single heterotrimer, free UreF, or UreF:UreF dimer was detected (see also Figure 2.7). The observation of this overall dimeric species corroborates the dimerization suggested by gel filtration analysis and MALDI-MS data that had indicated UreF-UreF cross-linking (Figure 2.2). Significantly, individual heterotrimeric units of this dimer bind to the core urease assembly

$(UreA:UreB:UreC)_3$ (Figure 2.6A, No. 2) to create a $(UreABC)_3$:MBP-UreDFG assembly (Figure 2.6A, No. 3). A hypothetical pathway for synthesis of this species is illustrated in Figure 2.8.

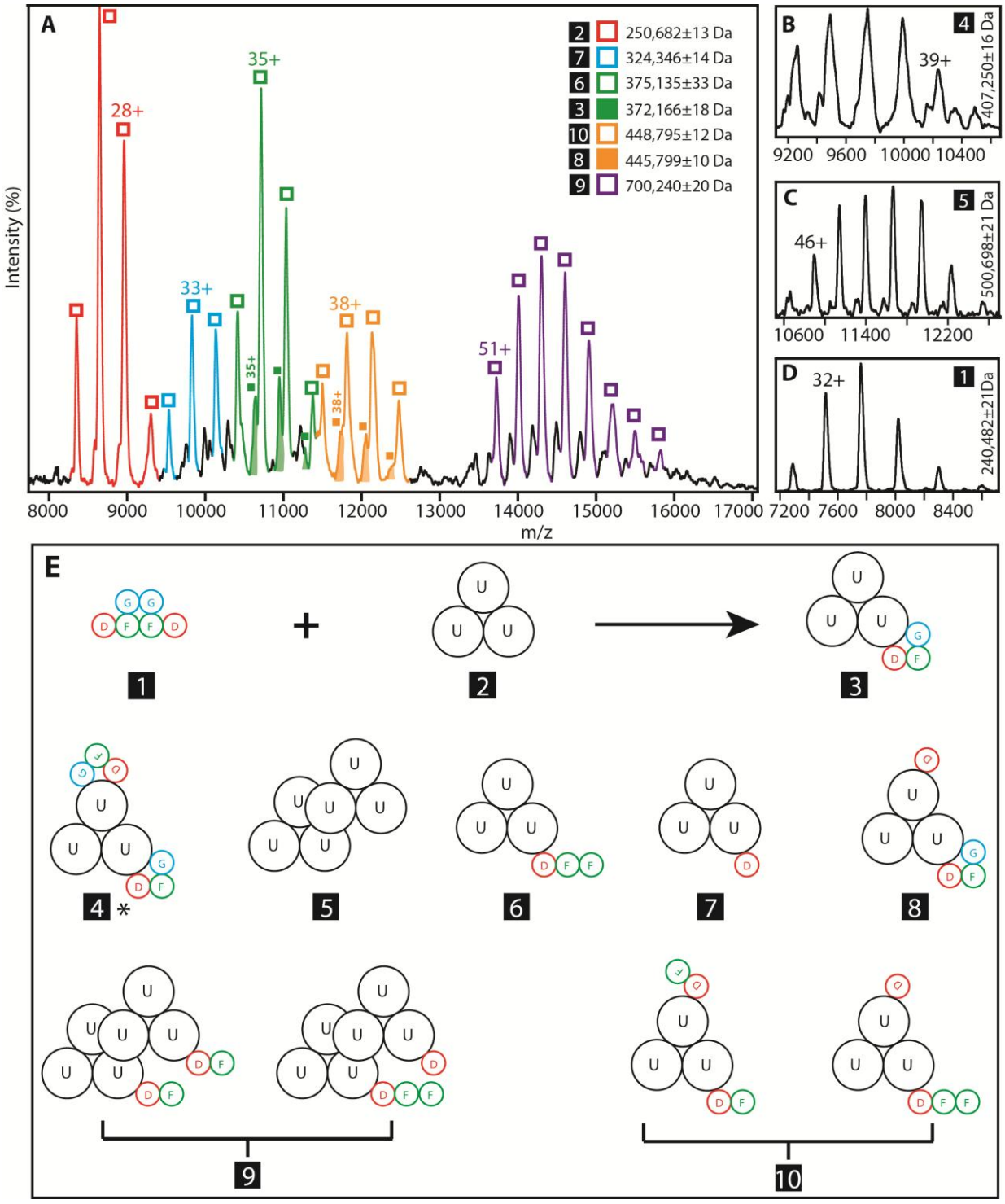

Figure 2.6: Intact complexes of MBP-UreDFG and urease as probed through ESI-MS. (A), (B), (C) and (D) are mass spectra recorded for various stabilized urease complexes discussed in the text. (E) Topological diagrams of the complex stoichiometries identified by ESI-MS, where structures are indicated by numbers 1-10. MBP-UreD, UreF, and UreG are abbreviated as D, F, and G, except for complex No. 4 which was isolated directly from cells, lacks MBP-tagged UreD, and has UreF containing *Strep*-tag II (labeled 4*). Depicted topologies are congruent with

Figure 2.6 (cont'd): the experimental observations and other structural information known for these assemblies. High confidence data from this work strongly indicates that complexes 1 and 2 form primarily complex 3 *in vitro*. Additional protein complexes are also observed, but likely result from the dissociation of higher-order complexes, and not from intermediates in the assembly of urease activation complexes. Complexes No. 9 and No. 10 each have at least two possible topologies that match the ESI-MS data (as shown).

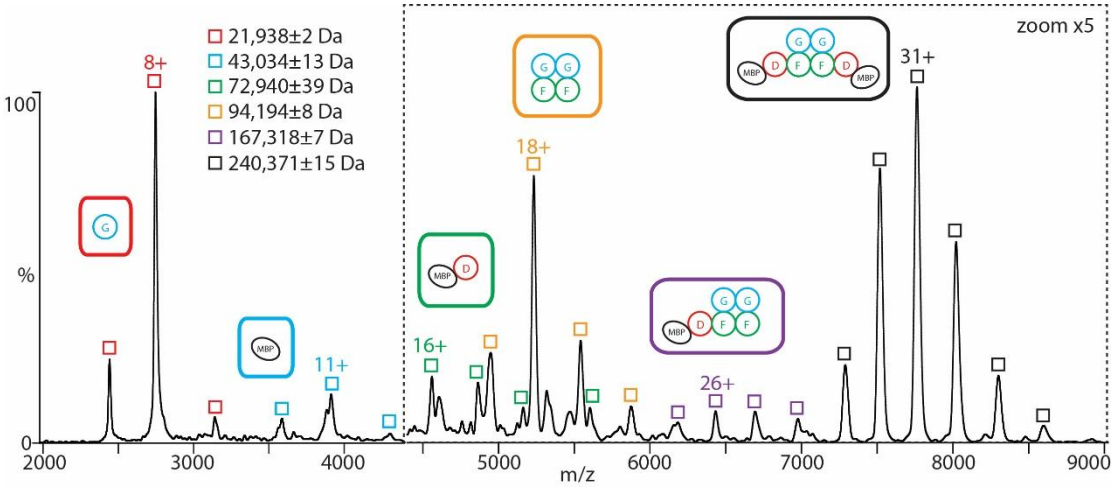

Figure 2.7: Mass spectrum recorded for MBP-UreD:UreF:UreG at pH 6.9. The charge states and schematic topologies for the complexes are indicated in matching colors. No free MBP-UreD:UreF:UreG, monomeric UreF or dimeric UreF is observed under any solution condition studied here, which strongly supports a urease activation complex assembly mechanism that does not involve the addition of discrete UreF, and consequently UreG, proteins to the core complex under *in vitro* incubation conditions. The spectra are magnified 5 fold above 4400 m/z. Maltose binding protein, UreD, UreF and UreG are abbreviated as MBP, D, F, and G, respectively.

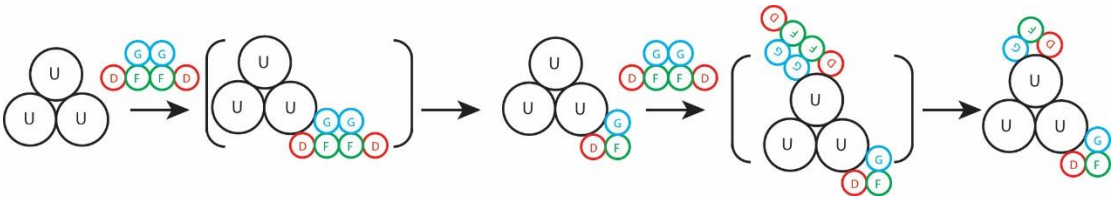

Figure 2.8: A likely assembly pathway for the urease activation complex. This scheme is most consistent with the MS data, in which the $(UreD:UreF:UreG)_2$ complex transiently binds to $(UreABC)_3$, and then dissociates to leave one UreD:UreF:UreG unit bound to the core urease complex (i.e., No. 1 plus No. 2 yields No. 3, Figure 2.6E). Successive $(UreD:UreF:UreG)_2$ binding is required to load additional copies of UreD:UreF:UreG onto $(UreABC)_3$, resulting in complex No. 4 (Figure 2.6E), as observed for sample directly purified from the cell. One hetero-trimer unit of $(UreABC)_3$, UreD, UreF and UreG are abbreviated as U, D, F and G, respectively.

Figure 2.6A also provides evidence of other protein complexes that presumably represent incompletely synthesized, partially decomposed, or aggregated assemblies. These include (but are not limited to): the $(UreABC)_3$ central complex bound to MBP-UreD:UreF:UreF (No. 6), to one copy of MBP-UreD (No. 7), or to two copies of MBP-UreD:UreF (No. 10, alternatively depicted as one copy of MBP-UreD and one copy of MBP-UreD:UreF:UreF), and complex No. 3 with an additional MBP-UreD (No. 8). For a different sample purified directly from the cells (rather than generated by mixing purified proteins in solution), I detected a complex with two copies of UreDFG (lacking MBP and with UreG fused to *Strep*-tag II) bound to urease (No. 4*, Fig 2.6B). The addition of a second $(UreDFG)_2$ to the complex marked as No. 3, indicated as a second transient species in brackets in Figure 2.8, is likely needed to satisfy the formation of several of these assemblies. Alternatively, complexes No. 7 and 8, as well as some possible topologies of complexes No. 9 and 10 can be formed through the binding of excess MBP-UreD to smaller assemblies. MS data reveal additional complexes which result from the oligomerization of $(UreABC)_3$ to form $((UreABC)_3)_2$ (Figure 2.6A, No. 5) and that same complex bound to two copies of MBP-UreD:UreF (No. 9, alternatively depicted as one MBP-UreD and one MBP-UreD:UreF:UreF). Due to the low working concentration of the samples used in the MS analysis of these intact complexes (<10 μM), it is unlikely that these larger oligomers can be described as artifacts of the nESI process.

All of the identifications discussed above are supported with tandem MS data, where CID generates fragment ions that enable the high-confidence assignment of the protein complex composition and stoichiometry. Figure 2.9 shows selected tandem MS spectra, using the same numerical identifiers as used in Figure 2.6 to refer to the assemblies originally isolated for gas-phase dissociation. In all cases shown, multiple stripped protein populations are observed and

rationalized based on the monomer components known to exist within each sample and the intact mass of the isolated protein complex ion (Table 2.1). In the cases of Figures 2.9B, C, D and E, for example, two overlapping protein complex ion populations are co-isolated in each dataset due to their similar intact *m*/*z* values (Figure 2.6A), and they produce fragment ion populations that allow for their discrete identification. In contrast, fragment ions recorded in Figure 2.9A correspond to complex No. 2 and a previously undetected putative truncated form present at low relative abundance. I also observed signals in the tandem MS data corresponding to multiple dissociated monomers, dominated by signals from UreB and UreF at low *m*/*z* in Figures 2.9B, C, D and E. For example, the ejection energies for UreF and UreB from complex No. 9 are similar, resulting in two prominent stripped protein ion populations (indicated by open purple circles and squares) in Figure 2.9E. In contrast, UreF and UreB are ejected at significantly different collision energies for complex No. 3 versus No. 6 or complex No. 8 versus No. 10, thus aiding the interpretation of the recorded CID patterns (Figure 2.9C and D).

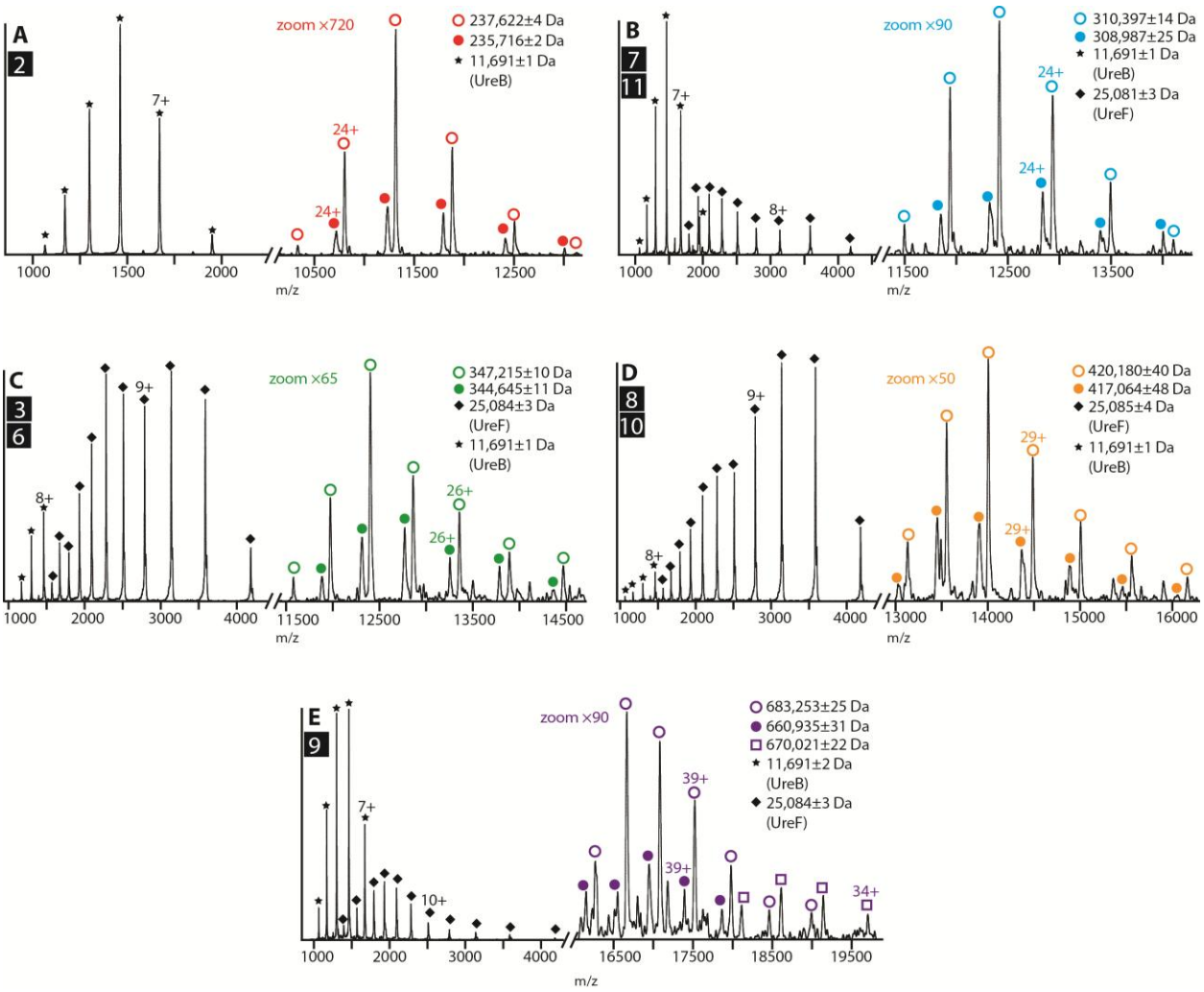

Figure 2.9: Protein complex identification through precise mass measurements enabled by tandem MS. Tandem MS CID spectra recorded for the urease-related species that appear in Figure 2.6B, acquired at a trap collision voltage of 200 V (A, B, C, D and E). CID spectra are typically dominated by signals for ejected UreB and UreF monomers at low *m/z*, indicated by star and diamond notations respectively, while the signals corresponding to stripped protein complex ions at high *m/z* are magnified (magnification factors indicated on each spectrum) and marked by color-coded circles. Detailed annotations are given in Table 2.1.

Table 2.1: A list of measured masses determined from primary MS and tandem MS (MS/MS) data, and sequence masses for the urease-related species that appear in Figure 2.6A. The sequence masses correspond to the urease apo-protein complexes, which can be converted to the urease holo-enzyme species by adding 496 Da (6 nickel ions and 3 CO_2 molecules) to the intact masses shown. Such small differences in masses cannot be resolved for the complexes shown here using our instrumentation. Good agreement is found between measured masses derived from MS/MS data and the sequence masses of the assigned complexes in each panel of Figure 2.9. The same marks are indicated such that the dissociated monomers and stripped complexes can correspond to their peaks shown in Figure 2.9. $(UreABC)_3$, UreD, MBP-UreD, UreD, UreF and UreG are abbreviated as U_3, B, MD, D, F and G, respectively.

Figure No.	measured mass (Da)				sequence mass (Da)	protein species	
	MS	MS/MS					
		dissociated	stripped	sum			
Fig. 5A	250,682±13	11,691±1 B ★	237,622±4 ○	249,313±5	249,260	U_3	2
	248,878±59	11,691±1 B ★	235,716±2 ●	247,407±3		truncated U_3	
Fig. 5B	324,346±14	11,691±1 B ★	310,397±14 ○	322,088±15	322,161	U_3:MD	7
	341,771±10	25,081±3 F ◆	308,987±25 ●	334,068±28	335,549	(U_3-B):MD:F	
Fig. 5C	375,135±33	25,084±3 F ◆	347,215±10 ○	372,299±13	372,336	U_3:MD:F:F	6
	372,166±18	25,084±3 F ◆	344,645±11 ●	369,729±14	369,188	U_3:MD:F:G	3
Fig. 5D	448,795±12	25,085±4 F ◆	420,180±40 ○	445,265±44	445,228	F:MD:U_3:MD:F	10
	445,799±10	25,085±4 F ◆	417,064±48 ●	442,149±52	442,023	MD:U_3:MD:F:G	8
Fig. 5E	700,240±20	11,691±2 B ★	683,253±25 ○	694,944±27	694,488	$[U_3$:MD:F$]_2$	9
	700,240±20	25,084±3 F ◆	670,021±22 □	695,105±25	694,488	$[U_3$:MD:F$]_2$	9
	679,960±27	11,691±2 B ★	660,935±31 ●	672,626±33		truncated $[U_3$:MD:F$]_2$	

Surprisingly, Figure 2.9B contains signals corresponding to both UreB and UreF though the complex I intended to isolate (No. 7) contains only the former as a constituent. Using IM-MS data to guide my interpretation, however, I discovered that the 33^+ charge state of complex No. 7 and the 34^+ charge state of $(UreABC)_3$:MBP-UreD:UreF lacking one UreB subunit coexist in the dataset and possess *m*/*z* values that cannot be distinguished by the quadruple MS (Figure 2.5). The latter complex contains UreF, and thus accounts for the appearance of those signals in Figure 2.9B.

Overall, the specific datasets shown clearly assign the stoichiometries and compositions

of the complexes indicated in Figure 2.6E. By summing the fragment ion population masses observed in Figure 2.9, I obtained intact complex masses that closely agree with the sequence masses for the protein constituents indicated (see Table 2.1). Nevertheless, protein complex topology is not established in all cases. For example, in addition to the two versions shown for species No. 9 one could alternatively position both MBP-UreD:UreF units (or the MBP-UreD and MPB-UreD:UreF:UreF units) on the same urease trimer; however, a urease:MBP-UreD:UreF:UreF:MBP-UreD:urease arrangement is excluded by the CID results. Similarly, two versions are shown for species No. 10, whereas the CID data preclude a single MBP-UreD:UreF:UreF:MBP-UreD unit bound to the urease. In other cases where many possible protein complex topologies occupy the same molecular mass, results from multiple samples under different conditions inform my assignments. A hypothetical assembly pathway that is most consistent with the MS data is depicted in Figure 2.8.

The soluble $(MBP\text{-}UreDFG)_2$ complex derived from the *K. aerogenes* proteins is an overall dimer, compatible with the previously reported $(UreF)_2$ and $(UreH{:}UreF)_2$ structures of the *H. pylori* proteins (15, 24). Furthermore, the chemical cross-linking results demonstrate a close juxtaposition (BS_3 forms a crosslink of 11.4 Å) of the amino termini of the two UreF protomers within this complex. This result also is consistent with the published structural results; the first 25 residues of *H. pylori* UreF are unstructured, but the shorter *K. aerogenes* protein lacks these residues and its dimer is predicted to have the two amino termini on the same protein face with the first four residues of each protomer likely to have substantial flexibility. The $(MBP\text{-}UreDFG)_2$ complex binds to the urease apoprotein and, unexpectedly, to the urease holoenzyme. The dimeric structure of $(MBP\text{-}UreDFG)_2$ raised the question of whether the intact species binds to urease or if it dissociates to form a heterotrimeric species upon binding.

The intact protein complex MS results display a number of features related to urease structure and stability that confirm both the chemical cross-linking and SDS-PAGE data, as well as previously reported findings. First, the loss of UreB from urease (Figure 2.9A) and several of its complexes (e.g., Figure 2.9B-E) may relate to its proposed weak interaction with UreC, providing access to the nascent active site (35). Second, even though UreF can be cross-linked to UreB in the (UreABC):UreD:UreF complex (12), previous data indicated UreF to be relatively weakly bound to the urease core complex (11); these findings suggest that UreF uses UreD as a scaffold to bind to urease rather than having a significant region of direct interface. This weak binding is observed both in the stoichiometry of the complexes recorded in the intact MS dataset that are most-likely formed through UreF dissociation, specifically the conversion between complexes No. 6 to 7 and No. 4 to 8 (Figure 2.6), and the tandem MS data, which showed several instances of the preferential ejection of UreF over other proteins upon collisional activation in the gas phase. This is specifically seen in the cases of complexes No. 3, 6, 8, 9, and 10, despite the constant presence of the much smaller UreB, the ejection of which is favored in $(UreABC)_3$ CID. Furthermore, the intact protein complex MS data strongly indicate the formation of a UreF dimer within $(MBP\text{-}UreDFG)_2$, primarily through the observation of complex No. 6, which is also consistent with the MALDI-MS cross-linking data (Figure 2.2). In general, MS data obtained with intact protein complexes also agree well with the gel filtration analysis, in that the stoichiometry of the MBP-UreDFG complex determined through both techniques is identical.

In addition to these aspects of commonality, intact protein complex MS analysis reveals unique aspects of urease-related structures and enzyme activation that were previously unknown. I found substantial evidence for protein complexes that are likely off-pathway in the formation of

activated urease. Complexes such as No. 6, 7, 8, and 10 all represent assemblies that could possibly result from the decay of the core urease complex bound to one or two MBP-UreDFG. In addition, complexes No. 5 and 9 appear to result from the dimerization of either $(UreABC)_3$ or $(UreABC)_3$:MBP-UreD:UreF, and are also likely to represent off-pathway assemblies. Of potential interest, the hexameric architecture of urease subunits in these species is reminiscent of jack bean urease, which is a hexameric enzyme (1). To account for all of the subcomplexes and decay products observed in the intact protein complex MS data, I invoked sequential $(MBP\text{-}UreDFG)_2$ additions to the core urease complex to generate complexes No. 3 and 4 (Figure 2.8), both of which are likely to lie on the activation pathway for the enzyme. I presume that incubation of $(MBP\text{-}UreDFG)_2$ in great excess over $(UreABC)_3$ would lead to addition of a third MBP-UreDFG unit to the enzyme; however, the experiment was designed to test for the presence of No. 3 rather than larger complexes that would less clearly address the question. Each of the pre-activation complexes appears to undergo dissociation under the analytical conditions to produce other partially assembled complexes that are unlikely to contribute to urease activation. Significantly, however, $(MBP\text{-}UreDFG)_2$ does not dissociate to yield MBP-UreD:UreF:UreG, free UreF, or UreF:UreF dimer (Figure 2.7), suggesting that these species are not available and do not add to urease during the *in vitro* incubation studies. The observed assemblies are present over relatively long time-scales (hours/days), suggesting that the complexes identified in Figure 2.6 are all relatively stable forms of these proteins *in vitro*.

CONCLUSIONS

I present here unique data on the urease activation complexes formed between the $(UreABC)_3$ core assembly and a complex comprised of UreD, UreF, and UreG. The MS data of the intact urease assemblies involved in enzyme activation are supported by measurements

involving SDS-PAGE, gel filtration, chemical cross-linking, and IM separations. First, I detected clear evidence that a $(UreDFG)_2$ complex with juxtaposed UreF subunits is the primary biological unit generated by UreD, UreF and UreG under the experimental conditions. Secondly, I detected the stepwise addition of UreDFG units to the core $(UreABC)_3$ assembly upon exposure to $(UreDFG)_2$ in solution, or from complexes isolated directly from cells. These $(UreABC)_3(UreDFG)$ and $(UreABC)_3(UreDFG)_2$ assemblies are on route to the putative, fully-assembled pre-activation complex shown in Figure 2.1 through the addition of UreDFG units. This result, therefore, lends credence to a urease activation mechanism in which UreDFG binds to urease apoprotein (Figure 2.1, bottom track), but does not preclude the sequential protein binding pathway (Figure 2.1, top). Importantly, these findings are inconsistent with the repeatedly seen UreF:UreF interaction remaining intact. Finally, I also observed evidence for many off-pathway complexes that appear in high abundance in the intact MS measurements, suggesting either the relative fragility of the pre-activation urease complexes probed, or the likely complexity of the activation process. Future work in this area will likely capitalize on the data shown here to further probe the structures and stabilities of urease activation complexes, and eventually construct a complete map of their assembly *in vivo*.

BIBLIOGRAPHY

BIBLIOGRAPHY

1. **Balasubramanian, A., and Ponnuraj, K.** 2010. Crystal structure of the first plant urease from jack bean: 83 Years of journey from its first crystal to molecular structure. J. Mol. Biol. **400**: 274-283.

2. **Benesch, J. L. P.** 2009. Collisional activation of protein complexes: Picking up the pieces. J. Am. Soc. Mol. Biol. **20**: 341-348.

3. **Benesch, J. L. P., Aquilina, J. A., Ruotolo, B. T., Sobott, F., and Robinson, C. V.** 2006. Tandem mass spectrometry reveals the quaternary organization of macromolecular assemblies. Chem. Biol. **13**: 597-605.

4. **Benesch, J. L. P., and Ruotolo, B. T.** 2011. Mass spectrometry: Come of age for structural and dynamical biology. Curr. Opin. Struct. Biol. **21**: 641-649.

5. **Benesch, J. L. P., Ruotolo, B. T., Simmons, D. A., and Robinson, C. V.** 2007. Protein complexes in the gas phase: Technology for structural genomics and proteomics. Chem. Rev. **107**: 3544-3567.

6. **Boer, J. L., and Hausinger, R. P.** 2012. *Klebsiella aerogenes* UreF: Identification of the UreG binding site and role in enhancing the fidelity of urease activation. Biochemistry **51**: 2298-2308.

7. **Boer, J. L., Quiroz-Valenzuela, S., Anderson, K. L., and Hausinger, R. P.** 2010. Mutagenesis of *Klebsiella aerogenes* UreG to probe nickel binding and interactions with other urease-related proteins. Biochemistry **49**: 5859-5869.

8. **Bush, M. F., Hall, Z., Giles, K., Hoyes, J., Robinson, C. V., and Ruotolo, B. T.** 2010. Collision cross sections of proteins and their complexes: A calibration framework and database for gas-phase structural biology. Anal. Chem. **82**: 9557-9565.

9. **Carter, E. L., Boer, J. L., Farrugia, M. A., Flugga, N., Towns, C. L., and Hausinger, R. P.** 2011. Function of UreB in *Klebsiella aerogenes* urease. Biochemistry **50**: 9296-9308.

10. **Carter, E. L., Flugga, N., Boer, J. L., Mulrooney, S. B., and Hausinger, R. P.** 2009. Interplay of metal ions and urease. Metallomics **1**: 207-221.

11. **Carter, E. L., and Hausinger, R. P.** 2010. Characterization of *Klebsiella aerogenes* urease accessory protein UreD in fusion with the maltose binding protein. J. Bacteriol. **192**: 2294-2304.

12. **Chang, Z., Kuchar, J., and Hausinger, R. P.** 2004. Chemical crosslinking and mass spectrometric identification of sites of interaction for UreD, UreF, and urease. J. Biol. Chem. **279**: 15305-15313.

13. **Erba, E. B., Ruotolo, B. T., Barsky, D., and Robinson, C. V.** 2010. Ion mobility-mass spectrometry reveals the influence of subunit packing and charge on the dissociation of multiprotein complexes. Anal. Chem. **82**: 9702-9710.

14. **Farrugia, M. A., Macomber, L., and Hausinger, R. P.** 2013. Biosynthesis of the urease metallocenter. J. Biol. Chem. **288**: 13178-85.

15. **Fong, Y. H., Wong, H. C., Chuck, C. P., Chen, Y. W., Sun, H., and Wong, K.-B.** 2011. Assembly of the preactivation complex for urease maturation in *Helicobacter pylori*: Crystal structure of the UreF/UreH protein complex. J. Biol. Chem. **286**: 43241-43249.

16. **Gasper, R., Scrima, A., and Wittinghofer, A.** 2006. Structural insights into HypB, a GTP-binding protein that regulates metal binding. J. Biol. Chem. **281**: 27492-27502.

17. **Gingras, A. C., Gstaiger, M., Raught, B., and Aebersold, R.** 2007. Analysis of protein complexes using mass spectrometry. Nat. Rev. Mol. Cell Biol. **8**: 645-654.

18. **Heck, A. J. R.** 2008. Native mass spectrometry: A bridge between interactomics and structural biology. Nat. Methods **5**: 927-933.

19. **Hernandez, H., and Robinson, C. V.** 2007. Determining the stoichiometry and interactions of macromolecular assemblies from mass spectrometry. Nat. Protoc. **2**: 715-726.

20. **Hyung, S. J., and Ruotolo, B. T.** 2012. Integrating mass spectrometry of intact protein complexes into structural proteomics. Proteomics **12**: 1547-1564.

21. **Jabri, E., Carr, M. B., Hausinger, R. P., and Karplus, P. A.** 1995. The crystal structure of urease from *Klebsiella aerogenes*. Science **268**: 998-1004.

22. **Jabri, E., and Karplus, P. A.** 1996. Structures of the *Klebsiella aerogenes* urease apoprotein and two active-site mutants. Biochemistry **35**: 10616-10626.

23. **Laemmli, U. K.** 1970. Cleavage of structural proteins during the assembly of the head of bacteriophage T4. Nature (London) **227**: 680-685.

24. **Lam, R., Romanov, V., Johns, K., Battaile, K., Wu-Brown, J., Guthrie, J. L., Hausinger, R. P., Pai, E., and Chirgadze, N. Y.** 2010. Crystal structure of a truncated urease accessory protein UreF from *Helicobacter pylori*. Proteins **78**: 2839-2848.

25. **Lee, M. H., Mulrooney, S. B., and Hausinger, R. P.** 1990. Purification, characterization, and *in vivo* reconstitution of *Klebsiella aerogenes* urease apoenzyme. J. Bacteriol. **172**: 4427-4431.

26. **Lee, M. H., Pankratz, H. S., Wang, S., Scott, R. A., Finnegan, M. G., Johnson, M. K., Ippolito, J. A., Christianson, D. W., and Hausinger, R. P.** 1993. Purification and characterization of *Klebsiella aerogenes* UreE protein: A nickel-binding protein that functions in urease metallocenter assembly. Protein Sci. **2**: 1042-1052.

27. **Ligabue-Braun, R., Real-Guerra, R., Carlini, C. R., and Verli, H.** 2012. Evidence-based docking of the urease activation complex. J. Biomol. Struct. Dyn. **31**:854-861.

28. **McKay, A. R., Ruotolo, B. T., Ilag, L. L., and Robinson, C. V.** 2006. Mass measurements of increased accuracy resolve heterogeneous populations of intact ribosomes. J. Am. Chem. Soc. **128**: 11433-11442.

29. **Mobley, H. L. T., and Hausinger, R. P.** 1989. Microbial ureases: Significance, regulation, and molecular characterization. Microbiol. Rev. **53**: 85-108.

30. **Moncrief, M. B. C., and Hausinger, R. P.** 1996. Purification and activation properties of UreD-UreF-urease apoprotein complexes. J. Bacteriol. **178**: 5417-5421.

31. **Moncrief, M. B. C., and Hausinger, R. P.** 1997. Characterization of UreG, identification of a UreD-UreF-UreG complex, and evidence suggesting that a nucleotide-binding site in UreG is required for *in vivo* metallocenter assembly of *Klebsiella aerogenes* urease. J. Bacteriol. **179**: 4081-4086.

32. **Park, I. S., Carr, M. B., and Hausinger, R. P.** 1994. *In vitro* activation of urease apoprotein and role of UreD as a chaperone required for nickel metallocenter assembly. Proc. Nat. Acad. Sci. **91**: 3233-3237.

33. **Park, I. S., and Hausinger, R. P.** 1995. Evidence for the presence of urease apoprotein complexes containing UreD, UreF, and UreG in cells that are competent for *in vivo* enzyme activation. J. Bacteriol. **177**: 1947-1951.

34. **Park, I. S., and Hausinger, R. P.** 1995. Requirement of carbon dioxide for *in vitro* assembly of the urease nickel metallocenter. Science **267**: 1156-1158.

35. **Quiroz-Valenzuela, S., Sukuru, S. C. K., Hausinger, R. P., Kuhn, L. A., and Heller, W. T.** 2008. The structure of urease activation complexes examined by flexibility analysis, mutagenesis, and small-angle X-ray scattering. Arch. Biochem. Biophys. **480**: 51-57.

36. **Ruotolo, B. T., Benesch, J. L. P., Sandercock, A. M., Hyung, S. J., and Robinson, C. V.** 2008. Ion mobility-mass spectrometry analysis of large protein complexes. Nat. Protoc. **3**: 1139-1152.

37. **Sharon, M., and Robinson, C. V.** 2007. The role of mass spectrometry in structure elucidation of dynamic protein complexes. Annu. Rev. Biochem. **76**: 167-193.

38. **Sobott, F., and Robinson, C. V.** 2004. Characterising electrosprayed biomolecules using tandem-MS - the noncovalent GroEL chaperonin assembly. Int. J. Mass. Spectrom. **236**: 25-32.

39. **Soriano, A., and Hausinger, R. P.** 1999. GTP-dependent activation of urease apoprotein in complex with the UreD, UreF, and UreG accessory proteins. Proc. Nat. Acad. Sci. **96**: 11140-11144.

40. **Taverner, T., Hernandez, H., Sharon, M., Ruotolo, B. T., Matak-Vinkovic, D., Devos, D., Russell, R. B., and Robinson, C. V.** 2008. Subunit architecture of intact protein complexes from mass spectrometry and homology modeling. Acc. Chem. Res. **41**: 617-627.

41. **Uetrecht, C., Rose, R. J., van Duijn, E., Lorenzen, K., and Heck, A. J. R.** 2010. Ion mobility mass spectrometry of proteins and protein assemblies. Chem. Soc. Rev. **39**: 1633-1655.

42. **Witte, C.-P.** 2011. Urea metabolism in plants. Plant Sci. **180**: 431-438.

43. **Zambelli, B., Musiani, F., Benini, S., and Ciurli, S.** 2011. Chemistry of Ni^{2+} in urease: Sensing, trafficking, and catalysis. Acc. Chem. Res. **44**: 520-530.

44. **Zambelli, B., Musiani, F., Savini, M., Tucker, P., and Ciurli, S.** 2007. Biochemical studies on *Mycobacterium tuberculosis* UreG and comparative modeling reveal structural and functional conservation among the bacterial UreG family. Biochemistry **46**: 3171-3182.

45. **Zambelli, B., Stola, M., Musiani, F., De Vriendt, K., Samyn, B., Devreese, B., Van Beeumen, J., Dikiy, A., Bryant, D. A., and Ciurli, S.** 2005. UreG, a chaperone in the urease assembly process, is an intrinsically unstructured GTPase that specifically binds Zn^{2+}. J. Biol. Chem. **280**: 4684-4695.

46. **Zhong, Y. Y., Hyung, S. J., and Ruotolo, B. T.** 2011. Characterizing the resolution and accuracy of a second-generation traveling-wave ion mobility separator for biomolecular ions. Analyst **136**: 3534-3541.

47. **Zhong, Y. Y., Hyung, S. J., and Ruotolo, B. T.** 2012. Ion mobility-mass spectrometry for structural proteomics. Expert Rev. Proteomics **9**: 47-58.

CHAPTER 3

Characterization of *Klebsiella aerogenes* UreD Variants Reveals a Potential Nickel-Transfer Tunnel for Urease Activation

ABSTRACT

Nickel-containing urease from *Klebsiella aerogenes* requires the accessory proteins UreD, UreF, and UreG, along with the metallochaperone UreE, for proper active site metalation. Earlier efforts had shown that UreE binds to UreG in the presence of nickel, that UreD, UreF, and UreG form a complex, and that the UreD:UreF:UreG complex binds to urease via UreD. *In silico* analysis of the homologous, structurally characterized UreH:UreF:UreG complex from *Helicobacter pylori* identified a putative water tunnel originating from the likely nickel-binding motif in UreG, through UreF, and exiting UreH, but no experimental support for this tunnel was reported. A UreD homology model was created and computationally analyzed to reveal a comparable tunnel with an identical origin at the presumed UreD:UreF interface and several exit points on the opposite face of the protein. *In vivo* activation of urease within cells that produce specific UreD variants which were designed to disrupt or block the putative 34.6 Å internal tunnel resulted in greatly reduced urease specific activities relative to enzyme activated with wild-type UreD, whereas cells producing UreD variants targeted to the alternate tunnel exits or to the protein surface exhibited no appreciable effect on activity. Affinity pull-down studies using cell-free extracts of cultures producing variant forms of UreD along with the other urease components showed no loss of interaction between UreD and either urease or the UreF:UreG accessory proteins. Metal-content analysis of urease enriched from extracts of the activity-deficient cultures demonstrated reduced nickel content for all samples, as well as an increase in zinc and iron incorporation. These findings support the role of UreD as a direct facilitator of nickel transfer into urease by using an internal water tunnel.

INTRODUCTION

It has been estimated that one-third of all proteins contain metals, with ~40% of metalloproteins having metal centers that are essential for catalysis (2, 22, 43). These proteins must overcome several challenges during their synthesis in order to incorporate the proper metal(s) to become functional. An approach to circumvent mismetalation is to use accessory proteins for binding the metal and transferring it into the nascent metalloenzyme active sites (11, 14, 18). Examples of this strategy are seen in the Nif proteins involved in biosynthesis of the FeMoco cofactor of nitrogenase, the Hyp proteins used to generate the [NiFe]-hydrogenase cofactor, the copper chaperone for superoxide dismutase required for copper transfer into the Cu,Zn-superoxide dismutase (11, 24, 44), and the focus here -- the activation of nickel-containing urease.

Urease catalyzes the hydrolysis of urea into ammonia and carbamate, with the latter molecule spontaneously decomposing into a second molecule of ammonia and bicarbonate (18). The enzyme is found in plants, as well as some bacteria, Archaea, algae, and fungi (16, 33, 41, 47). Most ureases use a dinuclear nickel metallocenter for catalysis, though a recent example of a di-iron urease has been characterized (10). Most of our knowledge about the formation of the nickel active site comes from studies of the urease activation machinery of *Klebsiella aerogenes* and *Helicobacter pylori*, as detailed below.

The urease gene clusters from *K. aerogenes* (*ureDABCEFG*) (18) and *H. pylori* (*ureABIEFGH*) (21) are similar, but the encoded proteins exhibit a few important distinctions. The three structural subunits of the *K. aerogenes* enzyme (*Ka*UreA, *Ka*UreB, and *Ka*UreC) are closely related to the two subunits of the *H. pylori* protein (*Hp*UreA is homologous to a fusion of *Ka*UreA and *Ka*UreB, while *Hp*UreB is homologous to *Ka*UreC). The subunits assemble into a

trimer of heterotrimers, (*Ka*UreABC)$_3$, and a tetramer of trimeric heterodimers, ((*Hp*UreAB)$_3$)$_4$, respectively, as shown by their crystal structures (22, 25). In each case, the dinuclear active site is located in the largest subunit and, in the case of the *K. aerogenes* enzyme, access to this site is proposed to be gated by the flexible domain of UreB (8, 25, 40). *Ka*UreD and *Hp*UreH are homologous and neither is soluble when overproduced as an independent protein (19, 38); however, a maltose-binding protein (MBP) fusion to *Ka*UreD (MBP-UreD) is soluble, binds two equivalents of nickel, and partially complements a Δ*ureD* loss of function phenotype *in vivo* (9). *Ka*UreF is insoluble when independently overproduced (4), but it is soluble and functional as the UreE-UreF fusion protein (28). By contrast, *Hp*UreF is soluble, a slightly truncated form was structurally characterized (29), and isothermal titration calorimetry studies demonstrate its nickel-binding ability (53), although no studies have been performed to determine if this metal binding is functionally relevant. *Ka*UreG exists as a soluble monomer that binds one equivalent of nickel or zinc with similar affinities (5, 34), while *Hp*UreG is a monomer in the absence of metal, binds zinc with high affinity leading to dimerization, and binds nickel with low affinity without facilitating dimerization of the protein (3). These proteins act as GTPases during urease activation, although the precise role of GTP hydrolysis in this process remains unclear. UreG Cys and His residues associated with a highly conserved Cys-X-His motif are hypothesized to function as the metal binding site, but substitution of one or both of these residues does not abolish metal binding (4, 54). Crystal structures are known for both *Ka*UreE (48) and *Hp*UreE (46); these are dimeric nickel-binding proteins proposed to deliver nickel for urease activation (15, 37). Metal-ion induced interactions between UreE and UreG have been observed for the proteins from *K. aerogenes*, *H. pylori*, and *Sporosarcina* (formerly *Bacillus*) *pasteurii* (3, 5, 32). Attempts to activate *K. aerogenes* urease *in vivo* in the absence of any one of its accessory

proteins result in the production of inactive enzyme lacking nickel (30, 36). Finally, a proton-gated urea permease (UreI) is produced by *H. pylori* (50), but not *K. aerogenes*.

Interactions among the accessory proteins and the enzyme subunits are critical for urease activation. A UreD:UreF:UreG complex is formed *in vivo* when the three corresponding *K. aerogenes* accessory genes are expressed separately from those encoding the urease structural subunits, though direct studies of this complex were limited due to its low solubility (34). In contrast, a soluble complex is formed with MBP-UreD, producing a $(\text{MBP-UreD:UreF:UreG})_2$ species that dissociates to a monomer of heterotrimers when bound to urease according to size-exclusion chromatography and mass spectrometry studies (17). The crystal structure of the analogous $(\text{UreH:UreF:UreG})_2$ *H. pylori* species is known (20). The surface of UreD/UreH that interacts with urease has not been defined.

While the importance of the accessory proteins in the activation of urease is clear, the exact mechanism of this activation process is still unknown, with two main hypotheses posited. One proposal invokes a "hand-off" mechanism in which cytosolic nickel binds to the UreE metallochaperone and passes to surface-exposed residues of UreG, then UreD, and finally into the nascent active site of *K. aerogenes* urease apoprotein, all within the urease:UreD:UreF:UreG complex (5, 9). Precedence for such a hand-off mechanism includes Cox17 and ScoI, which utilize thiol groups to pass Cu(I) into cytochrome *c* oxidase (42). The second hypothesis involves the initial delivery of nickel from UreE to UreG, followed by the use of a buried channel connecting the proposed nickel-binding site of UreG, through UreF and UreH, directly into the nascent active site of *H. pylori* urease (53). Examples of this strategy can be observed in the metal ion transfer tunnel into the ferritin core (7), Fe-Fe hydrogenase synthesis via a channel involving HydA (35) and membrane-bound uptake proteins for cations (6).

Here, the function of *Ka*UreD in urease activation is examined. The effects of targeted UreD side chain substitutions on the *in vivo* activation of urease, protein interactions with other urease components, and metal content of the purified enzyme are determined. This work provides further insights into how UreD functions in the activation of urease.

MATERIALS AND METHODS

UreD Homology Model Generation, Conservation Mapping, and Water Tunnel Prediction. To help select residues for substitution in *Ka*UreD, a homology model was prepared by using the Protein Homology/analogY Recognition Engine (Phyre2.0) server (27) and the crystal structure of *Hp*UreH from the UreH:UreF:UreG complex (PDB code 4HI0) as a template. A PSI-BLAST analysis (26) was performed for *Hp*UreD, sequences with more than 15% and less than 90% identity were identified, and the top 30 were selected along with *Ka*UreD. A multiple sequence alignment was prepared and the residue conservation scores were mapped onto the *Ka*UreD homology model using the ConSurf server (12). MOLE2.0 (45) was used to predict water tunnels within the *Ka*UreD homology model, and the effects of substituting residues along this tunnel were analyzed for steric clashes in Pymol (1) and by MOLE2.0 to determine if the water tunnels had been disrupted.

Plasmid Construction. To characterize the effects of point substitutions on the function of *Ka*UreD *in vivo*, three types of plasmids were constructed (i.e., pMF001L*, pKK17D*, and pKKD*G, where * indicates the mutant versions).

An EcoRI/HindIII fragment of pEC002 (9) containing *ureD* was inserted into similarly digested pUC8 to yield plasmid pMF001. This plasmid cannot be used to overproduce UreD directly because it was found to lack a critical upstream region needed for overexpression, so an

EcoRI/AgeI fragment of pKK17 (15) (containing *ureD* and a 197-bp 5' untranslated region) was substituted into similarly digested pMF001 to yield pMF001L. The accessory gene within pMF001L was mutated by polymerase chain reaction with overlapping oligonucleotides (Integrated DNA Technologies, Coralville, IA) containing the proper base-pair substitution(s) and amplified with *Pfu*Turbo® polymerase (Aligent Technologies). The resulting pMF001L* products were digested with *DpnI* and transformed into *E. coli* MAX Efficiency® DH5α cells (Life Technologies). Mutagenesis was confirmed by sequencing (Davis Sequencing, Davis, CA; Michigan State University Genomics Core, East Lansing, MI).

To study the effects of *ureD* mutations within the context of the intact urease gene cluster, the pMF001L* versions were digested and the desired *ureD*-containing fragments were isolated as described above. These fragments were ligated into similarly treated pKK17 to yield the analogous versions of plasmid pKK17D*. These plasmids were also sequenced to ensure the proper insertions were present.

To examine the effects of substitutions in UreD on protein:protein interactions, wild-type and variant EcoRI/AgeI *ureD* fragments from pMF001L* were ligated into the similarly digested and isolated backbone of pKKG (5). The resulting pKKD*G plasmids contain the *ureD* versions within the context of *ureDABCEFG*$_{\mathrm{Str}}$, where UreG has been modified with a *C*-terminal *Strep*-tag II (UreG$_{Str}$). The validities of the resulting plasmids were confirmed by sequencing. A summary of all plasmids used in these studies can be viewed in Table 3.1.

Table 3.1: Plasmids used in Chapter 3.

Plasmid used	Description	Source
pUC8	High-copy number, pBR322-derived vector conferring *Amp*^{R}	(51)
pKK17	Wild-type *K. aerogenes* urease cluster (*ureDABCEFG*) placed into pKK223-3	(15)
pKK17D*, -V37L, -Y42D, -E46A, -E46Q, -C48A, -H49A, -H54A, -I59Y, -D63A, -D63Q, -L65I, -L65W, -S85K, -K86A, -Y88V, -Y88F, -R89A, -W111Y, -T128E, -D142A, -R148M, -E153A, -E153Q, -R163A, -E165A, -D169A, -E176A, -E176Q, -T196K, -R211A, -R233A	EcoRI-AgeI *5'UTR-ureD* fragment from pMF001L* ligated into similarly digested pKK17	This study
pKKG	PstI-KpnI *ureG*$_{Str}$ fragment ligated into similarly digested pKK17 resulting in replacement of UreG with one containing a *C*-terminal *Strep*-tag II (*ureDABCEFG*$_{Str}$)	(5)
pKKD*G, -D63A, -D63Q. –S85K, -D142A, -E176A, -E176Q, -R211A	EcoRI-AgeI *5'UTR-ureD* fragment from pMF001L* ligated into similarly digested pKKG	This study
pEC002	pMAL-c2X derived vector for the overproduction of maltose binding protein fused at the *N*-terminus of UreD	(9)
pMF001	EcoRI-HindIII *ureD* fragment from pEC002 ligated into similarly digested pUC8	This study
pMF001L	EcoRI-AgeI *5'UTR-ureD* fragment from pKK17 ligated into similarly digested pMF001	This study

***In Vivo* Activation of Urease by Variant UreDs.** *E. coli* BL21(DE3) competent cells were transformed with pKK17D* or pKKD*G and plated on lysogeny broth (LB) agar plates supplemented with 300 µg/mL ampicillin. A single transformant colony was used to inoculate 2 mL of LB medium supplemented with 100 µg/mL ampicillin and cultured overnight. Aliquots (150 µl) of these overnight cultures were used to inoculate 15 mL of LB supplemented with 1 mM $NiCl_2$ and 100 µg/mL ampicillin in 50 mL flasks, which were shaken at 200 RPM at 37 °C until reaching an optical density at 600 nm (OD_{600}) of 0.5, induced with 0.1 mM isopropyl β-D-

1-thiogalactopyranoside (IPTG), and grown overnight at 37 °C. Urease apoprotein was prepared in a similar manner, but with the culture medium lacking supplemental nickel. Cells were harvested by centrifugation and resuspended in 2.5 mL of 100 mM HEPES, pH 7.8, per g of wet cell paste. Cells were lysed by sonication while placed in an ethanol ice bath using a Branson 450 sonifier with three 2-min cycles at 4 W output power and 50% duty cycle and 1 min of temperature recovery between cycles. Cell lysates were clarified by centrifugation at 100,000 *g* at 4 °C for one h. The soluble cell-free extracts were diluted 100-fold into 100 mM HEPES, pH 7.8, buffer for urease activity assays. Overproduction of urease subunits was confirmed by sodium dodecyl sulfate-polyacrylamide gel electrophoresis (SDS-PAGE).

Affinity Pull-Down Assays Using Soluble Cell-Free Extracts. To test if activation-deficient UreD variants exhibit impaired interactions with urease or the other accessory proteins, *E. coli* BL21(DE3) cells were transformed with pKKD*G constructs of interest. Cells were cultured, induced, and harvested as described above, and frozen at -80 °C until being further analyzed. Cells were thawed, resuspended in 1 mL of buffer W (50 mM NaH_2PO_4, pH 8.0, containing 300 mM NaCl and 1 mM ethylenediaminetetraacetic acid (EDTA)) supplemented with 0.1 mM phenylmethanesulfonylfluoride (PMSF), and lysed by sonication using 10 pulses at 1 W output power while placed on ice for five cycles with 15 s of recovery between cycles. Unbroken cells and debris were removed by centrifugation at 22,000 *g* at 4 °C for one h. Soluble cell-free extracts were loaded onto 2.5 mL of *Strep*-Tactin Superflow Plus resin (Qiagen) pre-equilibrated in buffer W and washed with 8 volumes of buffer W to remove unbound proteins. Proteins were eluted with 8 volumes of buffer W containing 2.5 mM desthiobiotin. The soluble cell-free extracts, wash fractions, and elution fractions were analyzed by SDS-PAGE.

Protein Purification. To determine the metal contents of urease produced by cultures containing functionally-deficient UreD, *E. coli* BL21(DE3) cells were transformed with pKKD*G constructs of interest. A single transformant colony was inoculated into 5 mL of LB supplemented with 100 μg/mL ampicillin and cultured overnight. For each UreD variant used, 1 L of LB supplemented with 1 mM $NiCl_2$ and 100 μg/mL of ampicillin was inoculated with 1 ml of overnight culture and grown until reaching an OD_{600} of ~0.6. These cultures were induced with 0.1 mM IPTG and grown overnight with shaking at 37 °C. Cells were harvested by centrifugation and resuspended in 2.5 volumes of buffer containing 50 mM Tris-base, pH 7.4, 1 mM EDTA, and 1 mM β-mercaptoethanol (TEB), and supplemented with 0.1 mM PMSF. Cells were lysed by sonication while immersed in an ethanol ice bath using a Branson 450 sonifier with three 2 min cycles at 4 W output power and 50% duty cycle including 1 min of temperature recovery between cycles. Soluble cell-free extracts were separated from unbroken cells and debris by centrifugation at 100,000 *g* for one h at 4 °C. Supernatants were diluted 1:1 in TEB buffer before being applied to a 90 mL Macro-Prep® DEAE Support (Bio-Rad) column pre-equilibrated in TEB buffer. The samples were washed with one volume of TEB buffer and eluted by using a 0 M to 1 M NaCl gradient in TEB buffer. Fractions containing urease were pooled, dialyzed into TEB buffer containing 25 mM NaCl, and concentrated to 1 mL by using an Amicon® Ultra-15 10K centrifugal filter (Millipore). Each concentrate was injected directly onto 100 mL columns containing either Superdex 200 (General Electric) or Sephacryl 300 HR (Sigma) resin pre-equilibrated in TEB buffer containing 25 mM NaCl. Proteins were eluted using the same buffer, and the fractions containing urease were pooled and concentrated to 2.5 mL. The pooled samples were analyzed for their purity by SDS-PAGE and assayed for urease specific activity.

Urease apoprotein was purified from cells containing the pKK17 plasmid as described previously (9).

Urease Activity Assays. Enzyme activity was measured by quantifying ammonia release from urea using methods described by Weatherburn (50)**.** The release of ammonia over time was monitored by the formation of indophenol on the basis of its absorption of light at 625 nm. One unit of urease activity is defined as the amount of enzyme required to hydrolyze 1 μmol of urea/min at 37 °C. The standard assay buffer was 50 mM of HEPES, pH 7.8, with 50 mM urea.

Protein Analyses. All SDS-PAGE analyses were performed using 15% running gels and 5% stacking gels prepared with 1.5 M Tris, pH 8.8, and 1 M Tris, pH 6.8, buffers, respectively. All gels were prepared using a 30% acrylamide:bis-acrylamide solution at 37.5:1 (Bio-Rad). All protein concentrations were determined with a commercially available protein assay kit and using bovine serum albumin as a standard (Bio-Rad). The metal contents of the purified urease pools were analyzed by inductively couple plasma-atomic emission spectroscopy (ICP-AES) (University of Georgia Chemical Analysis Laboratory).

RESULTS

Selecting Residues for Substitution in UreD. To investigate the function of UreD in the activation of *K. aerogenes* urease, a series of *ureD* mutants were examined for their effects on urease activity, metal content, and UreD:urease and UreD:UreF protein:protein interactions. Residues targeted for substitution were based, in part, on a multiple sequence alignment (31) of 32 homologous sequences that identified the conserved residues in the protein (Table 3.2). No metal-binding motifs were readily apparent within the alignment, nor were any metal-binding motifs identified for UreH within the UreH:UreF:UreG structure (19, 20).

Table 3.2: Multiple sequence alignment of UreD homologs used in Consurf conservation analysis. [a]

```
Nostoc sp. PCC 7120 UTEX 2576      -------GWHGKLNLVYAD-RSNSTQLIYNHQQAPLKVQRPFYPE-----
Nostoc sp. PCC 7107                -------AWHGKLNLIYAD-RQNSTQLIYNHHQAPLKVQRPFYPE-----
Nostoc sp.                         -------GWHGKLNLVYAD-RLGATELIYNHQQAPLKIQRPFYPE-----
Anabaena sp. 90                    ------QGWHGLLNLVYAN-RQDSTQLIYNHHQAPLKVQRPFYPE-----
Anabaena cylindrica                VNSPIDKNWHGRLNLVYAK-RQDSTQLIYNHHQAPFNIQRPFYPE-----
Nostoc punctiforme sp.             -------GWHGKLNLVYAD-RQGATQLIYNQQQAPLKVQRPFYPE-----
Microchaete sp. PCC 7126           -----TEGWHGQLNLVYAD-RHNSTQLIYNHHQAPLKVQRPFYPE-----
Chlorogloeopsis fritschii          ------QGWYGNLNLVYAR-TQGETQLIHSQSQAPLKVQRPFYPE-----
Scytonema hofmanni UTEX 2349       -------GWHGKLNLVYAD-RLGTTALIHNSHQAPLKVQRPFYPE-----
Fischerella sp. PCC 9339           --------WHGNLHLVYAD-RQNQTQLIFNQNQAPLKVQRPFYPE-----
Fischerella sp. PCC 9431           --------WYGNLDLVYAY-HQNQTQLIFNQNQAPLKVQRPFYPE-----
Fischerella sp. JSC-11             --------WHGNLHLVYAY-RQNQTQLIFNQNQAPLKVQRPFYPE-----
Fischerella sp. PCC 9605           -------GWHGKLNLVYAH-SQSGTQLIFNRNQAPLKVQRPFYPE-----
Scytonema hofmanni                 -------GWHGKLDLVYAQ-CQGKTTLIHNQNIAPLKVQRPFYPE-----
Mastigocladopsis repens            -----PTGWYGKLSLVYAH-RQNTTTLIHNQNQAPLKVQRPFYPE-----
Mastigocoleus testarum             --------WHGMLNLTYAS-RQGKTVIVEQQNQAPLKVQRPLYPEEQTDP
Calothrix sp. 336/3                -------SWHGKLHLTYGS-HGGKTQLVSSQNQAPLKVQRPFYPE-----
Rivularia sp.                      ----SSQSWHGKLNLVYNH-SQNKTALIQSRNQAPLKVQRPFYPE-----
Calothrix sp.                      -------SWHGKLDLLYAN-RQGITQLIHAHHQAPLKVQRPFYPE-----
Leptolyngbya boryana               ---LNPTDWHGILQLGFEY-RQGKTQLIRNQGQAPLKVQRPFYPE-----
Microcoleus sp.                    ----SSSGWHGSLQLVYAH-DHNGTQLTHAQVQAPLKVQRSFYPE-----
Coleofasciculus chthonoplastes     --------WQGSLELVYAN-DQGKTRLVRDRITSPLKVQRPFYPE-----
Synechocystis sp.                  --------WHGNLNLVYAQ-HQGKTQVIHSQMKAPLKVQRPFYPE-----
Chroococcidiopsis thermalis        -----PSTWHGNLDIVYAL-RNGKTQPISDRVQAPLKVQRPFYPE-----
Crinalium epipsammum               -----KSSWHGSLDLKFAC-RDGGSQVIKSQGKAPLKVQRPFYPE-----
Gloeocapsa sp. PCC 7428            -------SWHGSLNMVYTC-VDGATTVTHQQMQAPLKVQRPFYPE-----
Oscillatoria nigro-viridis         -----QTAWHGRLNLAYAN-RSGATQIIHNQMQAPLKVQRPFYPE-----
Oscillatoria acuminata PCC 6304    ------QGWHGSLELVYAQ-SGNATQMVSAKATAPLKIQRPFYPE-----
Arthrospira platenis sp.NIES-39    ----NPSEWHGILNLTYSQ-NHGITQVVDKYTTAPYKIQRPFYPP-----
Pseudomonas syringae               -----TPNWHAELELGYGR-FGDSTRPVQRRHKGPLRVQKHLYAE-----
Klebsiella aerogenes               -------GWQATLDLRFHQ-AGGKTVLASAQHVGPLTVQRPFYPE-----
Helicobacter pylori                ---MNTYAQESKLRLKTKIGADGRCVIEDNFFTPPFKLMAPFYPK-----
                                             . * :       .           *  :   :*.

Nostoc sp. PCC 7120 UTEX 2576      GEKVCHSVILHTAGGVVGGDRLSYNLHLQPNAQALITTAAAGKVYRSDG
Nostoc sp. PCC 7107                -GEKVCHSVILHTAGGVVGSDRLSSHFHLQPNTQALITTAAASKIYRSNG
Nostoc sp.                         -GERVCHSVILHTAGGVVGGDRLSTKIHLQPHTQAVITTAAAGKIYRSNG
Anabaena sp. 90                    -GQEICHSVILHTAGGIVGGDRLSSHIHLQPDTNALITTAAAGKIYRSNG
Anabaena cylindrica                -GQEVCHSVILHTAGGIVGGDRLSSDIHLEKDSQALITTAAAGKVYRSNG
Nostoc punctiforme sp.             -AEKVCHSVILHTAGGMVGGDRLSSNIHLQPQAQALITTAAASKIYRSNG
Microchaete sp. PCC 7126           -GEKVCHSIILHTAGGIVGGDRLSSKIHLQPDAQAVITTAAASKIYRSNG
Chlorogloeopsis fritschii          -GKNVCHSVILHTAGGIVGGDRLSCNFHLEPHAQALITTAAASKIYRTNG
Scytonema hofmanni UTEX 2349       -GQQVCHSIILHTAGGVVGGDRLSLNFHLQPNTQALITTAAASKIYRSNG
Fischerella sp. PCC 9339           -GQKVCHSVILHTAGGVVGGDRLSYDFHLQPHAQALITTATAGKIYRTNG
Fischerella sp. PCC 9431           -GQEVCHSVILHTGGGVVGGDRLSYDFHLQSDAQALITTATAGKIYRSNG
Fischerella sp. JSC-11             -GQEVCHSVILHTAGGVVGGDRLSYNFHLQPHAQALITTATAGKIYRSNG
Fischerella sp. PCC 9605           -GQEVCHSVILHTAGGVVGGDRLSYHLHLQPNAQALITTAAAGKIYRSNG
Scytonema hofmanni                 -GQEICHSVILHTAGGVVGGDRLSYKVHLQPKAQALITTAAASKIYRSNG
Mastigocladopsis repens            -GQQVCHSVILHTAGGIVGGDRLSCNFHLQPNAQALITTAAASKIYRSNG
Mastigocoleus testarum             EGQKICHSIILHTAGGVVGGDRLSCNFDLQPNSQALITTAAASKIYRSNG
Calothrix sp. 336/3                -GEAVCHSIILHTAGGVVGGDRLSTNIHLQPQSQVLLTTAAASKIYKSNG
Rivularia sp.                      -GQSVCHSVILHTAGGIVGGDRLSSDFHLQPDSKALITTAAANKIYRSNG
Calothrix sp.                      -GKAVCHSVILHTAGGVVGGDKLSCNFQLQPESQVLITTAAAGKIYRSNG
```

Table 3.2 (cont'd):

```
Leptolyngbya boryana                -GDEVCHSVIMHTAGGIVGGDRLTFDFHLASGSQALITTPAASKIYRTNG
Microcoleus sp.                     -GSAVCHSVVLHTAGGIVGGDRLSQTIHLSPHAHALITTAAASKIYGSKG
Coleofasciculus chthonoplastes      -GQGVCHTVVLHTAGGIVGGDRLSQTIHLQEDSQALITTAAASKIYRSNG
Synechocystis sp.                   -G-GVCHSVVLHTAGGIVGGDRNNLSFHLQPHSQSLITTATASKIYRSNG
Chroococcidiopsis thermalis         -G-DICHTAILHTAGGIVGGDCLSINLQLQPRSQALVTTTAASKIYRSNG
Crinalium epipsammum                -GREVCHSVILHTGGGVVGGDRLSLNFHLQPNTHALITSAAAGKVYRSNG
Gloeocapsa sp. PCC 7428             -GAEVCHSVILHTAGGVVGGDKLSLNFHLQQNAHTLITTAAASKIYRSNG
Oscillatoria nigro-viridis          -GKDVCHSVILHTAGGVVGGDRLSGHFHLQPNAKALITTAAAGKIYRSSG
Oscillatoria acuminata PCC 6304     -GEGVCHSVILHTAGGIVGGDSLGQSIHVQENAHALITTAAAAKIYRSTG
Arthrospira platenis sp.NIES-39     -GEEICHSVALHTAGGMVGGDRLSQNLHLQADTKVLLTTAAASRVYRSTG
Pseudomonas syringae                -GPQVCQHIIVHPPGGIAGGDRLDISAHVGPDAWAQLTSPGAAKWYRAAG
Klebsiella aerogenes                --EETCHLYLLHPPGGIVGGDELTISAHLAPGCHTLITMPGASKFYRSSG
Helicobacter pylori                 --DDLAEIMLLAVSPGMMRGDAQDVQLNIGPNCKLRITSQSFEKIHNTED
                                         ..   :    *:  .*      .:       :*     : : : .

Nostoc sp. PCC 7120 UTEX 2576       --------LQARQTIEIKIDAGACLEWLPQETILFNGAIYRQDLRVELAT
Nostoc sp. PCC 7107                 --------LQARQTIDIQIDAGACLEFLPQETILFNGADYRQDLRVELAT
Nostoc sp.                          --------LQARQTIDIQIDAGACLEWLPQETILFNGAIYRQDLRVELAT
Anabaena sp. 90                     --------LPARQTVNIQVDSHACLEYLPQETILFNGGIYRQDLRVELAT
Anabaena cylindrica                 --------LPAKQTVNIQIGANACLEYLPQETILFNGAVYRQDLKVKLDT
Nostoc punctiforme sp.              --------LQARQTIQMQVDPGACLEWLPQETILFNDAIYRQDLRVELAT
Microchaete sp. PCC 7126            --------LPATQTINLKIDTGACLEWLPQETILFNDGIYRQDLRVELAT
Chlorogloeopsis fritschii           --------LRARQTINIQIDANACLEWLPQETIVFNSALYRQDLRVELAT
Scytonema hofmanni UTEX 2349        --------TQAKQSINIQVDAGACLEWFPQETIVFNGAIYRQDLRVELAT
Fischerella sp. PCC 9339            --------MTAKQMIEIKVDDGACLEWLPQETIVFDGALYRQDINVKLAT
Fischerella sp. PCC 9431            --------MIAKQVIEIKVDDGACLEWLPQETIVFDGALYQQDLRVNLAT
Fischerella sp. JSC-11              --------TIAKQTIEIKVDDHAYLEWLPQETIVFDGALYRQENIVKLAT
Fischerella sp. PCC 9605            --------TTARQTIEIKVDAGACLEWIPQETIVFNSALYRQDLRVELTT
Scytonema hofmanni                  --------AQARQNIDIQVDAGASLEWLPQETIVFNGAIYRQDLRVELAT
Mastigocladopsis repens             --------TQAQQNIEIRVDSGACLELLPQETIVFNGAIYRQDLRVELAT
Mastigocoleus testarum              --------SQARQKIEINVDERACLEWLPQETIVFNAADYRQDLRVDLAN
Calothrix sp. 336/3                 --------LQARQDVTIHIDSHACLEYLPQETIVFNSANYRQDVRIHLAV
Rivularia sp.                       --------LQARQNIDIKIDKNACLEWLPQETIVFSGASFRQDIKIELAD
Calothrix sp.                       --------RQATQNINIEVSTGATLEWLPQETIVFDGAIYRQDTRINLAE
Leptolyngbya boryana                --------REAHQVIRVDVAEGACLEWLPLDSIVFNQAIYRQTMQINLAQ
Microcoleus sp.                     KSRACPQGQPAKQTIQIQIDQAACLEWLPQETIVFNGAIYQQDLRVELAP
Coleofasciculus chthonoplastes      --------QRANQRIHIHVEAGACLEWLPQETIVFNGADYQQQMTVELAP
Synechocystis sp.                   --------LLAKQNIQMQVDTDACLEWLPQETIVFDGAIYRQDLQVELAP
Chroococcidiopsis thermalis         --------LQARQIVEIQIDEGACLEWLPQETIVFNGANYRQDLRVELAP
Crinalium epipsammum                --------LEARQTVEMRVEAGACLEWLPQENIIFNDANYRQDLRVELAT
Gloeocapsa sp. PCC 7428             --------WEARQNIQVQVDSNACLEWFPQETIVFNGAIYRQDLRVELAP
Oscillatoria nigro-viridis          --------LESQQNIDIQLDTGANLEWLPQETIVFDGAIYRQNLRVELAP
Oscillatoria acuminata PCC 6304     --------EVARQSIKINVDSGAICEWLPQESIIFNGAIYRQDLRIELAP
Arthrospira platenis sp.NIES-39     --------KTASQNVKIKLEKGAYLEYLPRETIIFNGAIYRQDLRVELAP
Pseudomonas syringae                ---------PAYQQLDLTVEAGATLEWLPQETIVFSAAQAELTTRIELQG
Klebsiella aerogenes                --------AQALVRQQLTLAPQATLEWLPQDAIFFPGANARLFTTFHLCA
Helicobacter pylori                 G--------FASRDMHIVVGENAFLDFAPFPLIPFENAHFKGNTTISLRS
                                             :     : :   *  :: *   * *  .  .    . *

Nostoc sp. PCC 7120 UTEX 2576       GANFLGWEITRFGRSARGEKFYQGEWRSHTEIWQQGVPLWIDRQWLPGND
Nostoc sp. PCC 7107                 GACFLGWEITRCGRSARGEKFLEGKWRSHTEIWQQGVPLWIDRQFLPGNT
Nostoc sp.                          GANFIGWEITRFGRSARGEKFYQGEWRSHTEIWQEGVPLWIDRQYLPGSE
Anabaena sp. 90                     DASYLAWEITRFGRSARGEKFVQGEMRSHTEIWQNGIPLWIDRQIVPGSE
Anabaena cylindrica                 NSSFIGWEITRLGRSARGEKFLEGEMRSHTEIWQNGIPQWIDRQILPGSE
Nostoc punctiforme sp.              GASWLGWEITRFGRSARGEKFLQGEWRSHTEIWQQSVPLWIDRQCLRGSE
Microchaete sp. PCC 7126            GASFLGWEITRFGRTARGEKFYSGEWRSHTEIWQHNIPLWIDRQWLPGNQ
Chlorogloeopsis fritschii           GASYLGWEITRFGRTARGEKFVQGEWRSHTEIWQQGKPLWIDRQWLPGSD
Scytonema hofmanni UTEX 2349        KASYLGWEITRFGRSARGEKFVQGEWRNHTEIWQQGKPLWIDRQWLPGSE
Fischerella sp. PCC 9339            TASYIGWEITRFGRSARGEKFLQGEWRSHTEIWQQDKPLWIDRQWLPGSE
Fischerella sp. PCC 9431            KANYIGWEITRFGRSARGEKFLQGEWRSHTEIWQQNKPLWIDRQWLPASE
Fischerella sp. JSC-11              NSHYLGWEITRFGRSARGEKFLQGEWRSHTEIWQQGKPLWIDRQWLPGRE
```

Table 3.2 (cont'd):

```
Fischerella sp. PCC 9605          GASYLSWEITRFGRSARGEKFLQGEWRSNTEIWQQGKPLWIDRQWVPGSE
Scytonema hofmanni                GANWIGWEITRFGRSARGEKFCLGEWRSHTEVWQMGVPLWIDRQWLPGSE
Mastigocladopsis repens           KASWIGWEITRFGRSARGEKFLQGEWRSHTEIWQQGVPLWIDRQLLPGSE
Mastigocoleus testarum            NASFLGWEINRFGRTARGEKFVQGNWRSHTEIYQEGIPLWIDRQWLPGSE
Calothrix sp. 336/3               DASFLGWEITRFGRTARNEQFIQGEWRNYTEIWRDNQPLWIDRQYLPGDM
Rivularia sp.                     DANFIGWEITRFGRTARQEKFLTGEWRSNTEIWQNNKPLWIDRQYLPGSE
Calothrix sp.                     NANFIGWEITRFGRSARGEKFLHGNWKSNTEVWQQGKPLWVDRQWLPGSE
Leptolyngbya boryana              GANWLGWEITRFGRSARGEKFVEGNWRSRTEVWQAGKPIWIDRQWMPGSE
Microcoleus sp.                   GASWLGWEITRFGRSARGERFLQGEWRSHTEVWQQGRPLWIDRQWLPGEE
Coleofasciculus chthonoplastes    GASWLAWEITRFGRTARKERFLQGDWRSHTEIWQQGHPLWIDRQWLPGGE
Synechocystis sp.                 GAKWLGWEITRFGRTAKGERFLHGDWKSHTEVWQQGLPLWIDRQWLPAGE
Chroococcidiopsis thermalis       GASWLGWEITRFGRSARGERFLQGEWRSYTEVWQQGQPLWIDRQWLPGEE
Crinalium epipsammum              DATWMGWEITRLGRTARGEQFLQGNWRSHTEIWRQGDPLWIDRQWLPGGE
Gloeocapsa sp. PCC 7428           GATWTGWEITRFGRSARGEKFLQGNWRSHTEVWQQQRPLWIDRQQLRPDV
Oscillatoria nigro-viridis        TARILLWEITRFGRSARGENFLSGEWRSHTEVWQENSPLWIDRQLLKGGE
Oscillatoria acuminata PCC 6304   DARFLLWEINRFGRSARGETFVQGEWRSQTEIWQQGRPLWIDRQHLQGSE
Arthrospira platenis sp.NIES-39   EATWLGWEITRFGRSARGENFGQGEWRSHTEIWQNEKPLWIDRQWLPGGE
Pseudomonas syringae              DAKLMYWDVVALGRPASGERFTSGHFQSHVDIRRDGRLLWHERQRIIGGD
Klebsiella aerogenes              SSRLLAWDLLCLGRPVIGETFSHGTLSNRLEVWVDNEPLLVERLHLQEGE
Helicobacter pylori               SSQLLYSEIIVAGRVARNELFKFNRLHTKISILQDEKPIYYDNTILDPKT
                                   :     ::   ** .  * *  .   .  .:         :.  :

Nostoc sp. PCC 7120 UTEX 2576     AVFHSPHGLAGQPIVGSLVWLGSPISTEIIEKARNLGNTQGE--------
Nostoc sp. PCC 7107               DIFHSPHGLFGQPIVGSLLWLGHPVSTEIIEQVRSL-FTKHL--------
Nostoc sp.                        EVFHSPHGLSGQPIAGNFIYLGSPVSKETIEKARSIFTPHAL--------
Anabaena sp. 90                   EVFHSPHGLRDNPVVGSFVGVGFPISPEIINQARSLIIQNSD--------
Anabaena cylindrica               EVFHSPHGLAGYPVVGSLVWVGSSVSREIIEKARSLVTQNNL--------
Nostoc punctiforme sp.            DIFHSPHGLAGKPIVGSLVWVGGAVSAEIVEKTRSLWNGEGE--------
Microchaete sp. PCC 7126          DVFHSPHGLSGKPIVGTFVWVGDVVSAEIVETARNLWNGEGE--------
Chlorogloeopsis fritschii         KIFHSPHGLNGQAIAGSLVWVQGAVSQDMIEKARDLWHGEGE--------
Scytonema hofmanni UTEX 2349      EVFHSPHGLAGQPITGTLVWVGSSVSAEIVEKARLKWNGAGE--------
Fischerella sp. PCC 9339          EVFHSPHGLAGQPIVGSLVYIGQKISPELVHQARNLWKPTLT--------
Fischerella sp. PCC 9431          EVFHSPHGLAGQPIVGSLVYIGQEISPELVNKARNLGKPTLS--------
Fischerella sp. JSC-11            EVFHSFHGLAGQPIVGSLVYIGREISPEIVEKARNLWQLPIT--------
Fischerella sp. PCC 9605          EIFYSPHGLAGQPVVGSLVWVGSAVSVEIIEKARNIWQPIPPSPSLPL--
Scytonema hofmanni                DVFHSPHGLAGQPVTGSLVYIGQEVSQELVHKARTLFLSPTPHSLLP---
Mastigocladopsis repens           EVFHSPHGLAGQPLVGSLVYVGQEVSPELVEKVRSLWNG-----------
Mastigocoleus testarum            EIFYSPNGLAGQAVIGSLIFVGKTISKDIVEQVRSLWKSNPHMTLSRHAA
Calothrix sp. 336/3               AVFHSPHGLNSQAIAGSFIYLGKQISPQLITQIRQMWGEN----------
Rivularia sp.                     EVFHSPHALAGKPIVGTLIYIGKPVSPEIVQKIRTLFIPPS---------
Calothrix sp.                     EIFYSPHALNGQPVVGTFIYIGSTVSPEIIEKASSYTQHSVLS-------
Leptolyngbya boryana              ENFASPHGLAGCPVVGSFAWVGQVVTPELVEKARELWAGSSG--------
Microcoleus sp.                   QVLDSPHGLAGKPIVASLAWVGQAVSPEMIEKARLIWA---TQER-----
Coleofasciculus chthonoplastes    AVLDSPHGLAGEPIVGTLIWMGPPVSSEIIDNARSLWT---ADQR-----
Synechocystis sp.                 KIIDSPHGLAGLPIVGSLAWIGQPVEPEIVEKARVLFP---NNS------
Chroococcidiopsis thermalis       AILNSPHGLAGHSIVASLTWIGCEVSPELVTKCRDVTCNVSTTIP-----
Crinalium epipsammum              NIINSPHDLAGYPVIASFAFVGKAVSKDLIEKARNCWQAGEY--------
Gloeocapsa sp. PCC 7428           KVIDSPHGLAGKSIIGSFVWIGQPVSADVVEKVR--MLSTVD--------
Oscillatoria nigro-viridis        KMLESPHGLAGKPVVATLAWVGEPVTAEFVEKVRDLPSEATIYPG-----
Oscillatoria acuminata PCC 6304   SAVSSNSALAGFPIVATLAWIGDPVTPELVQEARSLWEGRSSSS------
Arthrospira platenis sp.NIES-39   TILESPHGLGGWPVVATLTWVGEPVSKETLNHVRMLWGEHQS--------
Pseudomonas syringae              GLLDSPIGLDGKTVFATLLITG-EVDSELLEACRSLSSPVRG--------
Klebsiella aerogenes              -----LSSIAERPWVG--TLLCYPATDALLDGVRDALAPLGLY-------
Helicobacter pylori               TDLNNMCMFDGYTHYLNLVLVNCPIELSGVRECIEESEGVDG--------
                                         :   .               :

Nostoc sp. PCC 7120 UTEX 2576     -----------AGVTSLEN-GFLCRYRGASTSEVRNWFTSVWQLLRGEFF
Nostoc sp. PCC 7107               -----------TGVTQLEH-GLLCRYRGASTSEVRNWFTAVWQILRTSFL
Nostoc sp.                        -----------IGVTRLEN-GFLCRYRGASTSEVRHWFTSVWQMLRVDYF
Anabaena sp. 90                   -----------AGVTRLQH-GFLCRYRGNSTSQVRSWFTNIWQMLRVSCL
Anabaena cylindrica               -----------TGVSRLQN-GFLCRYRGNSTSEVRNWFTNVWQILRVSLL
```

Table 3.2 (cont'd):

```
Nostoc punctiforme sp.              -----------VGASRLQH-GLLCRYRGSSTSEVRNWFIDVWQLLRVSFL
Microchaete sp. PCC 7126            -----------TGVTLLTH-GFLCRYRGDSTSEVRNWFMAVWQMLRISVW
Chlorogloeopsis fritschii           -----------VGVTRLEH-GFLCRYRGSSTAEVRNWFISVWQLLRVSFL
Scytonema hofmanni UTEX 2349        -----------AGVTRLEN-GFLCRYRGSSTSEVRNWFIDVWQLLRMSFL
Fischerella sp. PCC 9339            --------HSQIGVTRLEH-GLLCRYRGYSTTEVRNWFIGVWQLLRIFFL
Fischerella sp. PCC 9431            --------HSQIGVTRLEH-GLLCRYRGSSTAEVRNWFIGVWQLLRMSFL
Fischerella sp. JSC-11              --------HPQIGVTRLEH-GLLCRYRGSSTAEVRNWFIGVWQLLRMSFL
Fischerella sp. PCC 9605            ------PLSSQIGVTRLEH-GFLCRYRGSSTAEVRHWFIGVWQLLRMSFL
Scytonema hofmanni                  --------TPSVGVTRLSC-GLLCRYRGSGTTEVRNWFTSAWQLLRQSVL
Mastigocladopsis repens             --------KGEAGVTRLSC-GLLCRYRGSTTSEVRNWFTAVWQLLRQSFL
Mastigocoleus testarum              LTPIPNSKSPNQGVTRLNN-GFLCRYRGNSTAEVRNWFINVWLLLRTSFL
Calothrix sp. 336/3                 ------SPS-AVGVTALEH-GFLCRYRGNSTSEVRNWFISVWQLLRQSIG
Rivularia sp.                       -PPLPIPPS-SQGVTRIEN-GLLCRYRGDSTAKVRNWFISVWQLLRISFL
Calothrix sp.                       -------TQYSFGVTRLEH-GFLCRYRGSSTSEVRNWFTAAWQLLRQSLL
Leptolyngbya boryana                ----------EIGVTRLSI-GLLCRYRGHSSSEARRWFLAVWQLIRVSYF
Microcoleus sp.                     --------QGEAGVTQLMS-GLLCRYRGSSTSEVRNWFTEVWQLLRLSFL
Coleofasciculus chthonoplastes      --------QGEAGVTQTQAQGLLCRYRGSSTTEVRNWFTQVWQCLRLTYL
Synechocystis sp.                   --------SSQGGVTRLPM-GLLCRYRGSSSTEVRNWFTEIWQLLRSPYL
Chroococcidiopsis thermalis         --------ITNYGVTRLPH-GLLCRYRGSSSIEVRNWFTSVWQ-------
Crinalium epipsammum                --------QGESGVTTLLE-GMLCRYRGYSTLEARNWFIRVWELLRLAYL
Gloeocapsa sp. PCC 7428             --------QGETGVTRLTT-GLLCRYRGDSTTEVRQWFTEVWHLLRLSSL
Oscillatoria nigro-viridis          --------NSTVGVTRIPN-GLLCRYRGTSTTAARDWFVNIWQLLRLSFS
Oscillatoria acuminata PCC 6304     --------EGEAGVTRLTH-GLLCRYRGSSTPEVRNWFSEVWQLLRLSFI
Arthrospira platenis sp.NIES-39     --------EGEAGATQLLS-GLLCRYRGPSSQEAIAWFTQIWQLLRPNLS
Pseudomonas syringae                ------------DLTQLPG-LLVARCLADEALHARAWLIELWKLLRPAVL
Klebsiella aerogenes                -----------AGASLTDR-LLTVRFLSDDNLICQRVMRDVWQFLRPHLT
Helicobacter pylori                 ------------AVSETASSHLCVKALAKGSEPLLHLREKIARLVTQTTT
                                                    :      :  :  .

Nostoc sp. PCC 7120 UTEX 2576       SR-
Nostoc sp. PCC 7107                 SR-
Nostoc sp.                          KR-
Anabaena sp. 90                     NR-
Anabaena cylindrica                 NR-
Nostoc punctiforme sp.              NR-
Microchaete sp. PCC 7126            KR-
Chlorogloeopsis fritschii           SRV
Scytonema hofmanni UTEX 2349        NR-
Fischerella sp. PCC 9339            SR-
Fischerella sp. PCC 9431            SR-
Fischerella sp. JSC-11              NR-
Fischerella sp. PCC 9605            NR-
Scytonema hofmanni                  TR-
Mastigocladopsis repens             AR-
Mastigocoleus testarum              SR-
Calothrix sp. 336/3                 NR-
Rivularia sp.                       NR-
Calothrix sp.                       ER-
Leptolyngbya boryana                QR-
Microcoleus sp.                     GR-
Coleofasciculus chthonoplastes      GR-
Synechocystis sp.                   NR-
Chroococcidiopsis thermalis         ---
Crinalium epipsammum                GK-
Gloeocapsa sp.PCC 7428              GK-
Oscillatoria nigro-viridis          QR-
Oscillatoria acuminata PCC 6304     GR-
Arthrospira platenis sp.NIES-39     GK-
Pseudomonas syringae                GR-
Klebsiella aerogenes                GK-
Helicobacter pylori                 QKV
```

Table 3.2 (cont'd):

[a]The *K. aerogenes* UreD sequence shown does not include seven amino-terminal residues (MLPPLKK). Residues substituted by mutagenesis experiments are highlighted in yellow. The asterisk (*) symbols indicate positions which have a single, fully conserved residue, (:) indicates conservation between groups of strongly similar properties and (.) indicates weakly similar properties.

To specifically guide substitution of surface residues that may facilitate protein:protein interactions or participate in a hand-off mechanism during nickel transfer, a UreD homology model was prepared using the Phyre2.0 server with the pdb coordinates of UreH extracted from the UreH:UreF:UreG crystal structure (20) serving as the template (Figure 3.1A). Alignment of this homology model with UreH using PyMol (1) resulted in a C_α root mean square deviation of 0.469 Å. The extent of conservation derived from the sequence alignment was mapped onto the homology model by using the Consurf server (12), revealing a region of highly conserved, surface exposed residues on the face opposite to that of the UreF binding site (Figure 3.1C) (20). This region might reasonably function as the UreD:urease binding interface. Conserved surface residues predicted to lie in this region of the protein (Tyr42, Glu46, Cys48, His49, His54, Asp63, Lys86, Tyr88, Arg89, Arg148, and Glu153) were substituted. In addition, a few surface residues on the reverse face or near the UreF interface (Arg163, Glu165, Asp169, Glu176, Thr196, Arg211, and Arg233) were chosen for substitution. Arg211 and Arg233 are predicted to form polar contacts with UreF based on comparison to their homologous residues in the *Hp*UreH:UreF:UreG crystal structure (20).

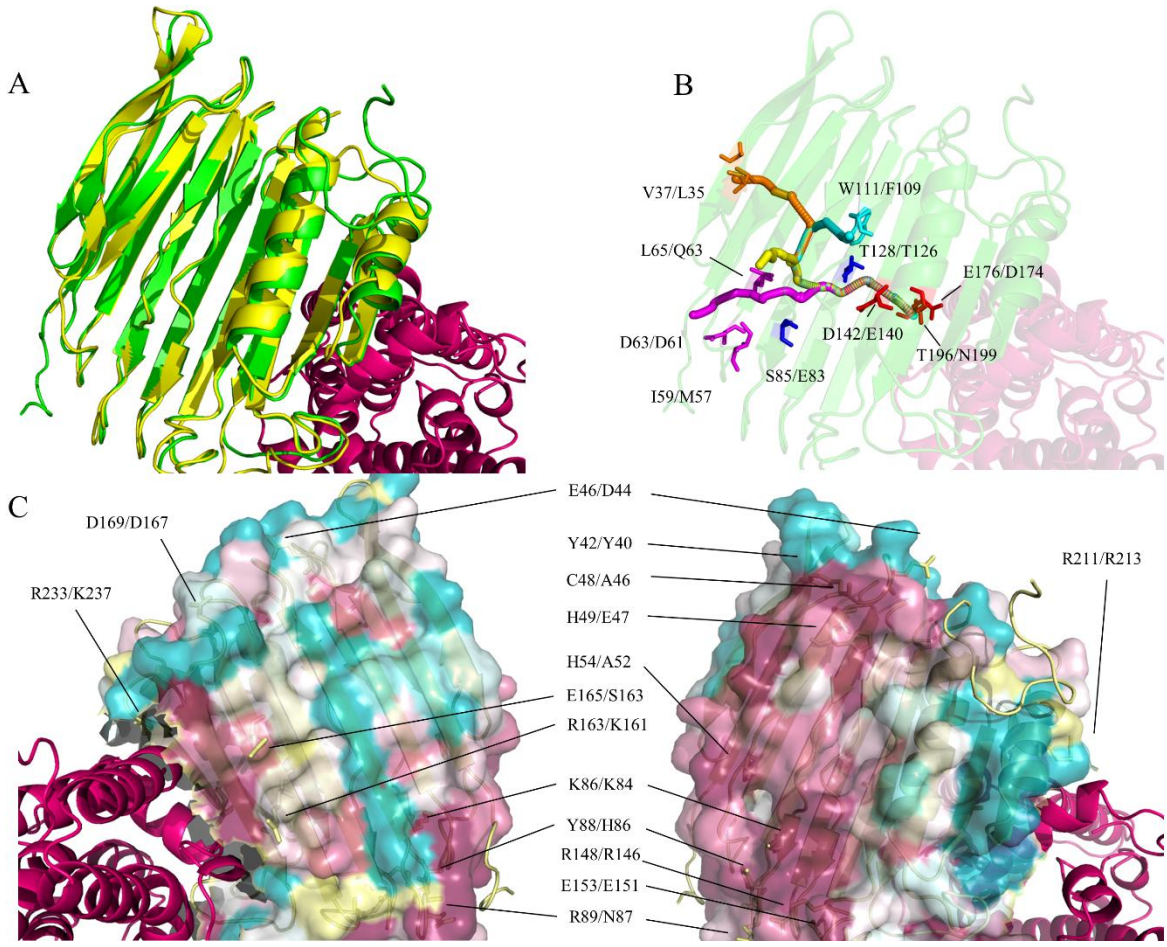

Figure 3.1: Homology-model guided mutagenesis of *K. aerogenes* UreD. (A) Phyre 2.0 homology model of *Ka*UreD (green) aligned to *Hp*UreH (yellow) from the *Hp*UreH:UreF:UreG crystal structure. *Hp*UreF (magenta) is depicted to define the *Hp*UreH:UreF interaction site. (B) Water tunnels predicted for the *Ka*UreD homology model by MOLE2.0. The color of residues corresponds to the associated tunnel exit (tunnel 1 = magenta, 2 = yellow, 3 = orange, and 4 = teal). Blue residues are positioned at the branch point shared by all tunnels, while red residues are located at the entrance point of the tunnel. (C) Two views of the *Ka*UreD homology model colored by conservation score as assigned using the Consurf server and depicted in a surface representation. Dark blue, white, and dark magenta denote low, average, and high conservation. Left image is a 180° y-axis rotation of the right image. Surface residues and buried residues not associated with predicted water tunnels are labeled. All residues listed were selected for mutagenesis and are noted with *K. aerogenes/H. pylori* numbering.

An additional group of residues selected for substitution were predicted to be at least partially buried in the protein and may be important for urease activation if the tunnel hypothesis is correct. Channels within the *H. pylori* UreH:UreF:UreG complex were previously predicted using CAVER 3.0 (13, 20); similar channels were identified on the same structure using

MOLE2.0 (not illustrated), an alternative software program that scans static structures for the presence of water tunnels. When this program was applied to the *K. aerogenes* UreD homology model, analogous tunnels were predicted, initiating near Glu176 at the UreF interface and exiting through any of four pathways (Figure 3.1B). The origin of these tunnels at the UreD:UreF interface is unchanged with the *H. pylori* protein and similarities exist between tunnel 1 of the UreD homology model and the exit tunnel predicted by CAVER 3.0 analysis of UreH:UreF:UreG. However, the three novel exit tunnels in the UreD homology model (tunnels 2, 3 and 4 in Figure 3.1B) were not predicted by either CAVER 3.0 or MOLE2.0 analysis of the UreH:UreF:UreG structure. To test for the importance of these channels in urease activation, selected non-surface (internal) residues were changed. For example, Glu176 was substituted with similarly sized and smaller residues, in both cases lacking a negative charge. Additionally, several substitutions were designed to place bulky (Phe, Tyr, or Trp) or long (Lys or Glu) residues at positions within or at the temini of the tunnels (e.g. Val37, Asp63, Leu61, Leu65, Ser85, Trp111, Thr128, and Thr196). For each alteration, the substitute residue was placed into the UreD homology model using Pymol and analyzed to ensure most rotomers did not have steric clashes. Models containing potential tunnel-blocking changes were analyzed with MOLE2.0 to assess whether the predicted blocking substitutions exhibited the desired effect of eliminating the tunnel. Variants which blocked the water tunnels *in silico* were selected for experimental study. The positions of residues selected for study and the corresponding *H. pylori* residue numbers are illustrated in Figure 3.1B and C. The set of substitutions, primers utilized, rationale for the mutations, and conservation score of the residues are listed in Table 3.3.

Table 3.3: Variant forms of *Ka*UreD, primers utilized, rationale for the changes, and conservation scores for the residues.[a]

UreD substitution	Primer used (5' → 3')	Rationale	Conservation Score[b]
V37L	GGCCCGCTGACC***CTC***CAGCGCCCGTTT	Block tunnel 3	8
Y42D	CTGACCGTCCAGCGCCCGTTT***GAT***CCGGAAGAAGAG	Alter surface	9
E46A	CAGCGCCCGTTTTACCCGGAAGAA***GCA***ACCTGTCACCTC	Alter surface	1
E46Q	CAGCGCCCGTTTTACCCGGAAGAA***CAA***ACCTGTCACCTC	Alter surface	1
C48A	CGGAAGAAGAGACC***GCT***CACCTCTATCTGC	Alter surface	8
H49A	GAAGAAGAGACCTGT***GCC***CTCTATCTGCTTC	Alter surface	9
H54A	CACCTCTATCTGCTT***GCA***CCGCCCGGCGGCATC	Alter surface	9
I59Y	CCGCCCGGCGGC***TAC***GTCGGCGGTGAT	Block tunnel	5
D63A	CATCGTCGGCGGT***GCA***GAGCTGACAATTAG	Disrupt tunnel 1 exit	9
D63Q	GGCGGCATCGTCGGCGGT***CAA***GAGCTGACAATT	Disrupt tunnel 1 exit	9
L65I	GGCGGTGATGAG***ATA***ACAATTAGCGCG	Block tunnel 1	8
L65W	GGCGGTGATGAG***TGG***ACAATTAGCGCG	Block tunnel 1	8
S85K	ATGCCTGGCGCC***AAA***AAGTTTTACCGC	Block shared cavity	5
K86A	GCCTGGCGCCAGC***GCG***TTTACCGCAGCAGC	Alter surface	9
Y88V	GGCGCCAGCAAGTTT***GTC***CGCAGCAGCGGCG	Alter surface	9
Y88F	GGCGCCAGCAAGTTT***TTC***CGCAGCAGCGGCG	Alter surface	9
R89A	GGCGCCAGCAAGTTTTAC***GCC***AGCAGCGGC	Alter surface	8
W111Y	GCGACCCTGGAG***TAT***CTCCCGCAGGAT	Block tunnel 4 exit	3
T128E	GCCCGGCTGTTC***GAA***ACCTTTCATCTT	Block shared cavity	4
D142A	CTGCTGGCCTGG***GCA***CTGCTCTGCCTTG	Disrupt shared cavity	9
R148M	CTGCTCTGCCTTGGC***ATG***CCGGTGATTGGCG	Alter surface	9
E153A	CCGGTGATTGGC***GCA***ACCTTCAGCCACGGC	Alter surface	9
E153Q	CCGGTGATTGGC***CAA***ACCTTCAGCCACGGC	Alter surface	9
R163A	ACCCTCAGCAAC***GCC***CTGGAGGTATGGGTG	Alter surface	6
E165A	CCTCAGCAACCGGCTG***GCG***GTATGGGTGGAC	Alter surface	8
D169A	CCGCTGGAGGTATGGGTG***GCC***AATGAGCCGCTGC	Alter surface	3
E176A	GCTGCTGGTC***GCA***CGCCTGCACCTG	Disrupt tunnel entrance	9
E176Q	CCGCTGCTGGTC***CAG***CGCCTGCACCTG	Disrupt tunnel entrance	9
T196K	CCCTGGGTCGGC***AAA***TTGCTGTGCTAT	Block tunnel entrance	4
R211A	CTCGACGGGGTG***GCC***GACGCGCTGGCG	Alter surface	8
R233A	CCGCCTGCTGACGGTG***GCT***TTCCTCAGTGAC	Alter surface	9

[a]Reverse complements of the primers listed were also used. See Figure 3.1C for an illustration of residue conservation. Bases altered from the wild-type sequence are noted in underlined bold italic font.

[b]Conservation scores are displayed on a scale from 1 to 9, with 1 denoting low and 9 denoting high conservation.

Effects of UreD Variants on the *In Vivo* Activation of Urease. To determine whether the *ureD* mutations affected *in vivo* urease activation, cells containing pKK17D* were cultured in LB in the absence or presence of 1 mM Ni^{2+}. SDS-PAGE was used to confirm similar levels of urease protein were produced in all cultures (data not shown). Substitutions of surface-exposed residues which map either to the highly conserved face of the UreD homology model or to the putative UreD:UreF interfacial site did not appreciably alter the activation of urease.

Substitutions involving four buried or partially buried residues (Glu63, Ser85, Glu142, Asp176) were shown to lead to greatly reduced (< 30%) urease specific activities relative to that of cells containing wild-type UreD when assayed using soluble cell-free extracts from these cultures. These residues were predicted to surround a 34.6 Å water tunnel (tunnel 1) within UreD. *In vivo* activation of urease using E176A or E176Q variants of UreD resulted in activities that were 27% and 21% of those activated with wild-type UreD. *Ka*UreD Glu176 corresponds to Asp174 in the *H. pylori* protein, where it maps to the interfacial site between UreH and UreF but is not involved in direct bonding to UreF. The D142A variant of UreD led to urease activity that is 24% of that obtained with the wild-type protein. This residue (corresponding to Glu140 in UreH) is predicted to be buried, forming backbone-mediated contacts with the side-chain of Thr196 and a hydrogen bond between the carboxylate oxygen and the backbone carbonyl oxygen of Leu143, and contributes to the β-sheet tertiary structure. Since β-sheet formation and stability is dominated by backbone hydrogen bonding, loss of the polar interaction is unlikely to severely affect the overall structural stability of UreD. Ser85 is positioned within UreD, with its side chain facing the shared branch-point for the water tunnels. The S85K variant, selected to avoid steric clashes predicted by modeling for bulky residues, yielded cell-free extract urease activities of 13% relative to the sample prepared from cells producing wild-type UreD. Asp63 resides on the face of UreD lying opposite the likely UreF interface and is positioned at the exit point of the 34.6 Å tunnel. Changing this residue to Ala or Gln resulted in cell-free extracts with urease specific activities that were 4% and 9%, respectively, of that obtained from samples with wild-type protein. Somewhat surprisingly, T196K UreD, containing a substitution designed to block the entrance point of the tunnel at the UreD:UreF interface, had only a mild effect on urease activation (76% of wild-type activation). These findings are illustrated in Figure 3.2.

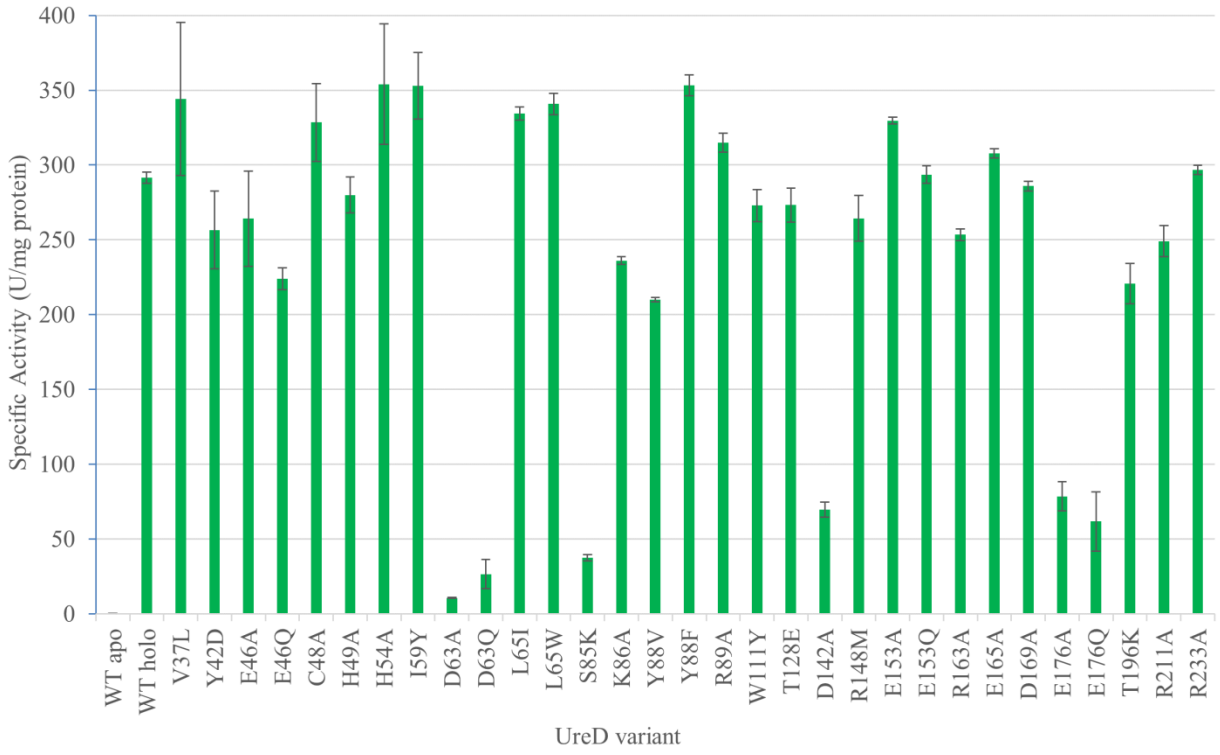

Figure 3.2: Urease activity of cell-free extracts from cells containing *Ka*UreD variants. *E. coli* BL21(DE3) cells were transformed with plasmid pKK17D* (encoding *ureD*ABCEFG*), grown in LB containing 1 mM $NiCl_2$ (except for the sample producing urease apoprotein, which was not supplemented with the metal), and soluble cell-free extracts were assayed for urease activity. Error bars represent triplicate analysis of single experimental samples.

Pull-Down Assays. To identify whether urease:UreD or UreD:UreF protein:protein interactions were disrupted for the UreD variants deficient in urease activation, the urease:UreD:UreF:$UreG_{Str}$ complexes were examined from *E. coli* cells containing pKKGD*. These constructs allowed for *Strep*-Tactin pull-downs by making use of UreG containing a *C*-terminal *Strep*-II tag (5). Previous studies had shown the intact complex can be isolated from such cells cultured in LB medium that lacked additional Ni^{2+}. The five *ureD* constructs found to be deficient in urease activation were inserted into pKKG, with the genes encoding wild-type and R211A UreD (providing 90% activity relative to wild-type) used as controls. In all cases, the soluble cell-free extracts produced similar levels of urease (Figure 3.3, lanes labeled I), and the

UreG$_{Str}$-containing fractions eluted from the *Strep*-Tactin resin (Figure 3.3, lanes labeled E) contained the urease subunits and the UreD, UreF and UreG accessory proteins. This result demonstrates that urease:UreD and UreD:UreF interactions are maintained when using the UreD variants, and it provides compelling evidence that these variant UreD proteins are properly folded.

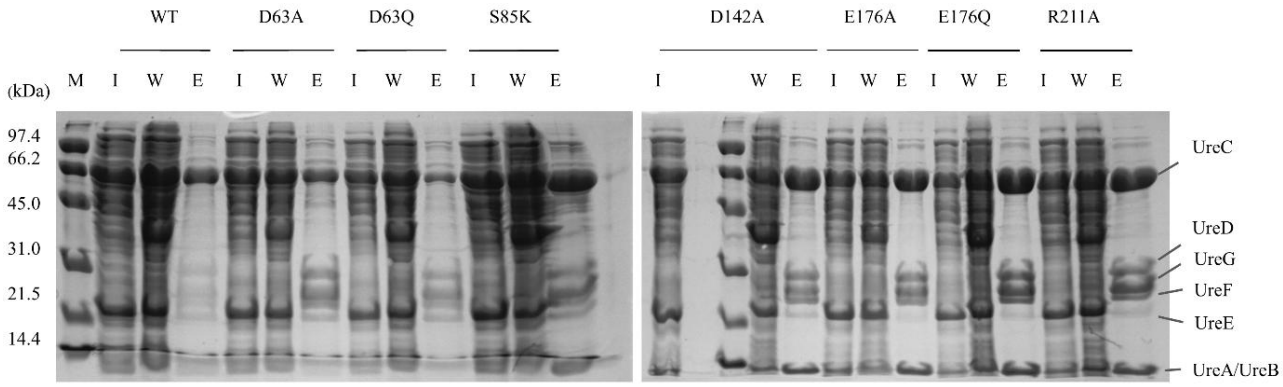

Figure 3.3: Interactions of *Ka*UreG$_{Str}$ with other *K. aerogenes* urease proteins. *E. coli* BL21(DE3) cells were transformed with pKKD*G variants producing the *Ka*UreD variants noted above the lanes. Soluble cell-free extracts (I, for input) were chromatographed on *Strep*-Tactin resin with the unbound wash (W) and the desthiobiotin-eluted (E) fractions analyzed by SDS-PAGE.

Analysis of the Metal Contents and Specific Activities of Urease Samples Activated *In Vivo* by Variant UreDs. To examine whether *ureD* mutant cultures with reduced urease activities (<30%) produced enzyme that was altered in its metal-content, the enzyme was enriched from selected *E. coli* pKKD(wild-type, D63A/Q, S85K, D142A, E176A/Q)G cells cultured in the presence of 1 mM Ni^{2+}, assayed for urease specific activity, and subjected to metal-content analysis by ICP-AES. pKKD(R211A)G, which resulted in *in vivo* activated urease with 75% of the activity of urease activated by wild type UreD, was similarly analyzed to act as a control mutation. Urease samples were enriched by chromatography on anion-exchange and size-exclusion resins to > 90% purity as determined by SDS-PAGE analysis (Figure 3.4). The resulting urease samples were assayed for their activities and yielded results (Table 3.4) that

generally paralleled the activities measured in cell-free extracts (Figure 3.2). For example, the UreD variants giving rise to reduced activity in the cell-free extracts also exhibited reduced specific activities for the enriched proteins. Detailed comparison of these results, however, underscores differences. For example, urease activity in cell-free extracts produced by D63A UreD exhibited only 3.7% of the wild-type activity, whereas the urease purified from the sample exhibited 25.7% of the wild-type enzyme activity. The samples associated with E176A UreD also yielded greater activity for the purified enzyme than expected from the cell-free extracts. In contrast, the purified urease specific activities were lower than expected on the basis of cell-free urease activities for the samples associated with D63Q and D142A UreD. On inspection of the metal-content, the enriched ureases with low urease specific activity contained less nickel than those activated with wild-type UreD and also contained varying levels of zinc and iron (Table 3.4), with the highest levels of zinc corresponding to the most inactive urease generated by activation with D142A UreD.

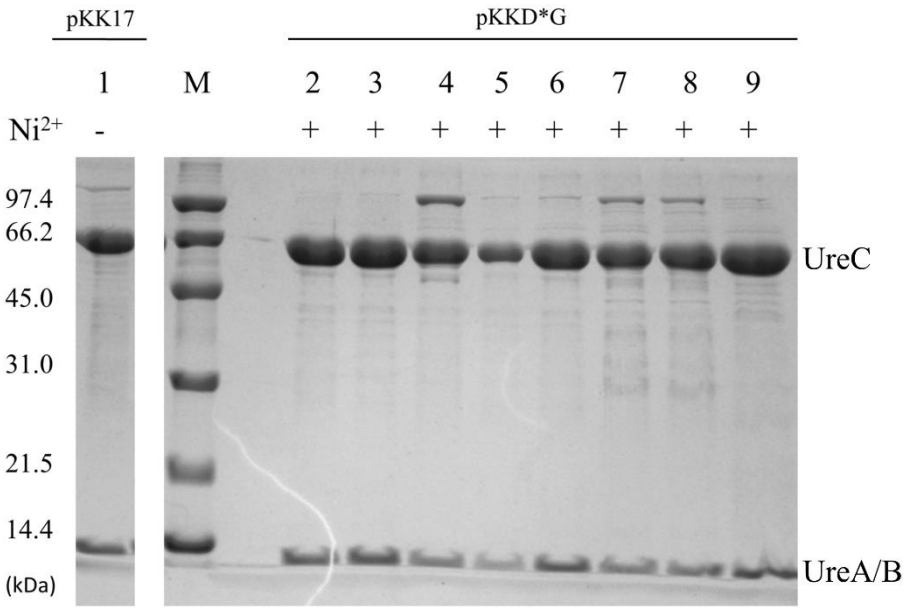

Figure 3.4: Purified urease activated *in vivo* using variant *Ka*UreDs. *E. coli* BL21(DE3) cells were transformed with either pKK17D (lane 1) or pKKD*G (lanes 2-9) and cultured in the absence or presence (- and +) of nickel. Cell-free extracts of these cultures were used for urease purification by anion exchange and size-exclusion chromatography. The resulting pools containing urease were analyzed by SDS-PAGE. The *Ka*UreDs used in cellular urease activation are as follows: lanes 1-2, WT; 3, D63A; 4, D63Q; 5, S85K; 6, D142A; 7, E176A; 8, E176Q; 9, R211A.

Table 3.4: Specific activities of urease samples enriched from cells containing selected *Ka*UreD variants.[a]

***Ka*UreD variant**	**Specific Activity[b] U/mg protein (% WT)**	**Ni/UreABC (% WT)**	**Zn/UreABC**	**Fe/UreABC**
(-), WT (pKK17D)	0	0.004 (4.0 x 10^{-5})	0.13	0.27
(+), WT (pKKDG)	1692 (100)	1.1 (100)	0	0.02
D63A	434.2 (25.7)	0.54 (49.1)	0.16	0.21
D63Q	55.71 (3.29)	0.22 (20)	0.34	0.07
S85K	487.3 (28.8)	0.39 (35.5)	0.06	0.30
D142A	14.14 (0.84)	0.07 (6.4)	0.52	0.14
E176A	1077 (63.7)	0.51 (46.4)	0.09	0.11
E176Q	375.0 (22.2)	0.43 (39.1)	0.03	0.13
R211A	1226 (72.4)	0.76 (69.1)	0.21	0.29

[a] Metal-content values were obtained from a single biological replicate. Specific activities were obtained from a single biological replicate and a triplicate of technical replicates. The urease samples were chromatographically enriched from cell-free extracts of *E. coli* pKKD*G grown in

Table 3.4 (cont'd): LB containing 1 mM $NiCl_2$, except for a sample of urease apoprotein that was obtained from *E. coli* pKK17D grown in LB lacking nickel. Metal contents were determined by ICP-AES.

[b]U is defined as μmole of urea hydrolyzed · min^{-1}.

DISCUSSION

The studies outlined here give insights into the function of *K. aerogenes* UreD during urease activation. Previous equilibrium dialysis studies of MBP-UreD showed that the fusion protein can bind upwards of 2.5 nickel per UreD promoter, with zinc competing for these sites (9). Prior ICP-AES studies quantified increased nickel content for the urease:UreD complex than for urease under activating conditions lacking bicarbonate, also supporting nickel binding to UreD (39). Lastly, a putative buried water tunnel in the UreH:UreF:UreG crystal structure was predicted to span from the likely nickel-binding site in UreG through UreF and UreH, hypothesized to function in urease activation (53); however, no direct experimental support was reported. Here, I present evidence consistent with UreD functioning directly in nickel trafficking via an internal tunnel rather than acting as a scaffold protein that transfers the metal ion via surface residues.

The mutagenesis studies detailed in this work focused on the effects of substituting 27 residues, most of which are highly conserved among UreD homologues, and characterizing the consequences of these substitutions. Mutations designed to disrupt potential metal-transfer sites on the protein surface removed charges while either retaining the overall dimensions of the residues (e.g., E165Q) or resulting in size differences (e.g., K86A). None of the UreD surface residue substitutions examined led to significant reductions of urease activity, with the largest changes noted for the K86A and Y88V variants (81% and 72%, respectively). The mild loss of urease activity associated with these substitutions led me to hypothesize that the surface residues examined are not of great importance to the function of UreD.

A second set of mutations were introduced to disrupt one or more potential internal channels of UreD. Various substitutions include the use of several long or bulky side chains designed to block the tunnels predicted by MOLE2.0 analysis of the UreD homology model. The substitutions likely to affect the exits for tunnels 3 and 4 (Figure 3.1B) resulted in no loss of *in vivo* urease activation relative to wild-type UreD. In sharp contrast, UreD variants with altered residues at the ends (E176A/Q and D63A/Q) and the section prior to the initial branch point (D142A) of tunnel 1 exhibited greatly reduced urease activation. A UreD variant designed to block the shared branch point (S85K) also possessed reduced urease activity. One UreD variant designed to block the exit of tunnel 1 (I59Y) had no appreciable effect on urease activation; however, since this residue is located on a disordered loop in the homology model, it is likely that it adopts multiple conformations that would not be accurately depicted using analysis of a static structure. Surprisingly, T196K UreD had no appreciable effect on urease activation *in vivo*, though *in silico* analysis of the available rotomers predicted blockage of the tunnel entrance. Molecular dynamics simulations of this variant, as well as the variants affecting UreD function, are currently underway to better explain this disconnect. Unfortunately, no residues facing tunnel 2 could be modeled to block or disrupt the tunnel without severe steric clashes. Taken together, these initial results are consistent with a tunnel within UreD functioning in urease activation, but loss of urease activity also could arise from disruption of protein:protein interactions. Additionally, the nature of the loss-of-urease function could arise from a mis-metallated or un-metallated enzyme produced by variant UreD. Thus, further studies were carried out to probe for UreD:protein interactions and to assess the activity and metal content of urease activated *in vivo* by variant UreD.

To characterize whether the UreD variants of interest were capable of correctly interacting with their known binding partners, namely UreABC and UreF:UreG, pull-down studies were carried out using $UreG_{Str}$. Previous studies using the $UreG_{Str}$-producing construct demonstrated that urease activation in this system was comparable to that observed when using non-tagged UreG (5). *Strep*-Tactin pull-downs of $UreG_{Str}$ from cell-free extracts of *E. coli* cells containing pKKD*G and cultured in the absence of nickel resulted in fractions containing $UreG_{Str}$ along with the urease subunits, UreD, and UreF. This result qualitatively shows that binding interactions are not disrupted when using the selected UreD variants; thus, the reduction in urease activity in cells producing these UreD variants is not due to loss of protein:protein interactions. Additionally, the ability to enrich the large complex provides evidence for the proper folding of the UreD variants. This finding is especially important in the case of the proposed tunnel-blocking S85K variant, where the introduction of a positively-charged residue buried within the protein was a point of concern.

To investigate whether the reduced urease activities correlated with nickel content for cells producing variant forms of UreD, ureases from selected cultures were enriched by anion-exchange and size-exclusion chromatography and their specific activities and metal contents were determined. The urease activities of these samples roughly correlated with their nickel contents. Of interest, samples deficient in urease activity and nickel content, including the urease apoprotein control, possessed contaminating levels of zinc and iron. Most notably, ureases activated with the D63Q and D142A UreD variants had the lowest urease activity and nickel content as well as the highest zinc occupancy. Certain UreD variants generated urease with activities less than one would expect from their nickel content (see D63A and D63Q in Table 3.4). This, the can be thought to arise from malformation of the metallocenter, as it is known that

in vitro incubation of *K. aerogenes* urease apoprotein with nickel ions and bicarbonate leads to activation of ~15% of the active sites even though the protein becomes fully loaded with nickel (39). Alternatively, the composition of metallocenters could be heterogeneous in these samples, with some active sites containing two nickel ions while others contain a nickel ion and a contaminating metal, which would result in no urease activity.

While specific alterations of UreD clearly lead to reductions in ability to insert nickel properly into the nascent active site, the function of UreE, UreG, and UreF are presumably unaltered, so acquisition of nickel by UreE, transfer to UreG, and passage through UreF should remain unaffected. Thus, one must consider how can a system designed to specifically select and position nickel for transfer through UreD allow for spurious metal incorporation (zinc and iron). It is known that accessory protein dissociation from urease occurs following urease activation *in vitro* (49); however, it has not been detailed if the process itself (nickel ejection and transport through the accessory proteins) induces the dissociation or if the incorporation of nickel results in a conformation of urease that disallows for accessory protein binding. Indeed, the latter explanation is unlikely, as it is known that the soluble maltose binding protein-UreD:UreF:UreG accessory protein complex can interact with holourease (17) and holoUreABC:UreD:UreF:UreG complexes have been observed following *in vivo* activation of urease (unpublished data). Two explanations for the presence of contaminating metals in urease are reasonable to propose. First, the metal contamination observed in these samples can explained by a failure of UreD (within the UreABC:UreD:UreF:UreG complex) to deliver nickel from UreE into urease apoprotein, allowing opportunistic metals to enter the nascent urease active site following activation-induced dissociation of the accessory proteins from urease. Alternatively, the natural dissociation of the accessory proteins from urease could also allow for contaminating metals to bind at the active

site when insufficient nickel is present within the cell, as seen in the urease apoprotein sample. *In vitro* activation trials on either UreABC:UreD:UreF:UreG or UreABC:UreD:UreF:$UreG_{Str}$ complexes would help answer this lingering question. Overall these findings provide further evidence that UreD has a direct role in facilitating metal transfer into urease and support the concept of a nickel-transfer tunnel in the protein.

In summary, the studies presented here provide evidence for a direct metal-transfer role involving a tunnel within UreD. These findings fit well with results from previous nickel-binding studies of UreABC:UreD and MBP-UreD, as well as the computational studies of UreH:UreF:UreG that demonstrated metal binding by UreD and hypothesized a functional tunnel within UreF that connected to the UreG and UreH accessory proteins (9, 39, 53).

BIBLIOGRAPHY

BIBLIOGRAPHY

1. The Pymol Molecular Graphics System, Version 1.5.0.4 Schrödinger, LLC.

2. **Andreini, C., Bertini, I., Cavallaro, G., Holliday, G. L., and Thornton, J. M.** 2008. Metal ions in biological catalysis: from enzyme databases to general principles. J. Biol. Inorg. Chem. **13**: 1205-1218.

3. **Bellucci, M., Zambelli, B., Musiani, F., Turano, P., and Ciurli, S.** 2009. *Helicobacter pylori* UreE, a urease accessory protein: specific Ni^{2+} and Zn^{2+}-binding properties and interaction with its cognate UreG. Biochem J **422**: 91-100.

4. **Boer, J. L., and Hausinger, R. P.** 2012. *Klebsiella aerogenes* UreF: identification of the UreG binding site and role in enhancing the fidelity of urease activation. Biochemistry **51**: 2298-2308.

5. **Boer, J. L., Quiroz-Valenzuela, S., Anderson, K. L., and Hausinger, R. P.** 2010. Mutagenesis of *Klebsiella aerogenes* UreG to probe nickel binding and interactions with other urease-related proteins. Biochemistry **49**: 5859-5869.

6. **Braun, V., and Hantke, K.** 2011. Recent insights into iron import by bacteria. Curr. Opin. Chem. Biol. **15**: 328-334.

7. **Carrondo, M. A.** 2003. Ferritins, iron uptake and storage from the bacterioferritin viewpoint. EMBO J. **22**: 1959-1968.

8. **Carter, E. L., Boer, J. L., Farrugia, M. A., Flugga, N., Towns, C. L., and Hausinger, R. P.** 2011. Function of UreB in *Klebsiella aerogenes* urease. Biochemistry **50**: 9296-9308.

9. **Carter, E. L., and Hausinger, R. P.** 2010. Characterization of the *Klebsiella aerogenes* urease accessory protein UreD in fusion with the maltose binding protein. J. Bacteriol. **192**: 2294-2304.

10. **Carter, E. L., Proshlyakov, D. A., and Hausinger, R. P.** 2012. Apoprotein isolation and activation, and vibrational structure of the *Helicobacter mustelae* iron urease. J. Inorg. Biochem. **111**: 195-202.

11. **Casalot, L., and Rousset, M.** 2001. Maturation of the [NiFe] hydrogenases. Trends Microbiol. **9**: 228-237.

12. **Celniker, G., Nimrod, G., Ashkenazy, H., Glaser, F., Martz, E., Mayrose, I., Pupko, T., and Ben-Tal, N.** 2013. ConSurf: using evolutionary data to raise testable hypotheses about protein function. Isr. J. Chem. **53**: 199-206.

13. **Chovancova, E., Pavelka, A., Benes, P., Strnad, O., Brezovsky, J., Kozlikova, B., Gora, A., Sustr, V., Klvana, M., Medek, P., Biedermannova, L., Sochor, J., and Damborsky, J.** 2012. CAVER 3.0: a tool for the analysis of transport pathways in dynamic protein structures. PLoS Comput. Biol. **8**: e1002708.

14. **Cobine, P. A., Pierrel, F., and Winge, D. R.** 2006. Copper trafficking to the mitochondrion and assembly of copper metalloenzymes. Biochim. Biophys. Acta **1763**: 759-772.

15. **Colpas, G. J., Brayman, T. G., Ming, L. J., and Hausinger, R. P.** 1999. Identification of metal-binding residues in the *Klebsiella aerogenes* urease nickel metallochaperone, UreE. Biochemistry **38**: 4078-4088.

16. **Cox, G. M., Mukherjee, J., Cole, G. T., Casadevall, A., and Perfect, J. R.** 2000. Urease as a virulence factor in experimental cryptococcosis. Infect. Immun. **68**: 443-448.

17. **Farrugia, M. A., Han, L., Zhong, Y., Boer, J. L., Ruotolo, B. T., and Hausinger, R. P.** 2013. Analysis of a soluble $(UreD:UreF:UreG)_2$ accessory protein complex and its interactions with *Klebsiella aerogenes* urease by mass spectrometry. J. Am. Soc. Mass. Spectrom. **24**: 1328-1337.

18. **Farrugia, M. A., Macomber, L., and Hausinger, R. P.** 2013. Biosynthesis of the urease metallocenter. J. Biol. Chem. **288**: 13178-13185.

19. **Fong, Y. H., Wong, H. C., Chuck, C. P., Chen, Y. W., Sun, H., and Wong, K. B.** 2011. Assembly of preactivation complex for urease maturation in *Helicobacter pylori*: crystal structure of UreF-UreH protein complex. J. Biol. Chem. **286**: 43241-43249.

20. **Fong, Y. H., Wong, H. C., Yuen, M. H., Lau, P. H., Chen, Y. W., and Wong, K. B.** 2013. Structure of UreG/UreF/UreH complex reveals how urease accessory proteins facilitate maturation of *Helicobacter pylori* urease. PLoS. Biol. **11**: e1001678.

21. **Ge, R. G., Wang, D. X., Hao, M. C., and Sun, X. S.** 2013. Nickel trafficking system responsible for urease maturation in *Helicobacter pylori*. World J. Gastroenterol. **19**: 8211-8218.

22. **Ha, N. C., Oh, S. T., Sung, J. Y., Cha, K. A., Lee, M. H. and Oh, B. H.** 2001. Supramolecular assembly and acid resistance of *Helicobacter pylori* urease. Nat. Struct. Biol. **8**: 505-9.

23. **Holm, R. H., Kennepohl, P., and Solomon, E. I.** 1996. Structural and functional aspects of metal sites in biology. Chem. Rev. **96**: 2239-2314.

24. **Hu, Y., Fay, A. W., Lee, C. C., Yoshizawa, J., and Ribbe, M. W.** 2008. Assembly of nitrogenase MoFe protein. Biochemistry **47**: 3973-3981.

25. **Jabri, E., Carr, M. B., Hausinger, R. P., and Karplus, P. A.** 1995. The crystal structure of urease from *Klebsiella aerogenes*. Science **268**: 998-1004.

26. **Johnson, M., Zaretskaya, I., Raytselis, Y., Merezhuk, Y., McGinnis, S., and Madden, T. L.** 2008. NCBIBLAST: a better web interface. Nucleic Acids Res. **36**: W5-W9.

27. **Kelley, L. A., and Sternberg, M. J.** 2009. Protein structure prediction on the Web: a case study using the Phyre server. Nat. Protoc. **4**: 363-371.

28. **Kim, J. K., Mulrooney, S. B., and Hausinger, R. P.** 2006. The UreEF fusion protein provides a soluble and functional form of the UreF urease accessory protein. J. Bacteriol. **188**: 8413-8420.

29. **Lam, R., Romanov, V., Johns, K., Battaile, K. P., Wu-Brown, J., Guthrie, J. L., Hausinger, R. P., Pai, E. F., and Chirgadze, N. Y.** 2010. Crystal structure of a truncated urease accessory protein UreF from *Helicobacter pylori*. Proteins **78**: 2839-2848.

30. **Lee, M. H., Mulrooney, S. B., Renner, M. J., Markowicz, Y., and Hausinger, R. P.** 1992. *Klebsiella aerogenes* urease gene cluster: sequence of *ureD* and demonstration that four accessory genes (*ureD*, *ureE*, *ureF*, and *ureG*) are involved in nickel metallocenter biosynthesis. J. Bacteriol. **174**: 4324-4330.

31. **McWilliam, H., Li, W., Uludag, M., Squizzato, S., Park, Y. M., Buso, N., Cowley, A. P., and Lopez, R.** 2013. Analysis Tool Web Services from the EMBL-EBI. Nucleic Acids Res. **41**: W597-600.

32. **Merloni, A., Dobrovolska, O., Zambelli, B., Agostini, F., Bazzani, M., Musiani, F., and Ciurli, S.** 2014. Molecular landscape of the interaction between the urease accessory proteins UreE and UreG. Biochim. Biophys. Acta **1844**: 1662-1674.

33. **Mobley, H. L., and Hausinger, R. P.** 1989. Microbial ureases: significance, regulation, and molecular characterization. Microbiol. Rev. **53**: 85-108.

34. **Moncrief, M. B., and Hausinger, R. P.** 1997. Characterization of UreG, identification of a UreD-UreF-UreG complex, and evidence suggesting that a nucleotide-binding site in UreG is required for *in vivo* metallocenter assembly of *Klebsiella aerogenes* urease. J. Bacteriol. **179**: 4081-4086.

35. **Mulder, D. W., Boyd, E. S., Sarma, R., Lange, R. K., Endrizzi, J. A., Broderick, J. B., and Peters, J. W.** 2010. Stepwise [FeFe]-hydrogenase H-cluster assembly revealed in the structure of $HydA^{(\Delta EFG)}$. Nature **465**: 248-251.

36. **Mulrooney, S. B., Pankratz, H. S., and Hausinger, R. P.** 1989. Regulation of gene expression and cellular localization of cloned *Klebsiella aerogenes* (*K. pneumoniae*) urease. J. Gen. Microbiol. **135**: 1769-1776.

37. **Musiani, F., Zambelli, B., Stola, M., and Ciurli, S.** 2004. Nickel trafficking: insights into the fold and function of UreE, a urease metallochaperone. J. Inorg. Biochem. **98**: 803-813.

38. **Park, I. S., Carr, M. B., and Hausinger, R. P.** 1994. *In vitro* activation of urease apoprotein and role of UreD as a chaperone required for nickel metallocenter assembly. Proc. Natl. Acad. Sci. U.S.A. **91**: 3233-3237.

39. **Park, I. S., and Hausinger, R. P.** 1996. Metal ion interaction with urease and UreD-urease apoproteins. Biochemistry **35**: 5345-5352.

40. **Quiroz-Valenzuela, S., Sukuru, S. C., Hausinger, R. P., Kuhn, L. A., and Heller, W. T.** 2008. The structure of urease activation complexes examined by flexibility analysis, mutagenesis, and small-angle X-ray scattering. Arch. Biochem. Biophys. **480**: 51-57.

41. **Rees, T. A., and Bekheet, I. A.** 1982. The role of nickel in urea assimilation by algae. Planta **156**: 385-387.

42. **Robinson, N. J., and Winge, D. R.** 2010. Copper metallochaperones. Annu. Rev. Biochem. **79**: 537-562.

43. **Rosenzweig, A. C.** 2002. Metallochaperones: bind and deliver. Chem. Biol. **9**: 673-677.

44. **Schmidt, P. J., Ramos-Gomez, M., and Culotta, V. C.** 1999. A gain of superoxide dismutase (SOD) activity obtained with CCS, the copper metallochaperone for SOD1. J Biol. Chem. **274**: 36952-36956.

45. **Sehnal, D., Varekovaa, R. S., Berka, K., Pravda, L., Navratilova, V., Banas, P., Ionescu, C. M., Otyepka, M., and Koca, J.** 2013. MOLE 2.0: advanced approach for analysis of biomacromolecular channels. J. Cheminform. **5**.

46. **Shi, R., Munger, C., Asinas, A., Benoit, S. L., Miller, E., Matte, A., Maier, R. J., and Cygler, M.** 2010. Crystal structures of apo and metal-bound forms of the UreE protein from *Helicobacter pylori*: role of multiple metal binding sites. Biochemistry **49**: 7080-7088.

47. **Sirko, A., and Brodzik, R.** 2000. Plant ureases: roles and regulation. Acta Biochim. Pol. **47**: 1189-1195.

48. **Song, H. K., Mulrooney, S. B., Huber, R., and Hausinger, R. P.** 2001. Crystal structure of *Klebsiella aerogenes* UreE, a nickel-binding metallochaperone for urease activation. J. Biol. Chem. **276**: 49359-49364.

49. **Soriano, A., and Hausinger, R. P.** 1999. GTP-dependent activation of urease apoprotein in complex with the UreD, UreF, and UreG accessory proteins. Proc. Natl. Acad. Sci. U.S.A. **96**: 11140-11144.

50. **Strugatsky, D., McNulty, R., Munson, K., Chen, C. K., Soltis, S. M., Sachs, G., and Luecke, H.** 2013. Structure of the proton-gated urea channel from the gastric pathogen *Helicobacter pylori*. Nature **493**: 255-258.

51. **Vieira, J. and Messing, J.** 1982. The pUC plasmids, an M13mp7-derived system for insertion mutagenesis and sequening with synthetic universal primers. Gene **19**: 259-68

52. **Weatherburn, M. W.** 1967. Phenol-hypochlorite reaction for determination of ammonia. Anal. Chem. **39**: 971-974.

53. **Zambelli, B., Berardi, A., Martin-Diaconescu, V., Mazzei, L., Musiani, F., Maroney, M. J., and Ciurli, S.** 2014. Nickel binding properties of *Helicobacter pylori* UreF, an accessory protein in the nickel-based activation of urease. J. Biol. Inorg. Chem. **19**: 319-334.

54. **Zambelli, B., Turano, P., Musiani, F., Neyroz, P., and Ciurli, S.** 2009. Zn^{2+}-linked dimerization of UreG from *Helicobacter pylori*, a chaperone involved in nickel trafficking and urease activation. Proteins **74**: 222-239.

CHAPTER 4

Further Insights into the Metallocenter Vibrational Structure of *Helicobacter mustelae* UreA2B2

ABSTRACT

The enzyme urease has been studied for nearly one-hundred years, but several questions involving the mechanism and substrate coordination of this nickel metalloenzyme still remain unanswered. The discovery of an oxygen-sensitive, di-iron urease from *Helicobacter mustelae* (UreA2B2) offers the potential to address some of these questions by use of spectroscopic investigations that are inaccessible to the nickel enzyme due to its spectroscopically-silent active site. Previous resonance Raman investigations of oxidized UreA2B2 provided evidence for an Fe(III)-O-Fe(III) site that is solvent-exchange inert, even when subjected to a reduction/oxidation cycle. Additionally, the vibrations associated with oxidized UreA2B2 were found to be sensitive to the addition of urea, indicative of either a binding event or protein conformational changes due to chaotropic effects. Here, I report new resonance Raman studies of UreA2B2 that demonstrate the bridging oxygen species is a μ-oxo species which does, in fact, exchange when the enzyme is redox cycled. I show the urea sensitivities observed previously are reversed by buffer exchange and are not due to chaotropic effects, but arise from substrate interaction at the di-ferric metallocenter. Additionally, I provide evidence that a known inhibitor of conventional nickel ureases, phenyl phosphorodiamidate, yields a downshift equivalent in magnitude to that observed with urea, whereas the inhibitor acetohydroxamic acid has no effect on the spectrum. I present observations of a terminal hydroxide ligand that is not completely displaced on urea binding, supporting a model where urea does not coordinate to oxidized UreA2B2 via displacement of all terminal ligands. The discovery of a slow-binding form of UreA2B2 is also discussed, and its solvent sensitivities are shown to be comparable to those of the fast-binding form of the enzyme. Finally, I highlight that neither ^{15}N-labeled nor ^{18}O-labeled urea generate additional downshifts

relative to normal abundance urea. These studies further define the vibrational features of the only iron-containing urease identified.

INTRODUCTION

Urease catalyzes the hydrolysis of urea into a molecule of ammonia and carbamate (10), which subsequently decomposes into a second molecule of ammonia and bicarbonate. The enzyme is found in all plants (17, 21), as well as certain bacteria, algae, Archaea and fungi (6, 14, 15, 17). Urease is the first nickel-containing enzyme to be discovered (7) and has been identified as a virulence factor in the ulcerative human-pathogen *Helicobacter pylori* (9). An abundance of structural information exists on urease from jack bean seeds (2), *Sporosarcina* (formerly *Bacillus*) *pasteurii* (3), *H. pylori* (11), and the archetype nickel-urease from *Klebsiella aerogenes* (12). These structures reveal a highly conserved active site architecture containing two nickel atoms bridged by a carbamylated lysine side chain and a μ-hydroxy solvent molecule, with one nickel additionally coordinated by two histidine residues and a terminal solvent molecule, and the other metal coordinated by two histidine residues, an aspartic acid residue, and a terminal solvent molecule. Attempts to design experiments to probe the mechanism of this di-nickel site, however, are stymied by the spectroscopically silent nature of these metal atoms. This limitation partially spurred investigations into ureases that can utilize alternative, more tractable metals in their catalysis.

UreA2B2 is a urease from the ferret pathogen *Helicobacter mustelae*. This organism contains a typical *Helicobacter*-like nickel-urease gene cluster (*ureABIEFGH*) that is induced by nickel, with a second gene cluster containing genes homologous to the urease structural genes (*ureA2B2*) that are regulated by iron and negatively regulated by nickel (20). UreA2 and UreB2 exhibit high sequence conservation with UreA and UreB (57.4% and 69.5% identity, respectively) (5). Structural and biochemical characterization of this enzyme reveals the same coordinating residues and geometries as found in the nickel-containing ureases, but with iron in

place of nickel (Figure 4.1) (5). Despite the active site similarities, the *K. aerogenes* apoenzyme is activated *in vitro* by bicarbonate and nickel or (anaerobically) iron, whereas the partial apoprotein of the *H. mustelae* protein is only activated by bicarbonate plus iron. Ultraviolet (UV)-visible (vis) spectra of oxidized UreA2B2 reveal absorption features (320, 380, and 500 nm) reminiscent of the μ-oxo bridged, diferric centers of methemerythrin and oxyhemerythrin (8, 16). These electronic features are bleached upon chemical reduction under anaerobic conditions, accompanied by the generation of active enzyme. The fully reduced enzyme exhibits no electron paramagnetic resonance (EPR) spectrum in the standard perpendicular mode, as expected for the diferrous state, while the oxidized sample also yields no EPR signal, consistent with antiferromagnetic coupling between the two ferric ions. Together, these results identify UreA2B2 as an iron-containing metalloenzyme, the first urease identified to function with this metal, with a bridging oxo-species coupling the two metals in the oxidized sample. This diferric form of the enzyme uniquely allows for vibrational spectroscopy characterization of the metalloenter under various conditions by using resonance Raman methods.

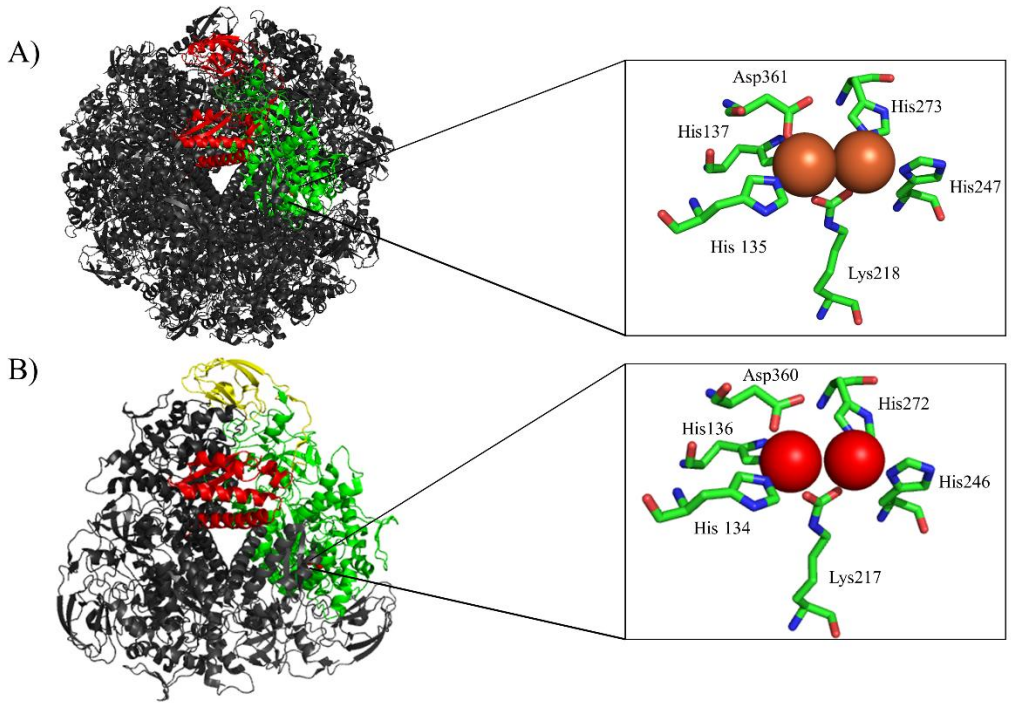

Figure 4.1: Structural comparison of iron- and nickel-dependent ureases. (A) The crystal structure of *H. mustelae* $((UreA2B2)_3)_4$ (PDB: 3QGA). One protomer of UreA2 is depicted as a red cartoon and one protomer of UreB2 is depicted as a green cartoon. The remaining protomers are depicted in dark grey. (B) The crystal structure of *K. aerogenes* $(UreABC)_3$ (PDB: 1EJW). One promoter each of UreA, UreB and UreC are depicted in red, yellow, and green cartoon, respectively. The remaining promoters are depicted in dark grey. The active-site residues for UreA2B2 (top) and UreABC (bottom) are shown on the right. Iron is depicted in orange, while nickel is displayed in red.

Resonance Raman spectroscopic characterization of UreA2B2 reveals an intense Raman shift at 500 cm^{-1} and an additional mode at ~790 cm^{-1} that are downshifted by addition of urea, but are insensitive to rapid bulk solvent ($H_2{}^{18}O$) exchange (4). These findings, together with the EPR and structural studies highlighted above, suggested that the 500 cm^{-1} and 790 cm^{-1} modes are the symmetric (ν_s) and asymmetric (ν_{as}) vibrational modes from a μ-oxo bridged, diferric metallocenter. Surprisingly, the μ-oxo group also was reported to be solvent exchange-inert during a reduction/oxidation cycle, which could be invaluable for designing experiments to probe the catalytic mechanism of urease (e.g., testing whether the bridging solvent molecule is the nucleophile in catalysis). The nature of the urea-induced vibrational downshifts was not

examined (4), and one could speculate that the shift arises from urea coordination at or near the metallocenter or that it stems from a chaotropic effect of urea. Should this effect be defined as a binding event, one could further test whether the presence of urea at the metallocenter of UreA2B2 affects the previously identified $H_2{}^{18}O$ bulk solvent modes attributed tentatively as terminal Fe-OH modes (4). This type of spectroscopic analysis of ligand-binding can also be expanded to test whether known nickel-urease inhibitors generate UreA2B2 Raman shifts similar to those induced by urea binding. In addition, the effect of urea isotopes on the Raman spectrum of UreA2B2 could provide some evidence for how substrate coordinates to the metallocenter.

The work described here addresses the gaps in knowledge described above and further characterizes the metallocenter of oxidized UreA2B2 using resonance Raman spectroscopy. My studies identified a purification-dependent heterogeneity in UreA2B2 presenting as a slow substrate-binding form of the enzyme and a fast substrate-binding form. In contrast to prior results, I found that anaerobic reduction and chemical oxidation of UreA2B2 in the presence of isotopic solvent led to exchange of the μ-oxo group; hence, identification of the nucleophile in catalysis by assessing retention of this atom was not feasible. Additionally, I demonstrated that the urea-induced mode shifts are not reproduced with a different chaotropic agent, and I examined the effects of conventional urease inhibitors on the Raman spectra. Binding of either ^{15}N- or ^{18}O-labeled urea to UreA2B2 led to no additional downshifts in the UreA2B2 Raman spectrum, nor did the presence of D_2O affect the primary bridging mode. This latter finding gives further evidence that the bridging species is indeed oxo as opposed to hydroxo. My findings presented here provide further insights into the nature of the metallocenter in this unique urease.

MATERIALS AND METHODS

Purification, Protein Concentration, and Activity Assays of UreA2B2. The UreA2B2 holoprotein was prepared as described previously (4), with minor modifications, from *E. coli* BL21(DE3) cells transformed with pEC015 (5). Either Sephacryl S300-HR or Superdex-200 resin (GE healthcare) was used for gel filtration chromatography, with no obvious difference in separations between the resins. Fractions containing UreA2B2 were analyzed by sodium dodecyl sulfate polyacrylamide gel electrophoresis using 4% stacking and 12% running gels, and the protein bands were visualized by Coomassie blue staining. Purified samples were subjected to UV-vis spectroscopy to assess the presence of the antiferromagnetically-coupled diferric metallocenter associated with features at 500, 380, and 320 nm. Urease activity of anaerobic, reduced UreA2B2 was assayed as described previously (5).

Protein concentrations were assayed in triplicate by using a commercially available colorimetric protein assay kit (Bio-Rad).

Isotopic Exchange of the UreA2B2 Oxygen Bridge with Bulk Solvent. To re-investigate the exchange of the bridging oxo-species, chemical reduction and oxidation of anaerobic UreA2B2 was performed in buffers containing HPLC grade $H_2{}^{16}O$ (Fisher Scientific) or $H_2{}^{18}O$ (ICON Isotopes). Aerobically purified, UreA2B2 (3 mM) was exchanged into 250 mM HEPES, pH 7.8, buffer containing 5 mM EDTA and gas exchanged by injecting into an argon-filled vial and incubating on ice overnight. Solutions of 50 mM HEPES, 1 mM EDTA, pH 7.8, buffer, HPLC grade $H_2{}^{16}O$, and $H_2{}^{18}O$ were made anaerobic with a minimum of 5 cycles of vacuum (10 min)/argon replacement (10 min) on a Schlenk line. Powders of sodium dithionite ($Na_2S_2O_4$) and potassium ferricyanide (Sigma-Aldrich) were made anaerobic with 3 cycles of vacuum (2 min)/argon replacement (2 min). The following steps, unless otherwise noted, were

performed in a 100% N_2 glove bag (PlasLabs). Solutions of UreA2B2 (3 mM) were reduced with 5 mM of $Na_2S_2O_4$ at room temperature for 2 h. Samples were diluted with 2 or 4 volumes of solvent ($H_2{}^{16}O$ or $H_2{}^{18}O$ at 40 or 80% isotope enrichment, respectively), incubated for 30 min at room temperature, and chemically oxidized with 3 mM potassium ferricyanide. To test whether substrate turnover facilitated exchange of the bridging oxygen, samples of UreA2B2 were reduced and isotopically enriched as described above then incubated with 50 mM urea for one h at 37 °C. To confirm successful turnover, an aliquot was removed and assayed for urease activity under anoxic conditions. Samples were desalted with sequential concentration and dilution in 28 mM TAPS, pH 8.4, buffer using Amicon® Ultra-0.5 centrifugal filters.

The effects of bulk isotopic solvent on UreA2B2 in the absence or redox cycling or substrate were determined for rapid (min) exchange. Desalted samples were concentrated 10-fold and diluted with 9 volumes of the appropriate solvent for brief time periods prior to Raman analysis. To examine the effects of urea on the observed solvent-sensitive modes, samples of UreA2B2 were incubated with varied concentrations of urea. In some cases, these experiments were combined with solvent exchange, as noted above.

The Effects of Substrate, Chaotropic Agents, and Inhibitors on the Raman Spectrum of UreA2B2. To determine if the resonance Raman vibrational modes observed in this work and previously (5) are a result of a chaotropic effect or due to coordination to the metallocenter, samples of untreated UreA2B2 or samples treated as described above were incubated with 30 mM urea or 30 mM guanidinium chloride for 20 min before being analyzed by resonance Raman spectroscopy. To test whether the urea-induced mode shift could be reversed by the removal of urea, samples of UreA2B2 were incubated with 20 mM urea overnight and analyzed by resonance Raman spectroscopy to confirm the presence of the urea-induced mode

shift. Samples were then exchanged 900-fold into 28 mM Tris-HCl, pH 7.4, and analyzed again by resonance Raman spectroscopy. To determine if the rate of urea binding in UreA2B2 can be increased following substrate-binding and removal via dialysis, a sample of this enzyme was incubated overnight with 60 mM urea and dialyzed 1,000,000-fold into 280 mM TAPS, pH 8.4, over an additional two days at 4 °C. In addition, the effects on UreA2B2 vibrational modes of known inhibitors for the conventional nickel urease were examined: phenyl phosphorodiamidate (PPD: ICN Biochemicals) or acetohydroxamic acid (AHA: Sigma-Aldrich). Samples of UreA2B2 (300 µM) were incubated with 2 mM AHA, 2 mM PPD, or a buffer blank overnight on ice before being analyzed by resonance Raman spectroscopy.

Effect of pH on the Rate of Urea-Induced Shifts on UreA2B2. The effect of pH on the rate of urea-induced Raman shifts was determined by dialyzing 300 µl of 200 µM UreA2B2 against 300 ml of 28 mM CHES (pH 9.4), TAPS (pH 8.4), Tris-Base (pH 7.4), or MES (pH 6.4) overnight. Samples were incubated with 26 mM urea briefly (< 1 min) before being analyzed by resonance Raman spectroscopy.

Resonance Raman Spectroscopy. Resonance Raman analysis of UreA2B2 samples and buffer components was performed using the 406.7 nm excitation wavelength (20 mW) of a Kr^+ laser (model I-90, Coherent Inc., CA). Sample aliquots (90-105 µl) were subjected to Raman spectroscopy using a spinning cell cuvette. Scattered light was collected at right angle geometry and analyzed by using a single polychromator (model Triax 550, Jobin Yvon, NJ) containing a liquid N_2-cooled CCD detector (model Spectrum One, Jobin Yvon, NJ). Spectra were acquired in 10 s intervals over 3-60 min. Time periods during which the intensities of the excited modes were stable were integrated to provide a time-averaged Raman spectra. A 2400 ln/mm grating and slit width of 0.1 µm were used for all experiments. Difference plots were obtained by

subtracting one absolute spectrum from another. In some cases, a spline function was used to normalize the baseline of the spectrum.

RESULTS

Resonance Raman Spectra, the Effect of pH, and Identification of Fast and Slow Substrate-Binding Forms of UreA2B2 at 406.7 nm Excitation. I collected resonance Raman spectra of oxidized UreA2B2 using 406.7 nm excitation and found it to be largely similar to the previously described spectra obtained using 363.8 nm and 413.1 nm (4). The 406.7 nm excitation was chosen to circumvent a photo-degradative phenomena observed from extended exposure of the sample to the 363.8 nm laser (data not shown). Excitation of as-purified UreA2B2 revealed the same ν_s(Fe-O-Fe) mode at 500 cm^{-1} and the ν_{as}(Fe-O-Fe) at ~782 cm^{-1} as observed in previous work (4). Incubation of UreA2B2 with urea resulted in downshifts of these modes to 487 and 765 cm^{-1}, respectively (Figure 4.2). The substrate incubation time required for the complete downshift of the ν_s(Fe-O-Fe) mode was observed to be short (<5 min), and the downshift was shown to be more rapid at pH 8.4 than at pH 7.4 (Figure 4.3). Overnight dialysis into buffer pH's of 6.4 and 9.4 resulted in protein precipitation. Additional studies revealed that 2 mM urea was sufficient to induce a complete downshift of the ν_s(Fe-O-Fe) (data not shown), though typically the studies presented in this work were performed with concentrations in excess of this value (60 mM). Curiously, however, several purifications of the enzyme presented with a slow urea-binding phenotype characterized by a much slower rate of urea-induced downshift (> 3 hours, Figure 4.4). No obvious differences in protein purification, handling, or storage were noted between the two phenotypes of UreA2B2. Overall, the resonance Raman spectra of the two forms of the enzyme were shown to be identical in the positions and magnitudes of their Raman shifts under all conditions tested and only differ in the time needed to obtain complete red- or

blue-shifts. No distinction will be made between the two forms of the enzyme for the remainder of this chapter.

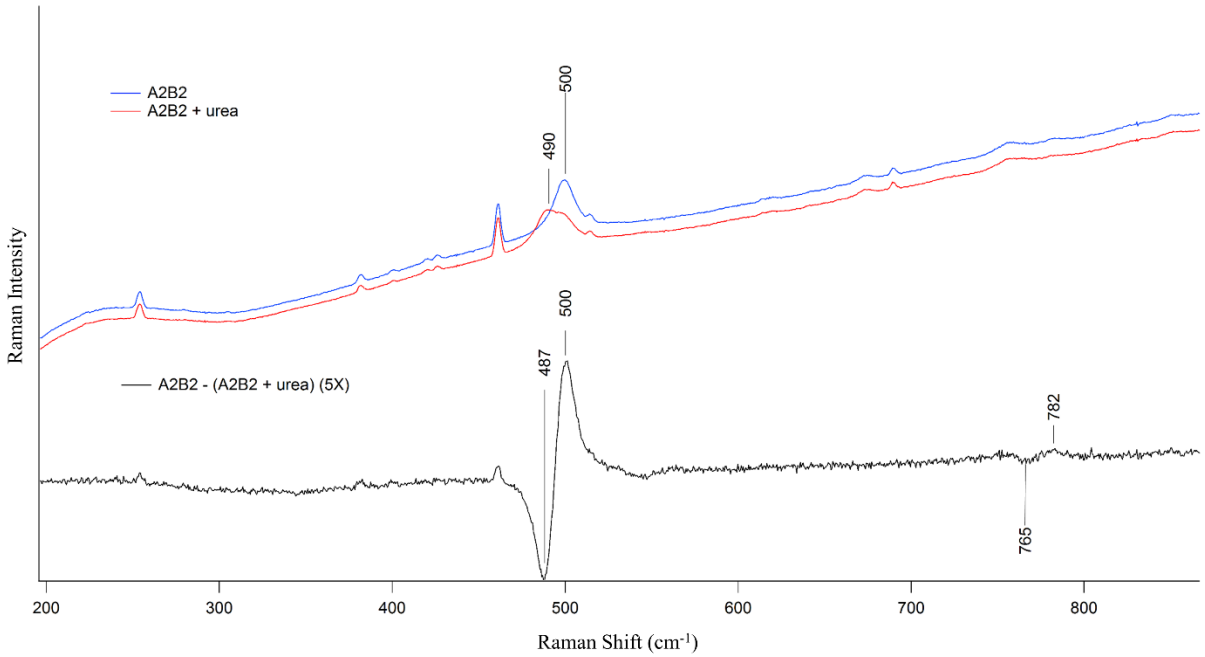

Figure 4.2: Representative resonance Raman absolute and difference spectra of oxidized UreA2B2 (blue) and sample that had been incubated with 60 mM urea (red). Urea-sensitive modes are highlighted by a difference plot (black trace). Noted Raman shift positions are displayed in units of inverse wavelength (cm^{-1})

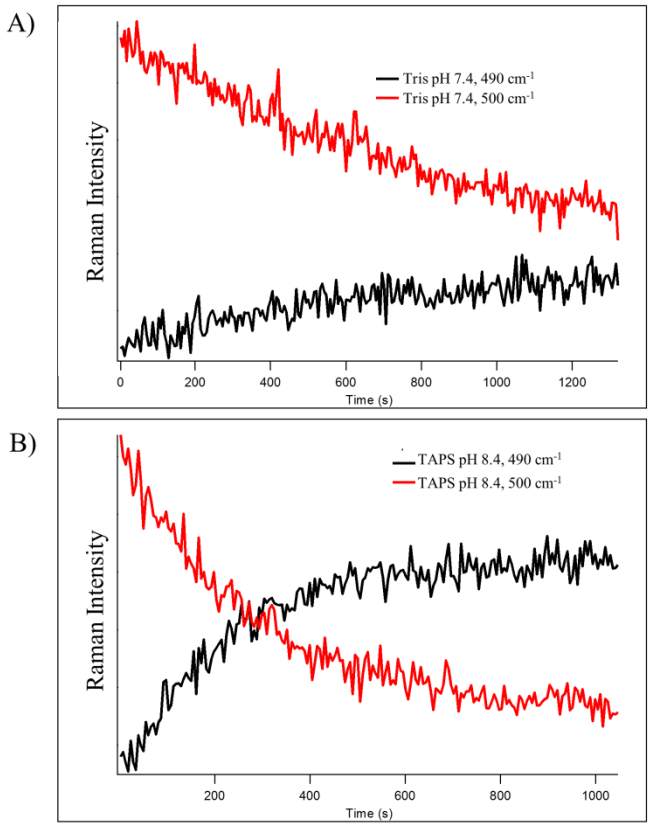

Figure 4.3: Rate of urea-induced Raman downshift at different pH values. Samples of aerobic, oxidized UreA2B2 were supplemented with 26 mM urea and scanned by resonance Raman spectroscopy immediately afterwards. Changes in intensity over time for the urea-unbound (500 cm^{-1}, red trace) and urea-bound (490 cm^{-1}, black trace) Raman shifts are shown for UreA2B2 at (A) pH 7.4 and (B) pH 8.4. Time (s) represents time post-exposure to the laser source and Raman intensity here represents relative abundance of each species at a given time.

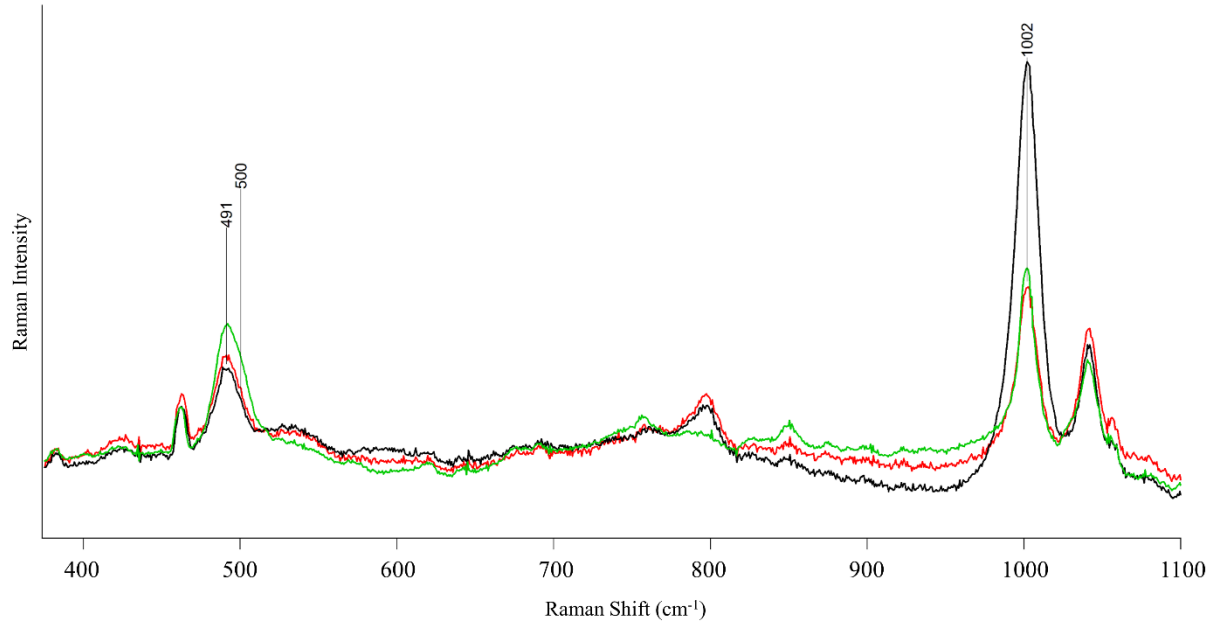

Figure 4.4: Evidence of slow substrate binding to UreA2B2. Samples of oxidized, aerobic UreA2B2 were incubated with 60 mM urea for three h (green) or overnight (red) or with 180 mM urea overnight (black trace) and analyzed by resonance Raman spectroscopy. A shoulder present at 500 cm^{-1} indicates binding is incomplete after 3 h, while overnight incubation at the same concentration of urea lacks this shoulder. The feature shown at 1000 cm^{-1} is an internal vibration of urea.

Anaerobic Chemical Reduction and Oxidation Facilitates the Complete Bridge-Exchange for UreA2B2. The reported resistance to isotopic substitution of the µ-oxo bridge during anaerobic redox cycling (4) was reexamined. Anaerobic samples of oxidized UreA2B2 were subjected to reduction with $Na_2S_2O_4$ in the presence or absence of urea and confirmed to be reduced by assaying for urease activity under anaerobic conditions (data not shown). Resonance Raman spectra of UreA2B2 that had been reduced in $H_2{}^{18}O$ in the presence or absence of urea and then oxidized with potassium ferricyanide revealed complete and symmetric downshifts of the ν_s(Fe-O-Fe) from 500 cm^{-1} to 484 cm^{-1} and of the ν_{as}(Fe-O-Fe) modes from 783 cm^{-1} to 742 cm^{-1} (Figure 4.5A and B). These downshifted modes remained present following extensive desalting of the oxidized sample in buffer prepared with $H_2{}^{16}O$. The 16 cm^{-1} downshift of the ν_s is in good agreement with $^{16}O/^{18}O$-shifts observed in other µ-oxo bridged enzymes (16, 19), but

it contradicts the previously reported, exchange-inert behavior of UreA2B2. The ν_{as}(Fe-O-Fe) mode shift was close to that observed in methemerythrin (16), but the weakness in the intensity of this mode made attaining Raman shift numbers difficult. The complete downshifts of the ν_s(Fe-O-Fe) and ν_{as}(Fe-O-Fe) modes allowed me to test the number of and coordination state of oxygens incorporated into the bridging site by redox cycling UreA2B2 in 40% $H_2{}^{18}O$ solvent. The difference spectrum for UreA2B2 cycled in $H_2{}^{16}O$ or 80% $H_2{}^{18}O$ versus UreA2B2 cycled in 40% $H_2{}^{18}O$ showed only two Raman shift positions, which supports assignment of the bridging oxo species as a μ-oxo bridge involving one oxo species as opposed to a bis(μ-oxo) bridge, which would present as three Raman shift positions in the mixed isotope spectrum (Figure 4.5A). Incubation of ^{18}O-substituted UreA2B2 with urea led to further downshifts of the ν_s and ν_{as}(Fe-O-Fe) modes that are equivalent in magnitude relative to those observed in the ^{16}O-substituted enzyme (Figure 4.5C).

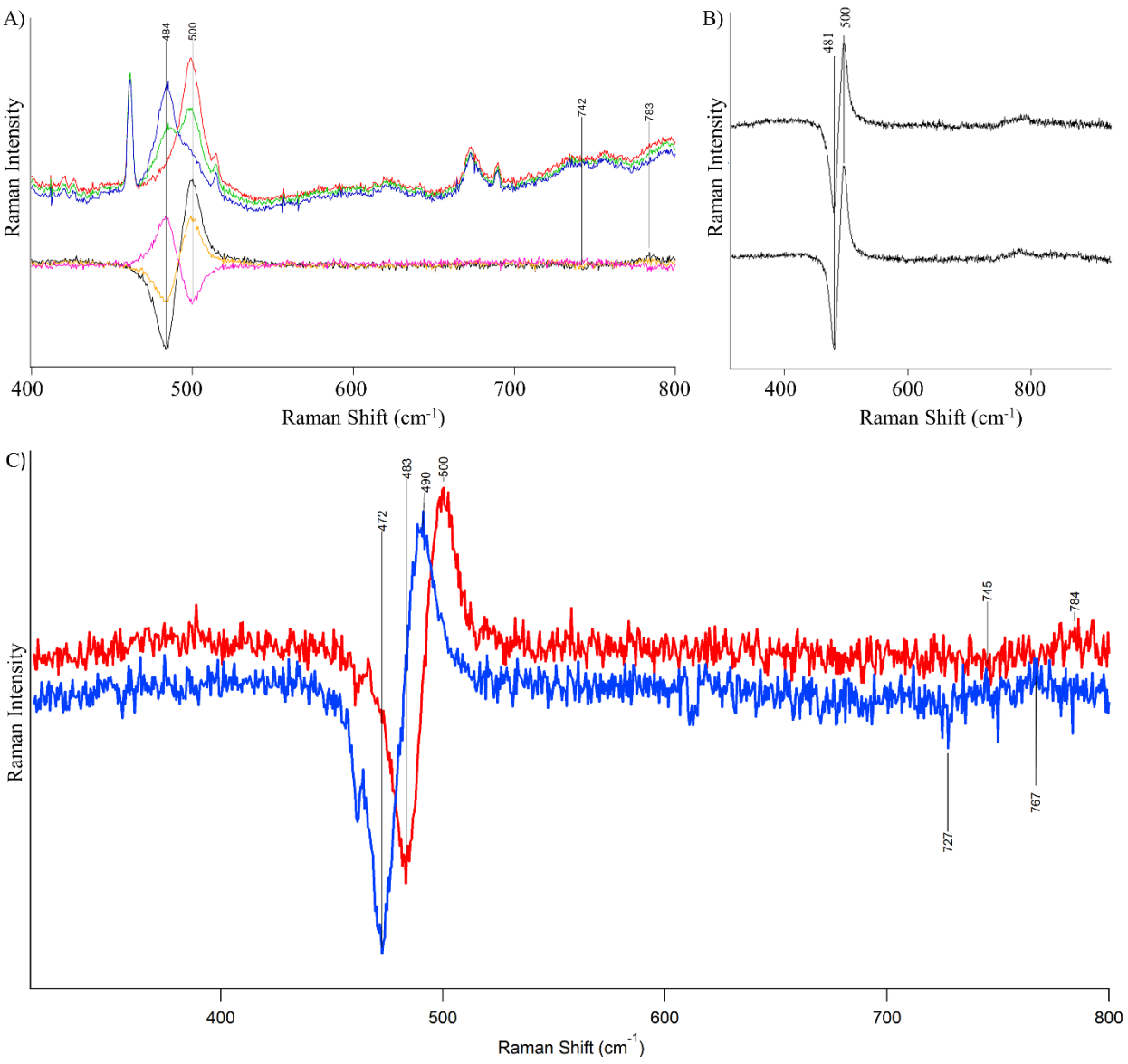

Figure 4.5: The effect of anaerobic chemical reduction and oxidation of UreA2B2 in $H_2{}^{18}O$ solvent in the presence or absence of substrate.(A) The resonance Raman absolute spectra of UreA2B2 redox cycled in $H_2{}^{16}O$ (red), 80% $H_2{}^{18}O$ (blue), or 40% $H_2{}^{18}O$ (green) in the absence of substrate. ^{18}O, Redox-exchange sensitive modes are displayed in a difference plot of $H_2{}^{16}O$ and 80% $H_2{}^{18}O$ (black trace), while the binding-mode of oxygen is displayed in the difference plots for $H_2{}^{16}O$ or 80% $H_2{}^{18}O$ and 40% $H_2{}^{18}O$ (yellow or magenta, respectively) (B) $H_2{}^{16}O/H_2{}^{18}O$ difference plot comparison of UreA2B2 redox cycled in the absence (top trace) or presence (bottom trace) of 60 mM urea. The samples containing urea were shown to have urease activity (data not shown). (C) The effect of urea on ^{16}O- or ^{18}O-bridged UreA2B2. A difference plot of UreA2B2 redox cycled in $H_2{}^{16}O$ versus $H_2{}^{18}O$ (red) is compared to similarly treated samples with 60 mM urea added following sample oxidation (blue).

Urea-Induced Shifts are not due to Chaotropic Effects in UreA2B2. The effects of urea on the resonance Raman spectrum of UreA2B2 were previously characterized (4), but that work did not address if the mode shifts observed were due to conformational changes arising from the denaturing effect of urea or to interaction with the metallocenter. To begin to address this question, samples of UreA2B2 with urea-induced mode shifts were dialyzed extensively into buffer lacking urea and analyzed again by resonance Raman spectrometry. The resonance Raman spectra for the samples were upshifted from 490 cm^{-1} to 500 cm^{-1} (Figure 4.6, red, blue, and green traces). Furthermore, samples of UreA2B2 were incubated with an equal concentration of the alternative chaotropic agent guanidinium chloride and subjected to similar analysis. The spectrum of this sample showed no shifts relative to untreated enzyme (Figure 4.6, black trace). Finally, two other urea-like molecules were examined for their effects on the (Fe-O-Fe) associated Raman shifts. These compounds were the known nickel-urease inhibitor, PPD, and the well-characterized nickel- and iron-urease inhibitor AHA. Overnight incubation of UreA2B2 with 2 mM PPD resulted in a downshift in the ν_s(Fe-O-Fe), while similar treatment with AHA showed no appreciable shifts in any of the metallocenter-associated vibrational modes (Figure 4.6, purple and yellow traces). Taken together, these results are consistent with the urea-induced shifts arising from a binding event at the metallocenter as opposed to chaotropic effects.

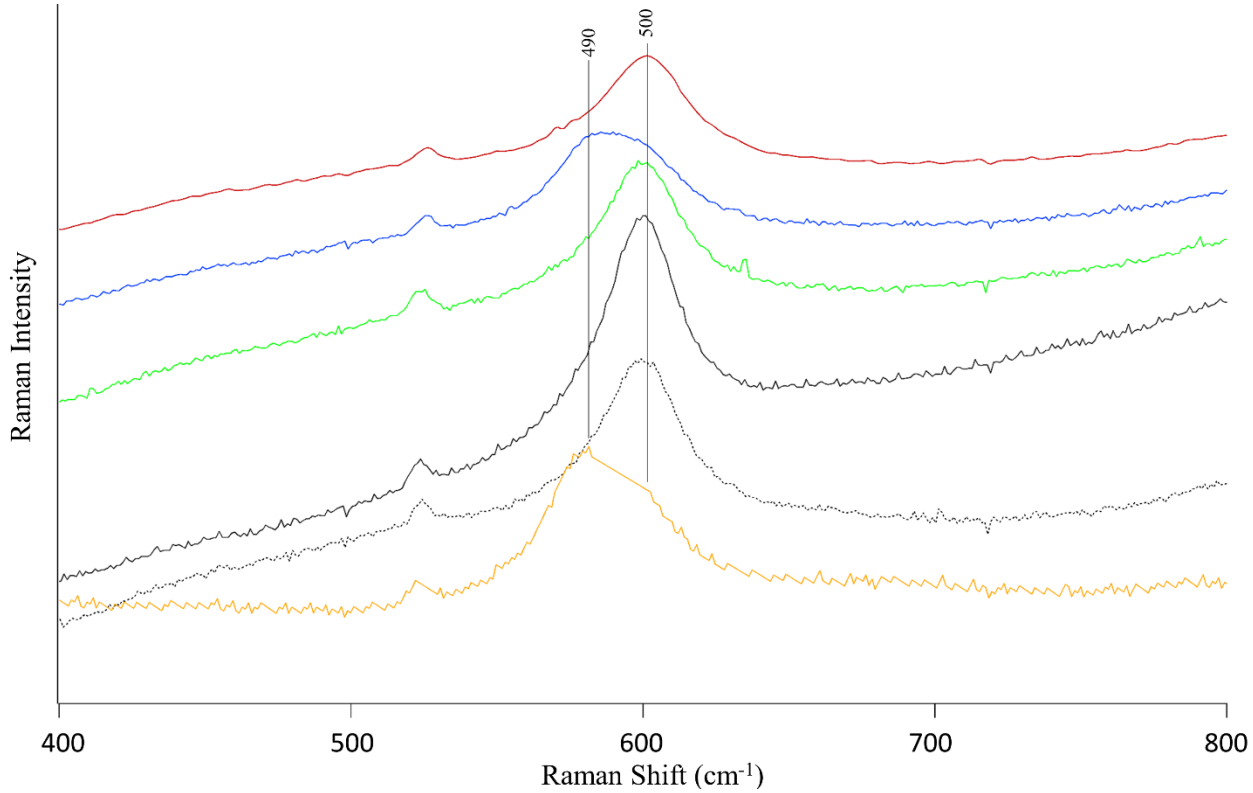

Figure 4.6. Examination of the basis for the urea-induced Raman shifts on UreA2B2. The absolute spectrum of UreA2B2 (red), after incubation with urea (blue), and when subjected to dialysis in buffer lacking substrate (green). The absolute spectrum of UreA2B2 treated with the chaotropic agent guanidinium chloride (black), the known UreA2B2 inhibitor AHA (black dotted), and the known urease inhibitor PPD (yellow).

The Effects of ^{15}N- and ^{18}O-Urea on the Resonance Raman Spectrum of UreA2B2.

To determine if the urea-sensitive modes are a result of direct coordination of the metallocenter to substrate, samples of UreA2B2 were incubated on ice with 60 mM unlabeled urea or ^{15}N-labeled urea for 3 h or with 60 mM ^{18}O-labeled urea for 5 h before being analyzed by resonance Raman spectroscopy. The absolute spectra of these samples all show a complete shift to the urea-bound mode of UreA2B2, with no detectable differences among the different isotopic forms of substrate, as illustrated in the double-difference plots (Figure 4.7).

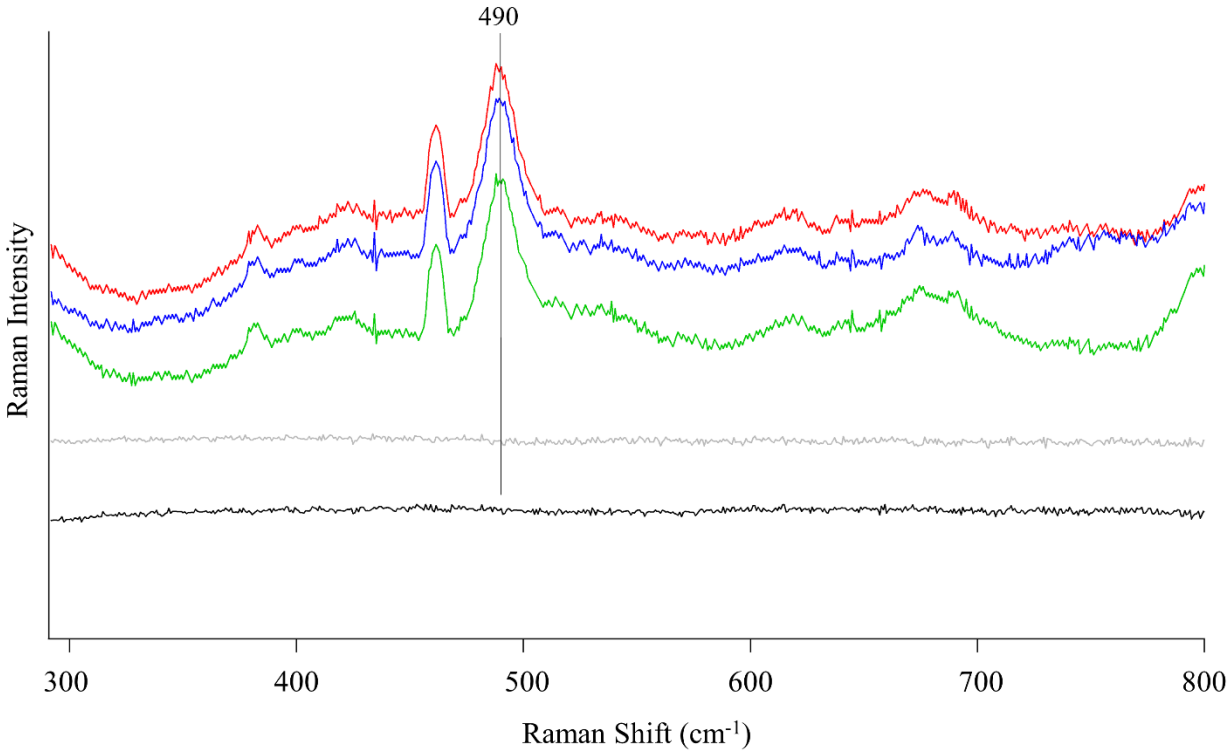

Figure 4.7: The effects of isotopically-labeled urea on the resonance Raman spectrum of UreA2B2. Samples of UreA2B2 were incubated overnight with 60 mM of unlabeled urea (red), ^{15}N-labeled urea (blue) or ^{18}O-labeled urea (green) and analyzed by resonance Raman spectroscopy. Difference spectra were used to highlight N-isotope sensitive modes (grey) and O-isotope sensitive modes (black).

Rapid Bulk Isotopic Solvent Exchange Provides Evidence of Terminal Solvent Modes in UreA2B2. To examine the effect of urea on the solvent isotope sensitive modes of UreA2B2, bulk solvent exchange studies were performed. Rapid D_2O or $H_2{}^{18}O$ exchange just prior to Raman analysis identified solvent proton- and oxygen-isotope sensitivities for UreA2B2 (Figure 4.8, top panels). These solvent-sensitive modes were upshifted in their relative positions by ~10 cm^{-1} in the presence of urea (Figure 4.8, bottom panels). Furthermore, comparison of the Raman spectra for ^{16}O-bridged and ^{18}O-bridged UreA2B2 in normal water versus D_2O resulted in no additional downshifts in the ν_s(Fe-O-Fe) (Figure 4.8, top panels, black traces), providing further evidence that this mode contains a bridging oxo group as opposed to a hydroxo group (Figure 4.8, bottom panels). The deuterium and oxygen sensitivities of the ~530 cm^{-1} to 511 cm^{-1}

downshift point to it being a stretching mode of terminal hydroxide coordinated to a ferric ion as hypothesized previously (4) and the existence of this terminal solvent precludes a substrate coordination scheme resulting in the displacement of both terminal solvent molecules in the oxidized metallocenter (3).

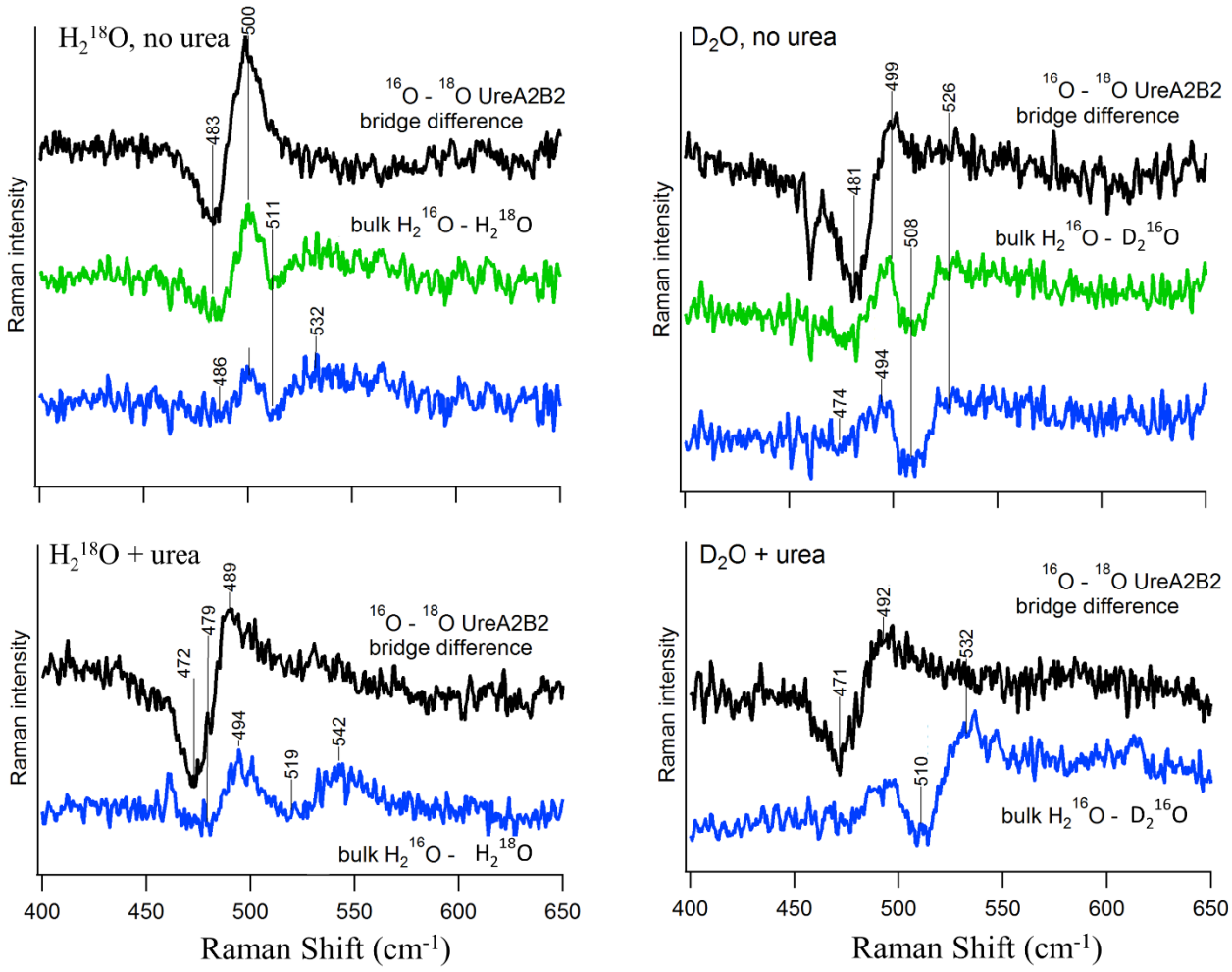

Figure 4.8: The effect of rapid bulk solvent exchange on ^{16}O- or ^{18}O-bridged UreA2B2 in the presence or absence of substrate. UreA2B2 was redox cycled in $H_2{}^{16}O$ or $H_2{}^{18}O$, diluted into 90% of $H_2{}^{18}O$ (left panels) or D_2O (right panels), incubated in the absence (top panels) or presence of 60 mM urea (bottom panels) and analyzed by resonance Raman spectroscopy. In all panels, the difference between the isotopic bridges (black) is compared to the difference between the bulk solvent-sensitive modes (blue). For the top panels, a trace showing the uncorrected bulk solvent difference is displayed for reference (green).

DISCUSSION

The studies presented here have furthered our understanding of the oxidized metallocenter of this unique urease. The pioneering studies on this enzyme highlighted several important properties (5), but the most intriguing finding was the solvent-exchange inert nature of the bridging oxo-species in the diferric metallocenter (4). In particular, it was surprising that that reduction of the enzyme, while successfully showing loss of the μ-oxo bridge chromophore by UV-vis spectroscopy, did not allow for exchange of the bridging oxo-group with bulk solvent. Here, we have shown that chemical reduction and oxidation in the presence of isotopic solvent does allow for the complete exchange of the bridging oxo-species in UreA2B2 independent of substrate turnover. It is difficult to explain why the previous studies did not observe oxygen-isotope solvent exchange by redox-cycling the enzyme, as reduction of the metallocenter was clearly observed in that work. In contrast to the former study, I used a chemical oxidant whereas the prior work used molecular oxygen for oxidation, but one expects to observe the isotopic shift in either case. Comparison of the $^{16}O/^{18}O$ Raman shifts for this enzyme and the μ-oxo bridged, diferric methemerythrin shows an identical wavenumber downshift (16). This result provides strong evidence that the oxidized state of the UreA2B2 metallocenter is indeed a μ-oxo bridge instead of a μ-hydroxo bridge. Additional evidence against a hydroxo bridging species comes from the difference spectra comparing ^{16}O- versus ^{18}O-bridged UreA2B2 which show no additional mode shifts when comparing enzyme in H_2O versus D_2O. Because the bridging oxygen exchanges with solvent when the enzyme is reduced, my initial plan to identify the nucleophilic water molecule by monitoring for loss of this atom during turnover was abandoned.

The metallocenter structures of urease from *K. aerogenes*, *H. pylori*, and *S. pasteurii* highlight a triad of water molecules positioned at the metallocenter, with one molecule serving as

a bridging water and two acting as terminal ligands to each nickel (3, 11, 12). Structures of AHA-bound urease from *H. pylori* (PDB 1E9Y) and diamidophosphate-bound urease from *S. pasteurii* (PDB 3UBP, where diamidophosphate derives from the slow enzymatic hydrolysis of PPD (1)) show that this solvent triad is displaced following inhibitor binding. I have shown that PPD, but not AHA, generates a downshift in the ν_s(Fe-O-Fe) mode equivalent in magnitude to the urea-induced downshift, even though it has been previously established that AHA is an inhibitor of UreA2B2 (5). The exchange-inert μ-oxo bridge of UreA2B2 precludes displacement of the bridging solvent molecule seen in both crystal structures, so it is still unclear how PPD, AHA, or urea, coordinate to the diferric site. Nevetheless, I hypothesize that the bulk-solvent sensitive modes, specifically the likely terminal Fe-OH mode at ~530 cm^{-1}, is absent in samples treated with either inhibitor. My results provide further evidence that the solvent-sensitive modes are from a terminal hydroxide and that urea coordination at the metallocenter alters their orientation, but does not lead to their displacement.

The surprising fast versus slow urea-binding phenotype of various UreA2B2 preparations caused me to examine my purification protocols in detail. However, no obvious deviations were noted when comparing my purification and handling protocols to the previously published work (4). I tested several hypotheses in an attempt to generate fast substrate-binding UreA2B2 from pEC015 expressing cells, including rapid sequential purification and freeze-thaw avoidance, but these adjustments did not produce fast substrate-binding UreA2B2. I also attempted to convert slow substrate-binding UreA2B2 into the fast substrate-binding UreA2B2 form by building on the hypothesis that a tight-binding inhibitor was present during purification. Though I could not identify a likely theoretical inhibitor that would be introduced during purification, I reasoned that displacement of the inhibitor with substrate followed by buffer exchange to remove both

inhibitor and substrate could change the phenotype. Unfortunately, application of this treatment on slow substrate-binding UreA2B2 did not result in an appreciable change in the rate of urea-induced downshifts. I propose additional tests to identify conditions for the generation of fast substrate-binding UreA2B2 in the concluding remarks of this dissertation.

The rapid bulk $H_2{}^{18}O$-solvent exchange studies presented in this work mirror the extensive $H_2{}^{18}O$-solvent exchange presented previously (4), with an observed trough at ~511 cm^{-1} and peak ~530 cm^{-1}. In this study, the effect of D_2O was more extensively characterized, with H_2O/D_2O difference plots showing a similar isotopic shift, with shifts comparable in position and magnitude. The exact position of these shifts is difficult to discern due to the relative weak intensity of these modes. However, the solvent oxygen- and proton-isotope sensitivity of this feature, its weak intensity, and its clear separation from the ν_s(Fe-O-Fe) mode support its assignment as a terminal solvent or hydroxide coordinated to the metallocenter. This assignment can be likened to the high pH Raman spectrum for horseradish peroxidase which arises from a terminal Fe-OH stretch (18). The peroxidase work identified this mode to be D_2O sensitive, but this sensitivity presented as an upshift, reasoned to be due to hydrogen bonding to a deprotonated His residue, which is precluded in UreA2B2. Deuterium exchange for Fe-OH stretches that are not participating in local hydrogen bonding are expected to result in downshifts of 20 cm^{-1} (13), similar to what is presented in my studies. The upshift of these features in the presence of urea could be caused by a slight displacement of the bound hydroxyl group on urea occupancy. This would present as an altered bond length or angle within the Fe-OH molecule, resulting in an upshift for both the $H_2{}^{18}O$ and D_2O sensitive shifts. The new mode at ~ 486 cm^{-1} following bridging oxo exchange with ^{18}O can be interpreted as a new Fe-OH bending mode as suggested

previously, however its overlap with the main ν_s(Fe-O-Fe) and weak intensity make its assignment difficult.

The reversibility of the urea-induced sensitivity in UreA2B2 and the lack of effect when using an alternative chaotropic agent were crucial for distinguishing if the resultant mode shifts were due to changes in the protein structure caused by a a denaturing effect or by substrate binding to the metallocenter. One could imagine that the urea-induced downshifts are due to local denaturation at the metallocenter, which could result in altered symmetric stretch angles of the Fe(III)-O-Fe(III) metallocenter and downshifts in the Raman spectrum. However, no denaturing effect would be expected from PPD treatment of UreA2B2, especially at the concentrations tested. This finding supports the hypothesis that urea coordination at the active site causes an altered orientation of the terminal solvent molecule, presumably bound at the non-substrate coordinating iron, which results in the observed Raman upshifts for the terminal water mode. In conclusion, strong evidence is presented in this work that the urea-induced mode shifts we observe for UreA2B2 are evidence of a binding-event at or near the metallocenter.

BIBLIOGRAPHY

BIBLIOGRAPHY

1. **Andrews, R. K., Dexter, A., Blakeley, R. L., and Zerner, B.** 1986. Jack bean urease (Ec 3.5.1.5) .8. on the inhibition of urease by amides and esters of phosphoric-acid. J. Am. Chem. Soc. **108**: 7124-7125.

2. **Balasubramanian, A., and Ponnuraj, K.** 2010. Crystal structure of the first plant urease from jack bean: 83 years of journey from its first crystal to molecular structure. J. Mol. Biol. **400**: 274-283.

3. **Benini, S., Rypniewski, W. R., Wilson, K. S., Miletti, S., Ciurli, S., and Mangani, S.** 1999. A new proposal for urease mechanism based on the crystal structures of the native and inhibited enzyme from *Bacillus pasteurii*: why urea hydrolysis costs two nickels. Structure **7**: 205-216.

4. **Carter, E. L., Proshlyakov, D. A., and Hausinger, R. P.** 2012. Apoprotein isolation and activation, and vibrational structure of the *Helicobacter mustelae* iron urease. J. Inorg. Biochem. **111**: 195-202.

5. **Carter, E. L., Tronrud, D. E., Taber, S. R., Karplus, P. A., and Hausinger, R. P.** 2011. Iron-containing urease in a pathogenic bacterium. Proc. Natl. Acad. Sci. U.S.A. **108**: 13095-13099.

6. **Cox, G. M., Mukherjee, J., Cole, G. T., Casadevall, A., and Perfect, J. R.** 2000. Urease as a virulence factor in experimental cryptococcosis. Infect. Immun. **68**: 443-448.

7. **Dixon, N. E., Gazzola, T. C., Blakeley, R. L., and Zermer, B.** 1975. Letter: Jack bean urease (EC 3.5.1.5). A metalloenzyme. A simple biological role for nickel? J. Am. Chem. Soc. **97**: 4131-4133.

8. **Duff, L. L., Klippenstein, G. L., Shriver, D. F., and Klotz, I. M.** 1981. Multiple conformations at functional site of hemerythrin: Evidence from resonance Raman spectra. Proc. Natl. Acad. Sci. U.S.A. **78**: 4138-4140.

9. **Eaton, K. A., Brooks, C. L., Morgan, D. R., and Krakowka, S.** 1991. Essential role of urease in pathogenesis of gastritis induced by *Helicobacter pylori* in gnotobiotic piglets. Infect. Immun. **59**: 2470-2475.

10. **Farrugia, M. A., Macomber, L., and Hausinger, R. P.** 2013. Biosynthesis of the urease metallocenter. J. Biol. Chem. **288**: 13178-13185.

11. **Ha, N. C., Oh, S. T., Sung, J. Y., Cha, K. A., Lee, M. H., and Oh, B. H.** 2001. Supramolecular assembly and acid resistance of *Helicobacter pylori* urease. Nat. Struct. Biol. **8**: 505-509.

12. **Jabri, E., Carr, M. B., Hausinger, R. P., and Karplus, P. A.** 1995. The crystal structure of urease from *Klebsiella aerogenes*. Science **268**: 998-1004.

13. **Loehr, T. M., and Plane, R. A.** 1968. Raman spectra and structures of arsenious acid and arsenites in aqueous solution. J. Inorg. Chem. **7**: 1708-1714.

14. **Mobley, H. L., Island, M. D., and Hausinger, R. P.** 1995. Molecular biology of microbial ureases. Microbiol. Rev. **59**: 451-480.

15. **Rees, T. A., and Bekheet, I. A.** 1982. The role of nickel in urea assimilation by algae. Planta **156**: 385-387.

16. **Shiemke, A. K., Loehr, T. M., Sanders-Loehr, J.** 1984. Resonance Raman study of the μ-oxo-bridged binuclear iron center in oxyhemerythrin. J. Am. Chem. Soc. **106**: 4951-4956.

17. **Sirko, A., and Brodzik, R.** 2000. Plant ureases: roles and regulation. Acta Biochim. Pol. **47**: 1189-1195.

18. **Sitter, A. J., Shifflett, J. R., and Terner, J.** 1988. Resonance Raman spectroscopic evidence for heme iron-hydroxide ligation in peroxidase alkaline forms. J. Biol. Chem. **263**: 13032-13038.

19. **Sjoberg, B. M., Loehr, T. M., and Sanders-Loehr, J.** 1982. Raman spectral evidence for a μ-oxo bridge in the binuclear iron center of ribonucleotide reductase. Biochemistry **21**: 96-102.

20. **Stoof, J., Breijer, S., Pot, R. G., van der Neut, D., Kuipers, E. J., Kusters, J. G., and van Vliet, A. H.** 2008. Inverse nickel-responsive regulation of two urease enzymes in the gastric pathogen *Helicobacter mustelae*. Environ. Microbiol. **10**: 2586-2597.

21. **Witte, C. P.** 2011. Urea metabolism in plants. Plant Sci. **180**: 431-438.

CHAPTER 5

Additional Studies

This chapter summarizes a series of disparate studies of both the *Klebsiella aerogenes* urease components and the *Helicobacter mustelae* UreA2B2 iron-containing urease. These investigations do not fit well into the earlier chapters, but they include a few novel findings that are worth recording to assist in future studies of these systems.

ADDITIONAL *K. aerogenes* UREASE STUDIES

Equilibrium Dialysis Studies of MBP-UreDFG Using Nickel. Prior studies had reported that UreG and MBP-UreD bind nickel (0.5 and 2 Ni atoms per protomer, respectively) (1 ,6), raising questions of whether these sites are retained and whether additional sites exist in MBP-UreDFG. To assess the nickel-binding capacity of this complex, I dialyzed 200 µl samples of MBP-UreDFG (20 µM) in 50 mM Tris buffer, pH 7.4, containing 25 mM NaCl against buffer containing varied concentrations of $NiCl_2 \cdot 6H_2O$ (12.5, 25, 50, 100, 200, 400, 800 or 1600 µM) overnight at 4 °C. I determined nickel concentrations for both the dialysis buffer and the dialyzed protein by colorimetric assay using the metal-binding probe 4-(2-pyridylazo) resorcinol (Figure 5.1). Experimental samples were compared against a nickel standard curve.

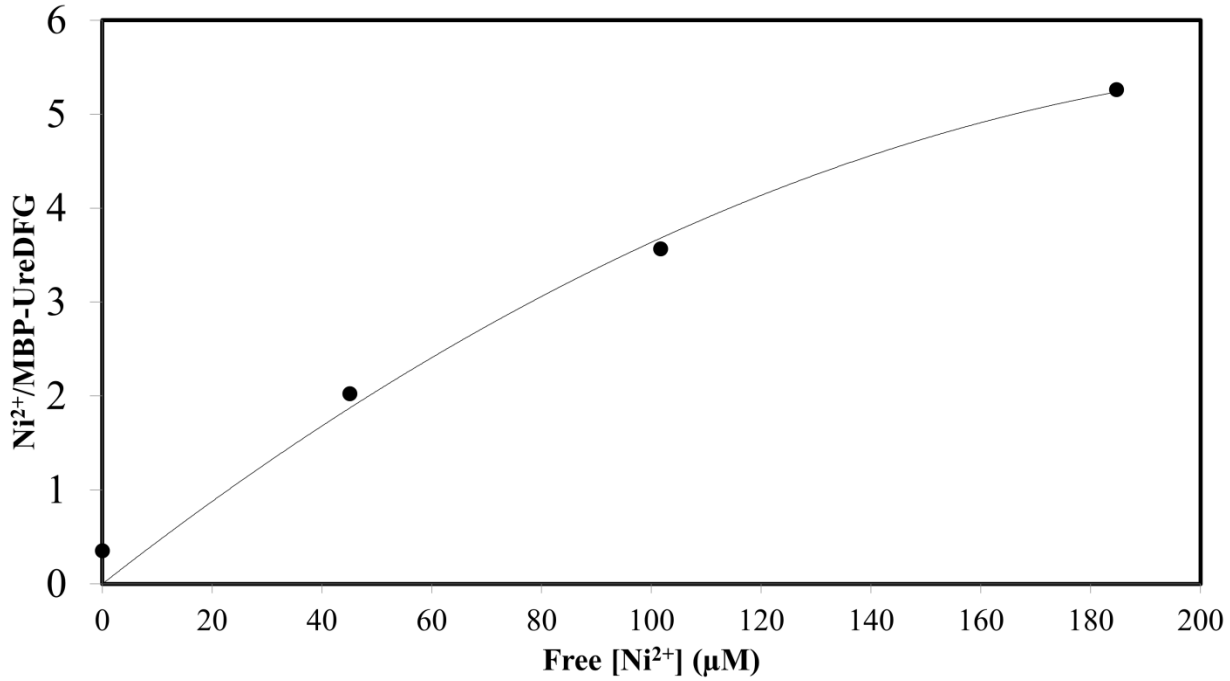

Figure 5.1: Nickel binding to MBP-UreDFG as determined by equilibrium dialysis. Ni^{2+} per MBP-UreDFG was determined by subtraction of [Ni^{2+}] in the dialysis tubing from [Ni^{2+}] in the protein sample, divided by the concentration of protein.

The results show that increasing nickel concentrations led to increasing numbers of nickel atoms weakly bound to MBP-UreDFG that seemed to approach a plateau; however, additional replicates would be required to be able to report binding constants. Furthermore, the data are somewhat compromised because protein samples experienced significant precipitation above 400 µM Ni^{2+}. A preliminary conclusion from these data is that MBP-UreDFG bound greater numbers of nickel atoms than expected for the separate MBP-UreD and UreG components, consistent with nickel binding to UreF when present in the complex or to new binding sites being exposed or created within the complex compared to the individual proteins. If these studies are repeated by others, it may be informative to extend the analysis by addition of GTP/Mg^{2+} to determine if these ligands have an effect on nickel binding to this complex.

Effects of Urease Activation Conditions on MBP-UreDFG Stability. The MBP-UreDFG complex provided me with a platform to study the stability of the accessory protein

complex when subjected to various conditions in the presence or absence of urease. The accessory proteins are known to exist as a complex separate from urease (20) and activation of urease results in dissociation of the accessory proteins from the structural subunits (22), but it is unknown if the accessory proteins dissociate from one another during this process or dissociate as a unit. To examine the protein:protein interactions of the accessory proteins under urease activation conditions, I incubated MBP-UreDFG and the MBP-UreDFG:urease apoprotein complex in buffers containing one or more of the following components: 100 µM $NiCl_2 \cdot 6H_2O$, 100 mM sodium bicarbonate, and 400 µM Li·GTP plus 800 µM $MgCl_2$. These treated samples were studied for their protein:protein interactions using an amylose-affinity resin pull-down approach (Figure 5.2).

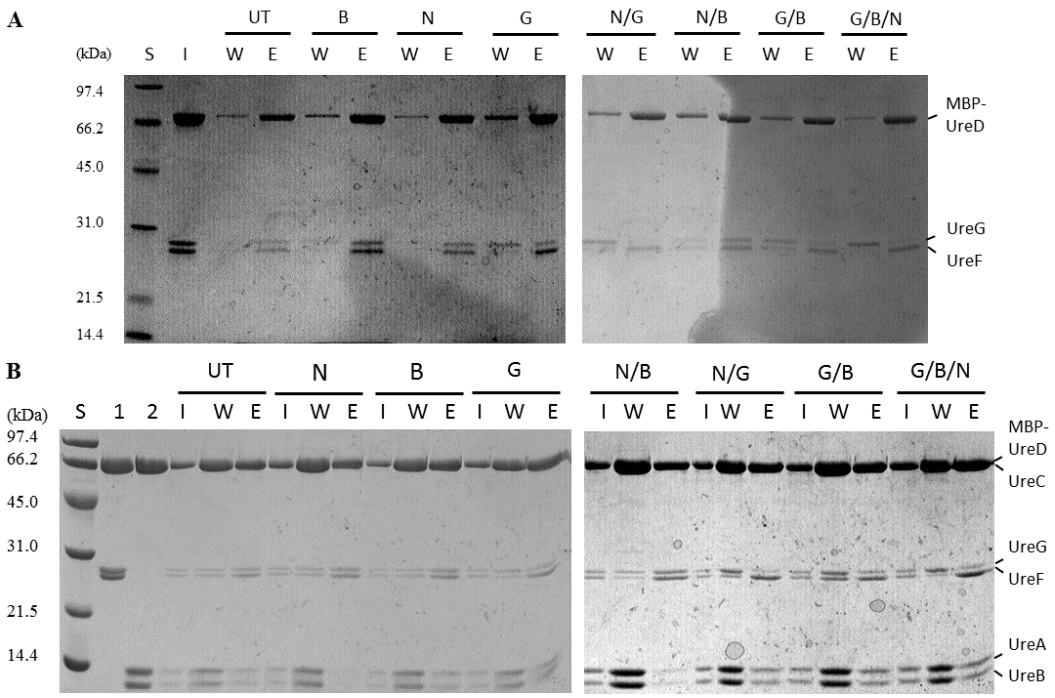

Figure 5.2: The effects of urease activation components on the stability of MBP-UreDFG and MBP-UreD:urease apoprotein. (A) Samples of 3 µM MBP-UreDFG were incubated in buffer alone (untreated, UT) or buffer containing one or more of 100 mM sodium bicarbonate (B), 100 µM $NiCl_2 \cdot 6\ H_2O$ (N), and 400 µM Li·GTP plus 800 µM $MgCl_2$ (G), and subjected to amylose affinity chromatography. Samples of the reactions prior to chromatography (input, I), the first wash step (W) and the final elution (E) with 10 mM maltose are displayed. (B) Samples of MBP-UreDFG incubated with UreABC apoprotein were treated and chromatographed as described above. Additional lanes: untreated MBP-UreDFG (1); untreated UreABC apoprotein (2), protein standard (S).

As shown in Figure 5.2A, MBP-UreDFG formed a stable complex that elutes from amylose resin with very little protein lost during the wash step when using the untreated sample. This association was at least partially lost in all samples containing GTP/Mg^{2+}, as evidenced by the appearance of the UreG band in the wash fractions and the loss of intensity of the UreG band in the elution fractions. This loss seemed to be enhanced when nickel was present, as is evident when comparing the fractions from GTP/Mg^{2+}/Ni^{2+} and GTP/Mg^{2+}/Ni^{2+}/bicarbonate samples to the GTP/Mg^{2+}/bicarbonate sample. These results fit well with what was discovered in the *Helicobacter pylori* urease system (16). That study reported the ejection of UreG from a soluble

UreH:UreF:UreG complex in a GTP-dependent manner, with UreG dissociation enhanced by the presence of Ni^{2+}.

In Figure 5.2B, I present similar experiments using the complex of MBP-UreDFG with urease. Again, the untreated sample is stable to the chromatographic step and elutes as an intact complex with maltose. In contrast to what was observed for MBP-UreDFG in panel A, the MBP-UreDFG:urease apoprotein complex was unaffected by GTP alone, but dissociated to urease and MBP-UreDFG in the presence of Ni^{2+} or Ni^{2+}/bicarbonate. For the case of Ni^{2+}/bicarbonate/Mg^{2+}/GTP, the data are consistent with initial release of MBP-UreDFG and subsequent UreG dissociation, but the sequence of steps was not tested in this study. The nickel-dependent dissociation of urease from the initial complex cannot be related to the active-site metal ion occupancy of urease because in Chapter 2 I demonstrated that MBP-UreDFG forms a stable interaction with urease holoprotein *in vitro*. Rather, I propose that added nickel binds to one or more sites on the MBP-UreDFG complex or on urease (other than at the urease catalytic center) to cause a physical change in the quaternary state that leads to dissociation of urease.

The GTP-dependent dissociation of UreG from MBP-UreDFG raised the question of the quaternary state of the released UreG. It is well established that *K. aerogenes* UreG purifies as a monomer that is not affected by added nickel or GTP (1, 20), whereas nickel-loaded, GTP-bound, *H. pylori* UreG exists as a dimer (16). To examine the quaternary state of UreG released from GTP-treated MBP-UreDFG, I incubated 60 µM protein complex for one h at room temperature in 50 mM Tris buffer, pH 7.4, containing 150 mM NaCl or with the same buffer supplemented with GTP/Mg^{2+}, GTP/Mg^{2+}/Ni^{2+}, or GTP/Mg^{2+}/Ni^{2+}/bicarbonate in concentrations equivalent to those listed above. The samples were analyzed using a 100 ml Sephadex-200 gel filtration column pre-equilibrated in 50 mM Tris buffer, pH 7.4, containing 150 mM NaCl, and

eluted in the same buffer (Figure 5.3A). Fractions corresponding to elution peaks were pooled, concentrated 50-fold, and analyzed by sodium dodecyl sulfate-polyacrylamide gel electrophoresis (SDS-PAGE) (Figure 5.3B).

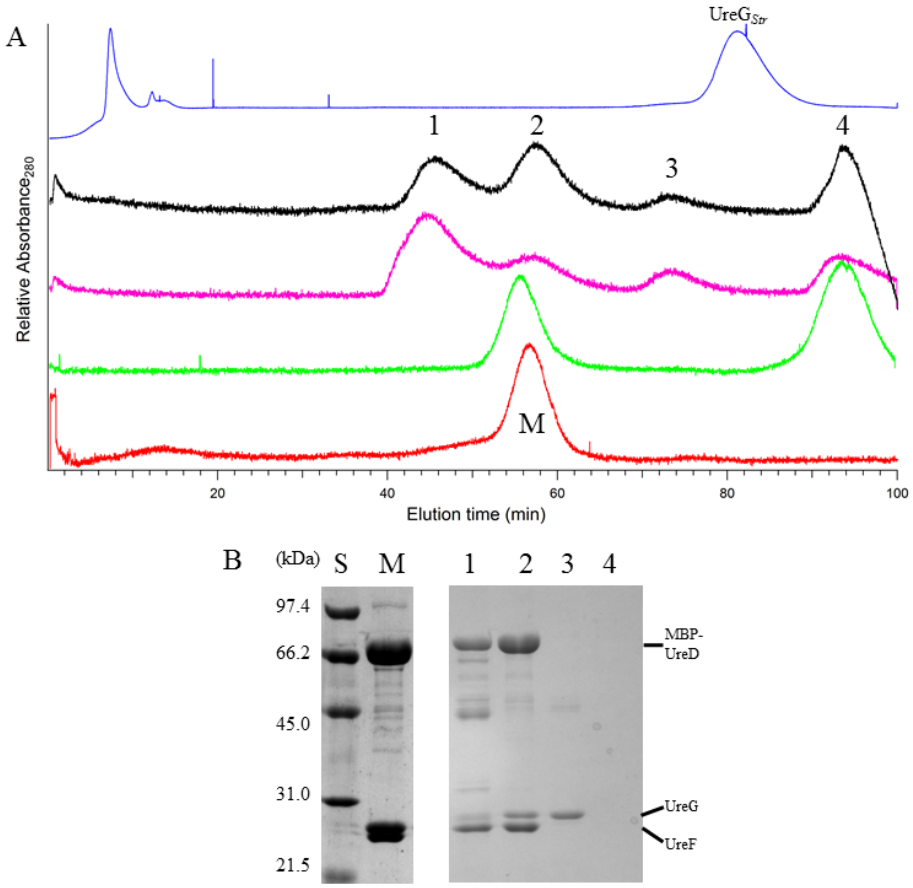

Figure 5.3: Size-exclusion chromatography of MBP-UreDFG exposed to various activation conditions. (A) Size-exclusion chromatographs of MBP-UreDFG samples incubated in 50 mM Tris buffer alone (red trace) or buffer supplemented with GTP/Mg^{2+} (green), GTP/Mg^{2+}/Ni^{2+} (magenta) or GTP/Mg^{2+}/Ni^{2+}/bicarbonate (black). A sample of purified UreG$_{Str}$ (blue trace) is included as a reference. (B) A representative SDS-PAGE gel containing the labeled fractions from the trace above. Untreated MBP-UreDFG (lane M) is compared against peaks 1-4 in the treated samples. Protein standards are located in lane S.

As illustrated above, treatment of MBP-UreDFG with buffers containing combinations of GTP and nickel resulted in the decomposition of (MBP-UreDFG)$_2$ into two species: dissociated UreG (Figure 5.3B, lane 3) and a species approximated by ((MBP-UreDF)$_2$:UreG$_x$)$_y$ (Figure 5.3B, lane 1; where 'x' was clearly substoichiometric and 'y' was not determined). A third

species eluted at roughly the same time as untreated MBP-UreDFG (Figure 5.3B, lane 2) and contained all of the subunits, likely representing unaffected complex. Comparison of the elution time for the dissociated UreG versus purified $UreG_{Str}$ (Figure 5.3A, blue trace) to the elution positions of standard proteins yields estimated sizes of 50 kDa for dissociated UreG and 27 kDa for $UreG_{Str,}$ which suggests that UreG is ejected from the MBP-UreDFG complex as a dimer. An incomplete ejection of UreG is observed in peak 1 of the GTP- and nickel-treated samples (Figure 5.3, black and magenta traces). Whereas UreG dissociation from the *H. pylori* complex provided the monomeric protein in the presence of bicarbonate (16), I observed no difference in the elution profiles when comparing GTP/Mg^{2+}/Ni^{2} treatments in the presence or absence of bicarbonate (Figure 5.3A, black and magenta traces). Perhaps of significance, my elution buffers lacked GTP, Mg^{2+}, Ni^{2+}, or bicarbonate, so a more complete study could examine the effects of these buffer components on the chromatographic behavior. Interestingly, the ejection of UreG generated a larger complex with an approximate molecular weight of 880 kDa. A prior study reported a large oligomeric complex for purified MBP-UreD via size-exclusion chromatography, and the authors hypothesized this was caused by associations among the MBP-tags (6). My results can be explained similarly, although further experiments with differentially tagged complexes would help to address this issue. As a final comment, the fourth species observed at the end of the elution with an estimated size of less than 5 kDa was not due to GTP as shown by analysis of GTP-containing buffer. The identity of this peak is still in question.

Interactions Between MBP-UreDFG and UreE. Previous studies identified both a complex containing urease apoprotein, $UreDFG_{Str}$, and UreE (according to SDS-PAGE analyses of *Strep*-tactin pull-down fractions) and a UreG:UreE interaction that was observed *in vitro* in the presence of nickel and zinc (1). These findings raised the questions of whether UreE also

interacts with MBP-UreDFG and whether the presence of divalent metals affects this interaction. To answer these questions, I incubated samples of MBP-UreDFG and His144*UreE (a truncated UreE missing its *C*-terminal 15 residues) in 50 mM Tris buffer, pH 7.4, containing 25 mM NaCl or the same Tris buffer supplemented with 100 µM $ZnCl_2$ or 100 µM $NiCl_2 \cdot 6H_2O$. After 30 min on ice, the mixtures were incubated with 50 µl of amylose resin (pre-equilibrated in the Tris buffer) and placed at room temperature with mixing for an additional hour. The resin was washed several times with 250 µl of the same buffer and eluted in 100 µl of Tris buffer containing 10 mM maltose. Samples from each step in treatment were analyzed by SDS-PAGE (Figure 5.4).

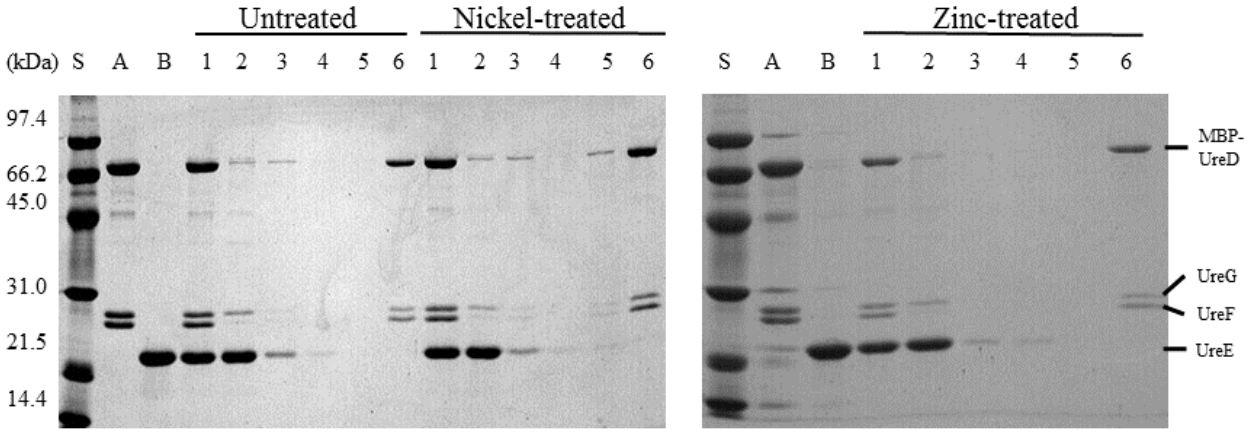

Figure 5.4: The effects of nickel and zinc on MBP-UreDFG:UreE interactions. MBP-UreDFG (2 µM) was incubated with 10 µM UreE for one hour on ice in 50 mM Tris buffer, pH 7.4, and 25 mM NaCl (Untreated). This buffer was supplemented with 100 µM of $NiCl_2 \cdot 6H_2O$ (Nickel-treated) or 100 µM $ZnCl_2$ (Zinc-treated). The lanes include: S, protein standards; A, MBP-UreDFG; B, H144*UreE; 1, amylose-resin inputs; 2-5, wash fractions; 1-4; 6, maltose elutions.

The above study shows that UreE eluted in the wash step regardless of treatment conditions, and it did not form a complex with MBP-UreDFG. The results also revealed a slight dissociation of UreG from the MBP-UreDFG complex, with the ejection of UreG being unaffected by the presence of divalent metals. The lack of binding between UreE and the

complex is somewhat surprising given the prior findings and this result may be attributed to steric interference by the MBP fusion tag; e.g., it could be reasoned that MBP obstructs the UreE:UreG interfacial site. However, this conclusion is weakened by recent work suggesting that UreE and UreF interact at the same site on UreG (19). To circumvent any concern about interference by MBP, an alternative tag could be used; however, solubility of UreDFG is an issue for complexes not containing the MBP-UreD fusion protein. It is also possible that the results are skewed because it relies on pull-down of MBP-UreD; a confirmatory experiment could be carried out using *Strep*-II tagged UreG in the complex or placing this tag on UreE. I would not recommend using the natural affinity of UreE for Ni-NTA resin because this requires the confounding presence of nickel for elution in the chromatographic step.

Crystallization Attempts on MBP-UreDFG and UreABC:UreD. Although the crystal structure of the UreH:UreF:UreG complex from *H. pylori* is known (15, 16), the many distinctions between that urease system and the one from *K. aerogenes* made it desirable to subject MBP-UreDFG to crystallization trials. I purified samples of MBP-UreDFG using a modified protocol (14). In particular, I used Q-Sepharose resin in place of DEAE-Sepharose for the second chromatographic step, while retaining the same elution protocol. Following size-exclusion chromatography, I analyzed fractions containing MBP-UreDFG for their purity by SDS-PAGE, pooled and concentrated them to 1 ml, and incubated the sample on ice for 3 days. To ensure the complex was maintained during this time-frame, I subjected the pooled concentrate to size-exclusion chromatography a second time and examined it for purity (Figure 5.5).

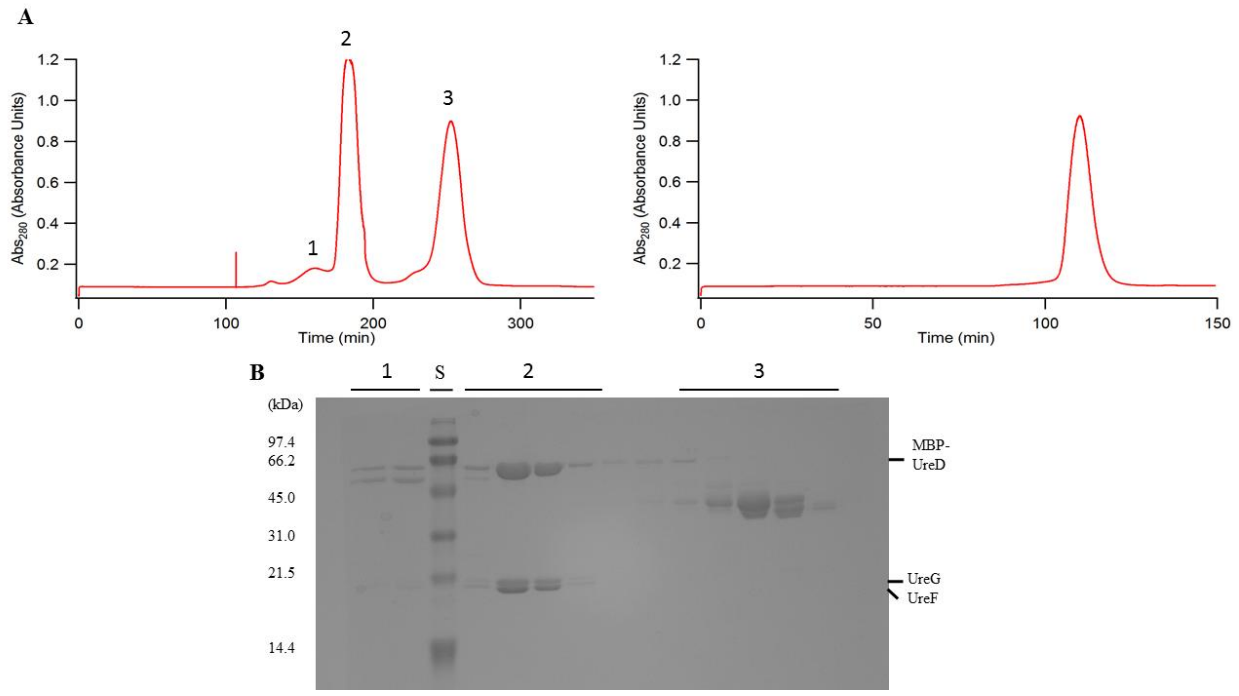

Figure 5.5: Size-exclusion chromatography of MBP-UreDFG. (A) MBP-UreDFG samples were purified by amylose and Q-Sepharose resins prior to being concentrated and chromatographed on Sephadex-200 size exclusion resin. The chromatographs using for the first (left) and second (right) Sephadex-200 separations are displayed. (B) SDS-PAGE analysis of the fractions from each of the labeled elution peaks above (1-3) compared to protein standards (S).

The MBP-UreDFG complex was stable over the short time-span examined and eluted as a single species off the Sephadex-200 resin. My studies from Chapter 2 demonstrated that MBP-UreDFG exists solely as a stable dimer of the hetero-trimeric species in the absence of the urease structural subunits. I have noted dissociation of UreG from the MBP-UreDFG complex for samples that were thawed for longer time-periods (weeks), but in collaboration with crystallographer Dr. Jian Hu (Michigan State University), we concluded this complex was a viable candidate for initial protein crystallographic screening.

Samples of MBP-UreDFG purified as described above were concentrated to 8 mg/ml and exchanged into 5 mM Tris buffer, pH 7.4, containing 1 mM β-mercaptoethanol, 1 mM EDTA, and 12.5 mM NaCl. Crystal screens used a Mosquito robot (TPPlabtech. Cambridge, MA) and

Wizard™ Classic (1 and 2, as well as 3 and 4), and the Hampton™ Salt, Crystal Screen, Index, and PEG 96-well crystal screen trays. Samples were prepared by the sitting-drop method, stored at 21 °C for four months, and checked on a semi-weekly basis for crystal formation. Unfortunately, I observed no crystals during this timeframe. Previous MBP-UreDFG purifications yielded stable protein at concentrations of 38 mg/ml, so future crystal trials could examine greater concentrations of MBP-UreDFG to see if that change facilitates crystal formation.

A crystal structure of the UreABC:UreD complex also was desired. The mutagenesis studies of UreD in Chapter 3 of this dissertation provided evidence for a buried water tunnel that plays a role in metal transfer into urease, and a structure could demonstrate the existence of such a channel. While biochemical and structural studies have given us some information on how UreD interacts with urease (8, 23, 24), the structure could directly establish how UreD interacts with urease apoprotein -- especially related to the nascent active site. To this end, I purified UreABC:UreD apoprotein from nickel-depleted *E. coli* cells expressing pKK17, which encodes the entire *K. aerogenes* urease gene cluster (*ureDABCEFG*). I determined that purification of UreABC:UreD:UreF:UreG by weak anion exchange, strong anion exchange, and size-exclusion chromatography yielded a fraction containing UreABC:UreD at high purity. The key to this process is the size-exclusion procedure, as I found that use of a low flow rate (0.3 ml/min) over a long column (100 ml bed volume) allowed for optimal separation of the various contaminating protein complexes. I subjected a sample of this complex at 12 mg/ml to crystallization conditions in the same manner as for MBP-UreDFG, but using only the Wizard™ Classic (1 and 2, or 3 and 4) trays. I observed various morphologies of crystal formation after 2 weeks, as listed in Table 5.1.

Table 5.1: Crystal morphology and buffer conditions used in production of crystals from solutions of UreABC:UreD.

Crystal morphology	Buffer conditions[a]
Wizard Classic 1 and 2	
Thin/long	35% MPD, 160 mM imidazole, 100 mM HCl, 200 mM $MgCl_2$, pH 8.0
Oval/large	20% PEG 3K, 100 mM sodium citrate, 100 mM citric acid, pH 5.5
Small/cubic	20% PEG 3K MME, 100 mM Tris HCl, pH 7.0
Star-like	20 % PEG 1K, 100 mM imidazole/HCl, 200 mM calcium citrate, pH 8.0
Star-like	10% PEG 3K, 100 mM H_2KPO_4/Na_2HPO_4, pH 6.2
Thin/long	10% PEG 8K 100 mM imidazole/HCl, 200 mM calcium acetate, pH 8.0
Large/irregular	30% PEG 3K, 100 mM Tris base/HCl, 200 mM NaCl, pH 7.0
Large/cubic	10% PEG 8K, 100 mM KH_2PO_4/Na_2HPO_4, 200 mM NaCl, pH 6.2
Medium/cubic	1260 mM ammonia acetate, 100 mM HEPES/NaOH, pH 7.5
Thin/long	10% PEG 3K, 100 mM sodium cacodylate/HCl, pH 6.5
Wizard Classic 3 and 4	
Thin/long	8% PEG 4K, 100 mM sodium acetate/HCl, 200 mM $CaCl_2$, pH 4.6
Star-like	28% PEG 400, 100 mM HEPES/NaOH, 200 mM $CaCl_2$, pH 7.5
Thin/long	20% PEG100K, 100 mM HEPES/NaOH, pH 7.5
Cubic/medium	5% PEG 1K, 100 mM Na_2HPO_4/Citric acid, pH 4.2
Star-like	50% PEG 200, 100 mM sodium cacodylate/HCl, 200 mM $MgCl_2$, pH 6.5
Star-like	40% PEG 200, 100 mM sodium cacodylate/HCl, 200 mM calcium acetate, pH 6.5
Star-like	25% PEG 1500, 100 mM SPG, pH 8.5
Oval/large	30% PEG 2K MME, 150 mM potassium bromide

Table 5.1 (cont'd):

Cubic/small	10% PEG 2K MME, 100 mM sodium acetate/acetic acid, 200 mM ammonium sulfate, pH 5.5
Cubic/small	20% PEG 3350, 100 mM sodium citrate/citric acid, 200 mM sodium citrate tribasic, pH 4.0
Star-like	100 mM Bis-Tris propane/HCl, 200 mM sodium malonate dibasic, pH 8.5

[a]Abbreviations used: MPD = 2-Methyl-2,4-pentanediol, PEG = polyethylene glycol, MME = monomethyl ether, SPG = succinic acid/phosphate/glycine.

While the observation of multiple successful crystallization conditions was an exciting finding, optimization will be required for two reasons. First, the identity of the proteins within these crystals needs to be ascertained, since dissociation of UreD could result in crystallization of free urease. A test for this would be to dissolve a large crystal of putative UreABC:UreD sample and analyze it by SDS-PAGE. The presence of bands corresponding to UreD and the urease subunits would confirm the crystal indeed contained UreD docked to urease. Second, the size and number of crystals generated was insufficient for X-ray scattering studies that are required for structure determination. Dr. Hu suggested that the buffer conditions could be optimized by hand, and this could be a future endeavor. Furthermore, it could be helpful to obtain a higher yield of UreABC:UreD by using a published protocol involving cells with a plasmid expressing only *ureDABC* and containing a second copy of *ureD* (21). My initial efforts with this approach failed to yield enhanced levels of the complex, but this direction is worth further investigation. Overall, crystallization efforts have great potential and appear to be poised to yield exciting information on how the accessory proteins dock to urease.

Native PAGE Analysis of Urease Apoprotein and Its Complexes with MBP-UreDFG. I was interested in identifying the relative protein stoichiometries of assembly complexes between urease and MBP-UreDFG as a precursor to the work presented in Chapter 2.

As a first step, I prepared mixtures of UreABC apoprotein and MBP-UreDFG in 50 mM Tris, pH 7.4, 1 mM EDTA, and 1 mM β-mercaptoethanol buffer containing 25 mM NaCl. The samples were incubated for 30 min at room temperature before being analyzed by blue native PAGE on precast 3-12% Bis-Tris acrylamide gels (GE Healthcare) (Figure 5.6).

A

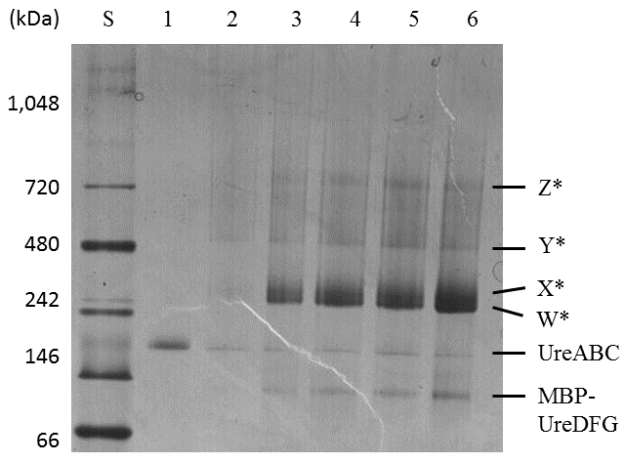

B

Band ID	Molecular weight (kDa)	Hypothetical stoichiometry	Mass difference (ΔkDa)
MBP-UreDFG	113.25	MBP-UreDFG	6.8
UreABC	247.4	$(UreABC)_3$	1.9
W*	367	$(UreABC)_3$:MBP-UreDFG	2.3
X*	390.5	$(UreABC)_3$:(MBP-UreDFG):UreG	0.8
Y*	559	$(UreABC)_3$:$(MBP\text{-}UreDF)_2$:MBP-UreDFG	6.5
Z*	732.5	$((UreABC)_3)_2$:$(MBP\text{-}UreDFG)_2$	6.4

Figure 5.6: Blue native PAGE analysis of UreABC and UreABC:MBP-UreDFG complexes. (A) Mixtures of UreABC apoprotein and MBP-UreDFG were subjected to blue native PAGE analysis. UreABC (1 µM) was incubated in the absence (lane 1) or the presence of 1, 2, 3, 4 or 5 µM MBP-UreDFG (lanes 2-6). NativeMark protein standards (lane S) were used to estimate the molecular masses of the complexes observed. (B) Band migration analysis of protein species observed in A. Band distances and molecular weights were calculated using Alphaview software on an Alphaimage HP gel scanning apparatus (Protein Simple). Bands W and X are two closely migrating species.

The two lowest molecular weight bands observed on the gel fit well with the theoretical masses of MBP-UreDFG and $(UreABC)_3$. No band was observed for $(MBP\text{-}UreDFG)_2$, but the MBP-UreDFG was not examined in isolation as a comparison. It is possible that the complex exists as a heterotrimer when subjected to the electrophoretic conditions even though ion mobility mass spectrometry (IM-MS) and size-exclusion chromatography findings presented in Chapter 2 demonstrate MBP-UreDFG exists in solution as a stable dimer. Four additional bands were observed when UreABC was incubated with increasing amounts of MBP-UreDFG (bands W-Z, above). An approximate molecular mass for each band was determined by using band

migration analysis and gave evidence of an $(UreABC)_3$:MBP-UreDFG complex (band W). This result is in good agreement with the published findings in Chapter 2 of this work. Assignments of $(UreABC)_3$:(MBP-UreDFG):UreG, $(UreABC)_3$:$(MBP\text{-}UreDF)_2$:(MBP-UreDFG), and $((UreABC)_3)_2$:$(MBP\text{-}UreDFG)_2$ for bands X, Y and Z, respectively, fit well with the experimental molecular weights determined in this study, but these structures are highly tentative. Although neither complex X or Y was observed in our IM-MS study, the prior work showed the urease complexes are complex in their compositions. Complex Z was observed in the earlier study, and I speculate that it derives from two urease trimer-of-trimers bridged by a single $(MBP\text{-}UreDFG)_2$ unit. Finally, I note that while MBP-UreDFG was added in increasing amounts, only bands W and X increased in intensity, with no apparent increase in free MBP-UreDFG or the appearance of a band corresponding to $(MBP\text{-}UreDFG)_2$. Overall, this study provides additional evidence that $(MBP\text{-}UreDFG)_2$ interacts with urease as a monomer of heterotrimers *in vitro* and provides new information on novel complexes formed between urease and the soluble accessory protein complex under non-activating conditions.

Stability of MBP-UreDFG Following Tag Removal. Proteolytic removal of MBP from MBP-UreD was previously shown to result in protein precipitation and an inability to recover free UreD from anion exchange chromatography (5). In analogous studies, I tested whether free UreD:UreF:UreG could be liberated from the complex containing the MBP tag and whether the sample is stable and soluble. Thus, I digested 1.3 mg of MBP-UreDFG with 0.04 mg of factor Xa in 20 mM Tris buffer, pH 8.0, containing 100 mM NaCl and 2 mM $CaCl_2$. After 3 h at room temperature, I analyzed the digested samples by SDS-PAGE (Figure 5.7). The results clearly demonstrate the successful cleavage of the linker between the MBP and UreD domains of MBP-UreD. In an extension of this approach, I attempted to separate the digestion products by size-

exclusion chromatography, but no protein elution peaks were observed at the expected positions (data not shown). This result could have been a consequence of the low protein concentrations I used in this experiment, but on the basis of prior studies with UreD (5) and UreD:UreF:UreG (20) I attribute the protein loss to protein aggregation on the resin. Thus, I conclude that UreD:UreF:UreG is unstable when liberated from its solubility tag. Future extensions of these studies could include use of detergent-containing buffers in an effort to retain solubility of the accessory proteins. The resulting sample might be useful for future GTPase activity studies by UreG or for crystallization studies of the UreD:UreF:UreG complex.

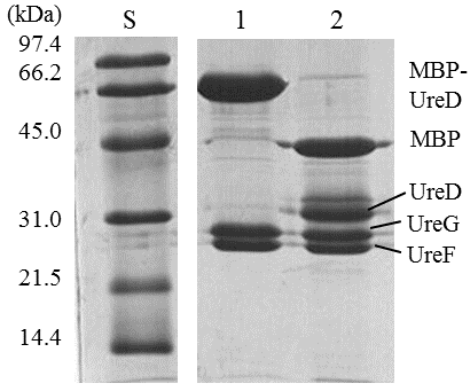

Figure 5.7: Factor Xa cleavage of MBP-UreDFG. Lane S depicts protein standards. Samples of MBP-UreDFG were incubated three h at room temperature in calcium-containing buffer that lacked (lane 1) or contained (lane 2) 3% w/w factor Xa.

Metal-Catalyzed Oxidation of H144*UreE and MBP-UreDFG. Previous studies that attempted to probe the metal-binding residues of *K. aerogenes* UreD focused on targeting residues for mutagenesis, but that process was made difficult by the relatively poor sequence homology with *H. pylori* UreH and no side chain ligands were identified (5). In Chapter 3, I expanded the alignment parameters to include 30 additional UreD homologs, but this effort also left the identity of metal ligands unclear. Here, I describe my attempts to probe for metal-coordinating residues by applying the metal-catalyzed oxidation (MCO) labeling technique (2). This method uses Fenton-like chemistry to generate reactive oxygen species that are localized

near the coordinated metal ions and has been successfully used in conjunction with mass spectrometry to probe for metal-coordinating sites on angiotensin I, bacitracin A (2), copper-zinc superoxide dismutase (3), and the prion protein (25). As a proof-of-concept, I chose to use this technique on the well-characterized nickel-metallochaperone H144*UreE (9). This truncated protein has two distinct metal-binding sites: one is found at the interfacial site of the homodimer with the metal coordinated by using His96 from each protomer, and a second site at the periphery of each protomer that uses His110 and His112 for metal binding (17). Samples of H144*UreE (100 µM) were incubated for one h at room temperature in 50 mM Tris buffer, pH 7.4, containing 85 mM NaCl or the same buffer supplemented with 10 mM of ascorbate and/or 1 mM of persulfate in a final volume of 20 µl. To test for metal-dependent oxidation, I added 100 µM of $NiCl_2 \cdot 6H_2O$, $CuSO_4$, or $(NH_4)_2Fe(SO_4)_2 \cdot 6H_2O$ to samples, treated them with ascorbate and persulfate, and incubated the mixtures for one h at room temperature. I adjusted each sample to pH 2.0 with glacial acetic acid and digested overnight at 37 °C with 1 µg of gastric porcine pepsin. I dried the digests in a speed-vac/SC110A centrifuge (Savant), resuspended them in water containing 0.1 % trifluoroacetic acid and 2 % LC-MS grade acetonitrile (Sigma), desalted using C-18 desalting tips (Thermo Scientific), and diluted 1:1 with α-cinnamic acid matrix. I used 1 µl of these dilutions for analysis by MALDI-TOF MS (Figure 5.8).

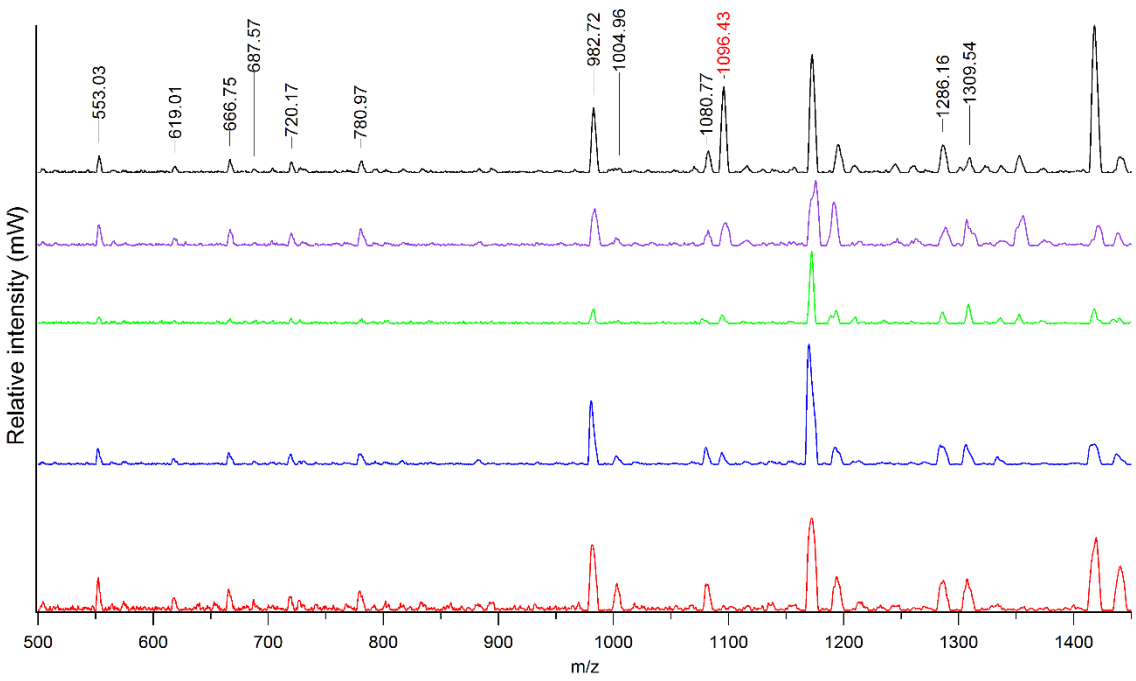

Figure 5.8: Mass spectra of pepsin digests from MCO-treated or untreated H144*UreE. Pepsin digests are shown for H144*UreE that was incubated in buffer lacking (red trace) or containing (blue trace) 1 mM ascorbate and 10 mM ammonium persulfate. Also shown for comparison are digests of protein incubated with the reductant/oxidant supplemented buffer containing Cu^{2+} (green trace), Ni^{2+} (purple trace), or Fe^{2+} (black trace). Peaks identified by theoretical digest: 553.05 *m/z* (residues 44-48), 619.01 *m/z* (residues 119-123), 666.75 *m/z* (residues 43-48, 1 missed cut), 687.57 *m/z* (residues 131-136), 720.17 *m/z* (residues 131-136, two oxidation events), 780.97 *m/z* (residues 43-49, 2 missed cuts), 982.72 *m/z* (residues 131-139, three missed cuts), 1004.96 *m/z* (residues 131-139, three missed cuts, 1 Na^{+}), 1080.77 *m/z* (residues 107-114, 1 missed cut), 1096.43 *m/z* (residues 107-114, 1 missed cut, 1 oxidation event), 1286.16 *m/z* (residues 91-101, 2 missed cuts), and 1309.54 *m/z* (residues 89-99, 2 missed cuts).

The above results identified a novel peak (*m/z* of 1096) that was consistent with oxidation of the H144*UreE pepsin fragment 107-114, which contains the characterized UreE metal-binding site, following treatment of the protein with reductant/oxidant which is enhanced in intensity when this treatment includes Cu^{2+}, Ni^{2+}, or Fe^{2+}. The MCO effect is most notable in the presence of ferrous ions, a highly effective reagent for Fenton chemistry (Figure 5.8, black trace). Overall, this proof-of-concept study confirmed that redox treatment of the

metallochaperone UreE in the presence of various divalent metals selectively oxidized a specific UreE pepsin fragment that is known to contain a well characterized metal binding site.

I extended the MCO approach to studies of MBP-UreD, MBP-UreDFG, and UreG. I examined both pepsin and trypsin digests, and I varied the ascorbate (0.1, 1 or 10 mM) and persulfate (0.1, 1 or 10 mM) concentrations. Treated and untreated samples were separated by SDS-PAGE, the bands corresponding to the individual protein subunits were excised and digested in-gel by trypsin as described previously (14), or with 1 mg of porcine pepsin in 10 µl of 100 mM ammonium bicarbonate, pH 2.0. Peptide fragments were extracted and analyzed by MALDI-TOF MS as described previously (14); however, no novel peaks were noted in any subunit for any condition tested when comparing metal-treated samples to untreated samples. The low affinity for nickel seen in the equilibrium dialysis study described in this chapter may account for the lack of metal-catalyzed oxidation in the MBP-UreDFG sample, but this result does not account for the absence of an oxidation peak in the MBP-UreD and UreG samples, as each protein has been shown to have relatively high affinity for nickel (1, 6).

Negative Stain Electron Microscopy of Urease:Accessory Protein Complexes. One of the biggest remaining questions regarding urease activation is where the accessory proteins dock to the enzyme. Previous small angle X-ray scattering and chemical cross-linking/mass spectrometry studies provided evidence that UreD interacts with both UreB and UreC, where the interaction was localized near the vertices of $(UreABC)_3$ (8, 23). Further structural studies on accessory protein-bound urease complexes were needed to solidify this docking assignment. To this end, I began a collaboration with Dr. Kristin Parent (Michigan State University) to study urease and urease:accessory protein complexes by negative stain electron microscopy. The small size of the urease complexes precluded the use of the more sensitive cryo-electron microscopy,

but I hypothesized that by comparing ensemble images of accessory-protein unbound and bound samples of urease we could determine more accurately how UreD was oriented on the enzyme. Furthermore, comparison to UreABC:UreD:UreF:UreG could provide us with information on how the distal accessory proteins orient themselves when docked to the enzyme, which would provide crucial information regarding whether the accessory proteins adopt a different conformation relative to that seen in the $(UreH:UreF:UreG)_2$ structure from *H. pylori* (16). To this end, I spotted 3 µl of a 0.2 mg/ml of UreABC, UreABC:UreD, UreABC:UreD:UreF or UreABC:MBP-UreD:UreF:UreG complexes onto a carbon grid and allowed the samples to dry. Excess protein not adsorbed to the grid was washed away with deionized water and the gridded protein was stained with 0.5% phosphotungstic acid. This stain is atypical in its use in modern electron microscopy, as it tends to give a dark, intense background. However, the more standard stains were found to cause decomposition of the protein complexes. Grids were scanned on a JEOL 2200-FS electron microscope. An ensemble image of particles resembling the expected triangular shape of urease was prepared and compared to the crystal structure (Figure 5.9). Overall, the averaged ensemble image overlays well with the crystal structure, providing us with a baseline with which to compare accessory protein-docked urease complexes.

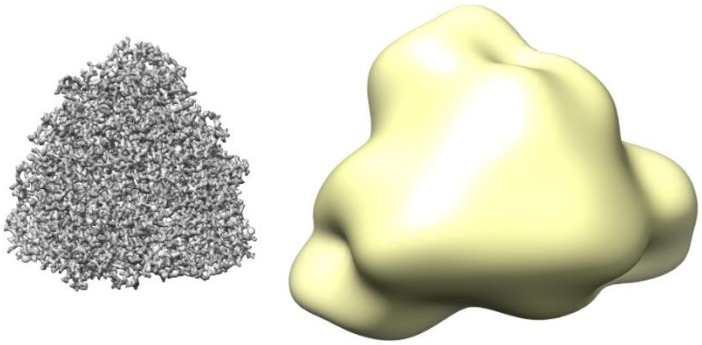

Figure 5.9: General shape comparison of the structures of *K. aerogenes* urease obtained by X-ray crystallography (left (18)) and negative-stain electron microscopy (right).

Unfortunately, similar studies on samples of $(UreABC)_3$ docked with UreD, MBP-UreD:UreF:UreG, or UreD:UreF yielded grid images that lacked particle homogeneity. In general, these complexes presented a large amount of background particles that were smaller in size compared to urease itself. The most peculiar finding was an absence of urease-like particles in most grids scanned. This result may be explained by a loss of stability of $(UreABC)_3$ when accessory protein are docked and in the presence of the dye; however, the UreABC:MBP-UreD:UreF:UreG complex was stable under standard conditions by IM-MS (14). Several experimental adjustments can be used in attempts to rectify these problems. For example, the sample could be stabilized for accessory protein-docked urease by chemical cross-linking. Samples of UreABC:UreD or complexes with additional accessory proteins could be treated with the various cross-linkers as previously described (8), separated by Blue-Native PAGE, and bands corresponding to $(UreABC)_3$:$(accessory\ protein)_x$ could be extracted, purified and analyzed by negative-stain electron microscopy as described above. I hypothesize the Blue native PAGE would enrich for specific accessory protein-docked urease species, and the cross-linking would help with stabilization of the enzyme.

ADDITIONAL UreA2B2 STUDIES

Additional Spectroscopic Studies of UreA2B2. While ample evidence has been presented supporting a diferrous active site in active UreA2B2 and a μ-oxo bridged, diferric center in oxidized UreA2B2, both in this dissertation and in founding studies on the enzyme (7), it was unclear whether a mixed-valent (Fe(II)/Fe(III)) state was accessible. To this end, I collaborated with Dr. Roman Davydov (Northwestern University) to attempt the generation of mixed-valent UreA2B2 by radiolytic reduction under low temperature (frozen) conditions. Significantly, electron paramagnetic resonance (EPR) spectra of mixed-valent species can

discern between a μ-oxo and μ-hydroxo bridge in the starting diferric centers of enzymes or synthetic inorganic complexes (10, 11, 12, 13). For example, mixed-valent di-iron centers generated by radiolytic reduction of μ-oxo bridged diferric enzymes yield EPR spectra that possess low anisotropy ($\Delta g \sim 0.1$) and exhibit an average *g*-value near 1.9 at 77 K, whereas samples that are warmed (annealed) briefly following cryoreduction either exhibit EPR spectra with no change in these values or they have increased anisotropy and a decrease in average *g*-value (12). Most tellingly, similar studies with μ-hydroxo bridged species lead to spectra exhibiting higher anisotropy ($\Delta g \sim 0.2$) and a lower average *g*-value (~ 1.8) at 77 K, with no change in these values after annealing.

Using samples that I provided, Dr. Davydov observed that radiolytic cryoreduction of UreA2B2 produced small quantities of the mixed-valent state that exhibited EPR spectral features at 77 K indicative of a μ-oxo bridged diferric state for the starting sample, with *g*-values of 1.945, 1.9 and 1.84 (Figure 5.10). These values did not change after annealing at temperatures of 155 and 173 K. Overall, this study gives further evidence that UreA2B2 possesses a μ-oxo bridged, diferric center in its oxidized state.

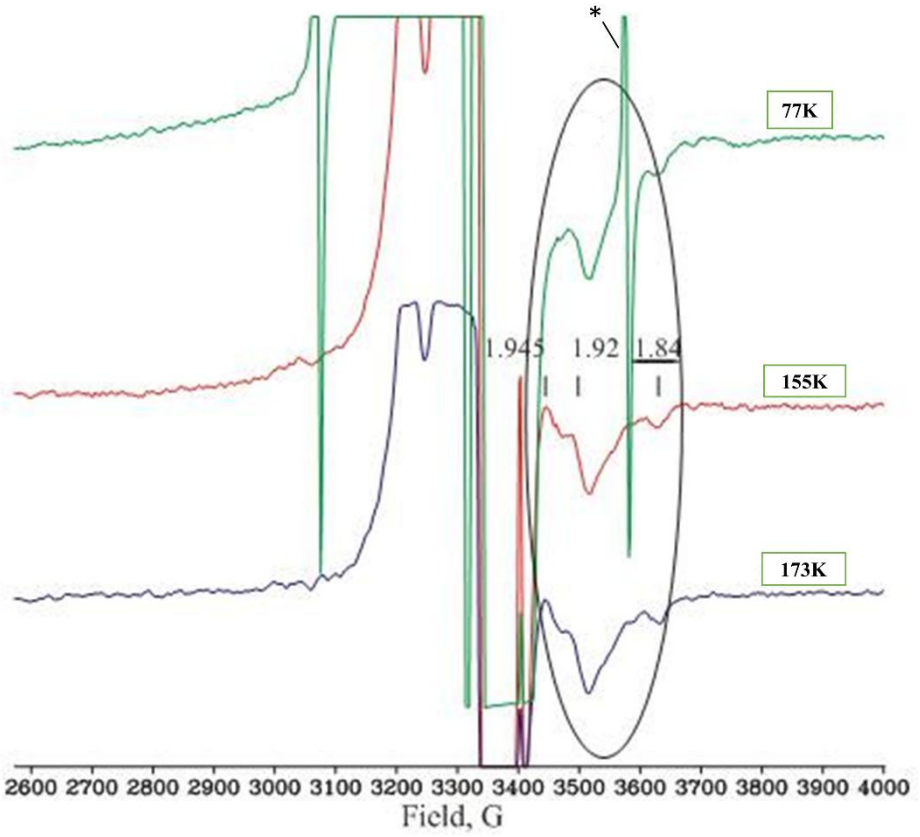

Figure 5.10: **EPR studies of UreA2B2 subjected to radiolytic reduction.** Samples of UreA2B2 were reduced by γ-radiation at 77 K and analyzed by EPR spectroscopy at 77 K (green trace) without additional treatment or after brief annealing at 155 K (red trace) or 173 K (blue trace). The feature noted by (*) at 77 K is a hydrogen-specific feature generated from irradiation of the sample holder and does not originate from sample. This figure was generously provided by Dr. Davydov (Northwestern University).

I also continued a collaboration initiated by Dr. Eric Carter with the laboratory of Dr. Edward Solomon (Stanford University) to study the dithionite-reduced state of UreA2B2 by circular dichroism (CD), magnetic circular dichroism (MCD), and variable-temperature, variable-field magnetic circular dichroism (VTVH MCD) spectroscopic methods. The diferrous state was assumed to possess a μ-hydroxo bridging mode, mirroring the situation that is thought to exist in the nickel enzyme. This weakly electronically coupled site should be poorly observable by MCD spectroscopy. As background, prior EPR studies of the fully reduced, anaerobic form of UreA2B2 showed it to be EPR-silent when using the conventional

perpendicular mode instrument as expected for two ferrous ions. Parallel mode EPR is capable of showing a signal near g ~ 16 arising from a coupled diferrous center, but such studies were not conducted.

Our initial MCD studies of reduced UreA2B2 highlighted strong MCD features at low-temperatures, with these features decreasing as temperature increased (Figure 5.11). These results provide evidence against a μ-hydroxo bridge in the fully reduced state and could suggest a bridging water molecule. Preliminary pH and deuterium-sensitivity studies were performed by analyzing reduced UreA2B2 at buffer pDs of 7.4, 8.4, and 9.4. The results (not illustrated) showed no change in the observed features by either CD or MCD spectroscopy. A μ-hydroxo bridged site would be expected to show sensitivity to bulk deuterium, thus giving further evidence against a (Fe(II)-OH-Fe(II)) site. Rather, these findings also support a μ-aqua bridge which would result in a loss of coupling between the ferrous ions. Preliminary VTVH MCD studies were carried out (not shown) and appear to identify these same strong features associated with weak J-coupling. Therefore, these studies provide evidence that the resting-state of UreA2B2 is that of a diferrous, μ-aqua bridged active site.

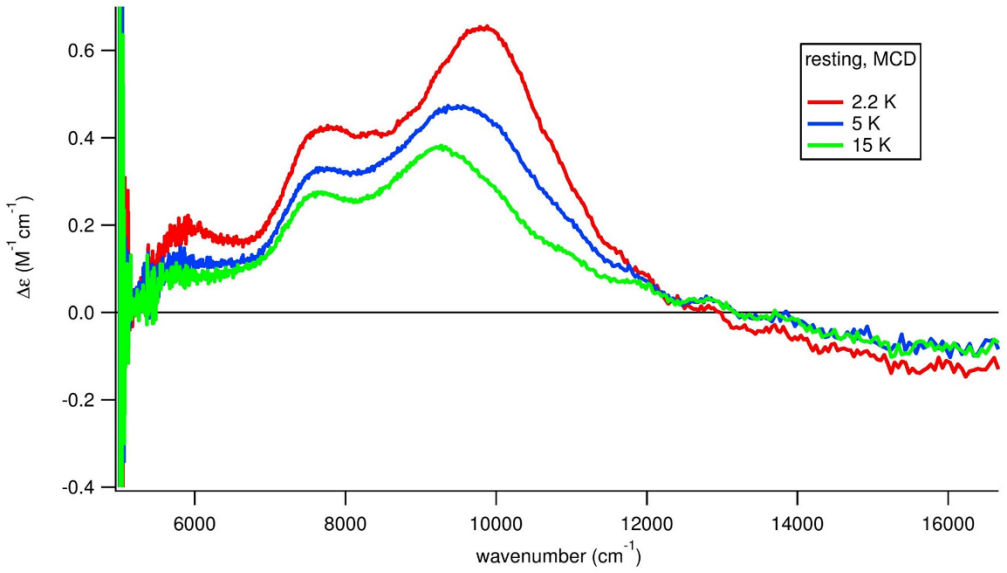

Figure 5.11: Low temperature MCD spectra of anaerobic, dithionite reduced UreA2B2. Changes in molar absorptivity were observed at 2.2 K (red trace), 5 K (blue trace), and 15 K (green trace). This figure was prepared and generously provided by Lars Boettger from the lab of Edward Solomon (Stanford University).

The effect of the nickel urease inhibitor boric acid (4) on the CD and MCD spectra of UreA2B2 was examined to gain further insights into the electronic coupling of the two metals at the metallocenter with a bound substrate analog. The preliminary results show differences between reduced UreA2B2 with or without boric acid (not shown), but additional studies need to be carried out. I've provided additional samples to the Solomon group and further analyses are planned in the near future.

Boric Acid Inhibition of UreA2B2. Although boric acid inhibition of nickel urease has been kinetically analyzed (4), the kinetic inhibition properties of this compound with the iron enzyme were unknown. Our collaboration with Dr. Solomon to investigate the electronic properties of the borate-inhibited enzyme necessitated kinetic characterization of the inhibitor mechanism and thermodynamics. To this end, I assayed for the mode and kinetics of inhibition for boric acid under anaerobic reducing conditions. UreA2B2 in 50 mM HEPES, 1 mM EDTA, pH 7.8, buffer was made anaerobic by injecting it into a 10 ml argon-filled vial using an argon-

purged gas-tight syringe (Hamilton) and allowing gas exchange to occur overnight on ice. Powders of ferrous sulfate and boric acid were made anaerobic with 3 vacuum/argon purge cycles at 2 min per step using a Schlenk line. A 50 mM HEPES, 150 mM NaCl, pH 7.8, assay buffer was made anaerobic with 5 vacuum/argon purge cycles at 10 min per step. Enzyme stop solution containing 5% phenol and 0.025% sodium nitroprusside was made anaerobic in a similar manner. All samples were transferred into a 100% N_2 chamber maintained at < 4 ppm O_2. Reaction tubes containing 0, 0.6, 2, 6, 20 or 60 mM boric acid and 2, 6, 20, 60, 200 or 600 mM urea were prepared in 50 mM HEPES, 150 mM NaCl, pH 7.8, buffer. UreA2B2 was diluted to 0.8 µg/ml and reduced with 1 mM of ferrous sulfate over 2 h at room temperature. Following this process, standard urease assay conditions were performed (27), but using anaerobic conditions. A plot of the specific activities versus substrate concentrations is depicted in Figure 5.12. The calculated K_m^{app} and V_{max}^{app} values are displayed in Table 5.3.

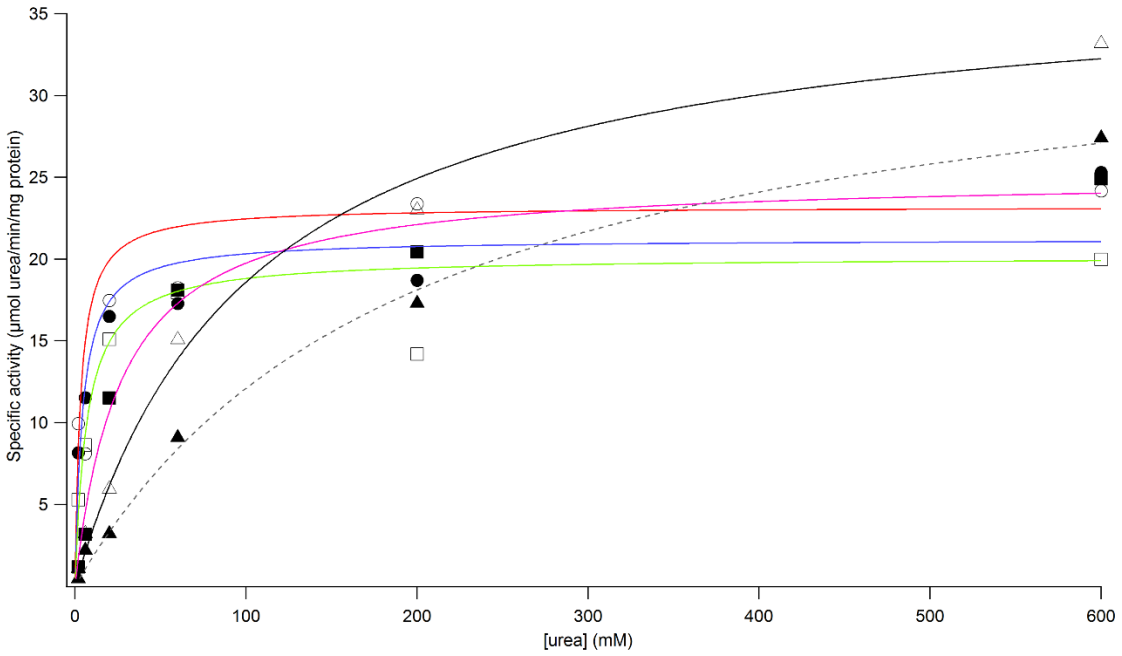

Figure 5.12: Kinetic analysis for boric acid inhibition of UreA2B2. Urease assays were performed anaerobically after prior reduction of the enzyme in solutions lacking (open circles, red trace) or containing boric acid at 0.6 (closed circles, blue trace), 2 (open square, green trace), 6 (closed square, magenta trace), 20 (open triangle, black line) or 60 mM (closed triangle) concentrations and the substrate concentrations indicated.

Table 5.3: Apparent K_m and V_{max} for UreA2B2 in various concentrations of boric acid.

[Boric acid] (mM)	K_m^{app} (mM)	V_{max}^{app} (µmol urea degraded ··min^{-1}·· mg $protein^{-1}$)
0	3.3	23.2
0.6	4.4	21.22
2	6.98	20.13
6	27.09	25.11
20	103.2	37.8
60	197.4	36

The data presented here represent a single study, so caution must be exercised when attempting to interpret the results. Nevertheless, the results are generally consistent with competitive inhibition (K_i ~ 1.23 ± 0.25 mM; the increased activity at the largest urea concentrations for 20 and 60 mM borate may be aberrant) which is an order of magnitude smaller than for the nickel enzyme from *K. aerogenes* (26). Also of interest, these reduction and reaction conditions yielded greater UreA2B2 activities than what was published previously (2 U/mg activity) (7). This result likely is due to the alternate reductant that I used, however, it is also possible that the enzyme sample utilized in this study differed from that used previously (e.g., see the evidence for two enzyme forms described in Chapter 4).

Resonance Raman Spectroscopy on UreA2B2 with Increasing Amounts of Urea. In order to determine the necessary amount of urea to add to UreA2B2 to generate a complete downshift in the ν_s(Fe(III)-O-Fe(III)) mode, resonance Raman spectra were obtained from samples of UreA2B2 incubated briefly (<2 min) with increasing concentrations of urea prior to analysis (Figure 5.13). The spectra showed a gradual shift toward a nearly complete downshift of the mode with increasing concentrations. My studies point to this shift being caused by urea binding at the metallocenter of UreA2B2, so this can be used as a rough assessment for the K_d of urea for oxidized UreA2B2. From this study, an estimated K_d between 10 and 30 mM urea was estimated. However, we later learned around 10 minutes of incubation is required for a complete downshift of the ν_s(Fe(III)-O-Fe(III)) mode at 2 mM urea. Thus, this study would have to be repeated with a longer incubation time to ensure binding has reached completion. Overall, this technique presents a novel way for determining the binding constants of urea for oxidized UreA2B2.

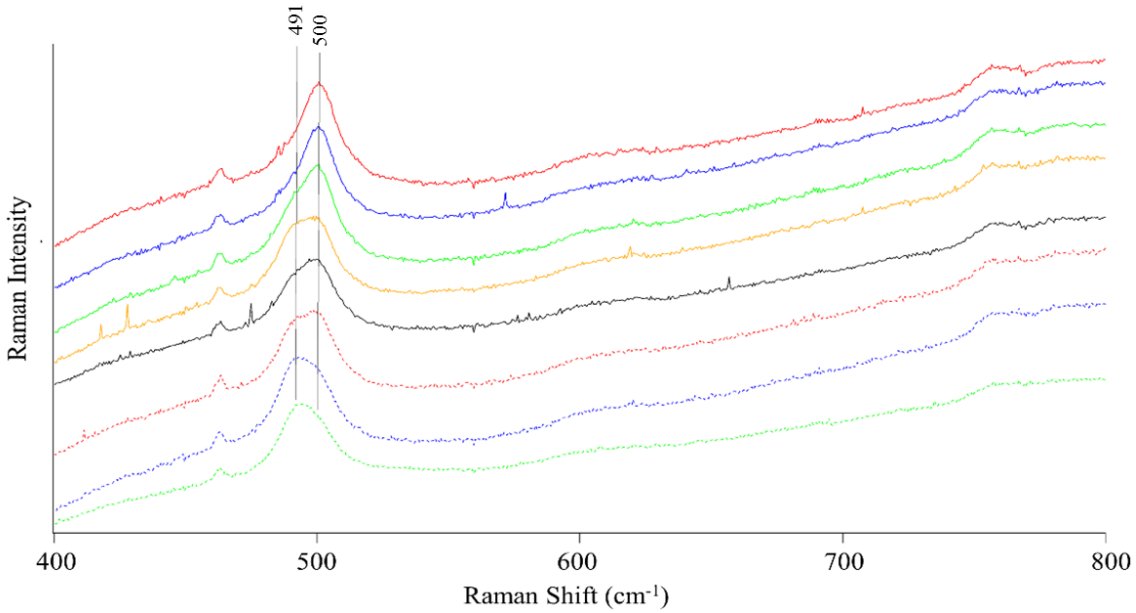

Figure 5.13: Resonance Raman spectra for samples of UreA2B2 incubated with varied concentrations of urea. 285 µM UreA2B2 was incubated with 0 (red trace), 0.1 (blue), 0.3 (green), 1 (yellow), 3 (black), 10 (red, dotted), 30 (blue, dotted), or 100 mM (green, dotted) for less than 2 minutes at room temperature before being analyzed by resonance Raman spectroscopy.

BIBLIOGRAPHY

BIBLIOGRAPHY

1. **Boer, J. L., Quiroz-Valenzuela, S., Anderson, K. L., and Hausinger, R. P.** 2010. Mutagenesis of *Klebsiella aerogenes* UreG to probe nickel binding and interactions with other urease-related proteins. Biochemistry **49**: 5859-5869.

2. **Bridgewater, J. D., Lim, J., and Vachet, R. W.** 2006. Transition metal-peptide binding studied by metal-catalyzed oxidation reactions and mass spectrometry. Anal. Chem. **78**: 2432-2438.

3. **Bridgewater, J. D., Lim, J., and Vachet, R. W.** 2006. Using metal-catalyzed oxidation reactions and mass spectrometry to identify amino acid residues within 10 Å of the metal in Cu-binding proteins. J. Am. Soc. Mass. Spectrom. **17**: 1552-1559.

4. **Breitenbach, J. M., and Hausinger, R. P.** 1988. *Proteus mirabilis* urease. Partial purification and inhibition by boric acid and boronic acid. Biochem. J. **250**:917-920.

5. **Carter, E. L.** 2012. Investigations into urease maturation and metal ion selectivity. Michigan State Univeristy, East Lansing, MI.

6. **Carter, E. L., and Hausinger, R. P.** 2010. Characterization of the *Klebsiella aerogenes* urease accessory protein UreD in fusion with the maltose binding protein. J. Bacteriol. **192**: 2294-2304.

7. **Carter, E. L., Proshlyakov, D. A., and Hausinger, R. P.** 2012. Apoprotein isolation and activation, and vibrational structure of the *Helicobacter mustelae* iron urease. J. Inorg. Biochem. **111**: 195-202.

8. **Chang, Z., Kuchar, J., and Hausinger, R. P.** 2004. Chemical cross-linking and mass spectrometric identification of sites of interaction for UreD, UreF, and urease. J. Biol. Chem. **279**: 15305-15313.

9. **Colpas, G. J., Brayman, T. G., Ming, L. J., and Hausinger, R. P.** 1999. Identification of metal-binding residues in the *Klebsiella aerogenes* urease nickel metallochaperone, UreE. Biochemistry **38**: 4078-4088.

10. **Davydov, R., Kuprin, S., Graslund, A., and Ehrenberg, A.** 1994. Electron paramagnetic resonance study of the mixed-valent diiron center in *Escherichia coli* ribonucleotide reductase produced by reduction of radical-free protein R2 at 77 K. J. Am. Chem. Soc. **116**: 11120-11128.

11. **Davydov, R., Sahlin, M., Kuprin, S., Graslund, A., and Ehrenberg, A.** 1996. Effect of the tyrosyl radical on the reduction and structure of the *Escherichia coli* ribonucleotide reductase protein R2 diferric site as probed by EPR on the mixed-valent state. Biochemistry **35**: 5571-5576.

12. **Davydov, R. M., Smieja, J., Dikanov, S. A., Zang, Y., Que, L., Jr., and Bowman, M. K.** 1999. EPR properties of mixed-valent μ-oxo and μ-hydroxo dinuclear iron complexes produced by radiolytic reduction at 77 K. J. Biol. Inorg. Chem. **4**: 292-301.

13. **Dewitt, J. G., Bentsen, J. G., Rosenzweig, A. C., Hedman, B., Green, J., Pilkington, S., Papaefthymiou, G. C., Dalton, H., Hodgson, K. O., and Lippard, S. J.** 1991. X-Ray absorption, Mössbauer, and EPR studies of the dinuclear iron center in the hydroxylase component of methane monooxygenase. J. Am. Chem. Soc. **113**: 9219-9235.

14. **Farrugia, M. A., Han, L., Zhong, Y., Boer, J. L., Ruotolo, B. T., and Hausinger, R. P.** 2013. Analysis of a soluble $(UreD:UreF:UreG)_2$ accessory protein complex and its interactions with *Klebsiella aerogenes* urease by mass spectrometry. J. Am. Soc. Mass. Spectrom. **24**: 1328-1337.

15. **Fong, Y. H., Wong, H. C., Chuck, C. P., Chen, Y. W., Sun, H., and Wong, K. B.** 2011. Assembly of preactivation complex for urease maturation in *Helicobacter pylori*: crystal structure of UreF-UreH protein complex. J. Biol. Chem. **286**: 43241-43249.

16. **Fong, Y. H., Wong, H. C., Yuen, M. H., Lau, P. H., Chen, Y. W., and Wong, K. B.** 2013. Structure of UreG/UreF/UreH complex reveals how urease accessory proteins facilitate maturation of *Helicobacter pylori* urease. PLoS Biol. **11**: e1001678.

17. **Grossoehme, N. E., Mulrooney, S. B., Hausinger, R. P., and Wilcox, D. E.** 2007. Thermodynamics of Ni^{2+}, Cu^{2+}, and Zn^{2+} binding to the urease metallochaperone UreE. Biochemistry **46**: 10506-10516.

18. **Jabri, E., Carr, M. B., Hausinger, R. P., and Karplus, P. A.** 1995. The crystal structure of urease from *Klebsiella aerogenes*. Science **268**: 998-1004.

19. **Merloni, A., Dobrovolska, O., Zambelli, B., Agostini, F., Bazzani, M., Musiani, F., and Ciurli, S.** 2014. Molecular landscape of the interaction between the urease accessory proteins UreE and UreG. Biochim. Biophys. Acta **1844**: 1662-1674.

20. **Moncrief, M. B., and Hausinger, R. P.** 1997. Characterization of UreG, identification of a UreD-UreF-UreG complex, and evidence suggesting that a nucleotide-binding site in UreG is required for *in vivo* metallocenter assembly of *Klebsiella aerogenes* urease. J. Bacteriol. **179**: 4081-4086.

21. **Park, I. S., Carr, M. B., and Hausinger, R. P.** 1994. *In vitro* activation of urease apoprotein and role of UreD as a chaperone required for nickel metallocenter assembly. Proc. Natl. Acad. Sci. U.S.A. **91**: 3233-3237.

22. **Park, I. S., and Hausinger, R. P.** 1995. Evidence for the presence of urease apoprotein complexes containing UreD, UreF, and UreG in cells that are competent for *in vivo* enzyme activation. J. Bacteriol. **177**: 1947-1951.

23. **Quiroz-Valenzuela, S., Sukuru, S. C., Hausinger, R. P., Kuhn, L. A., and Heller, W. T.** 2008. The structure of urease activation complexes examined by flexibility analysis, mutagenesis, and small-angle X-ray scattering. Arch. Biochem. Biophys. **480**: 51-57.

24. **Real-Guerra, R., Staniscuaski, F., Zambelli, B., Musiani, F., Ciurli, S., and Carlini, C. R.** 2012. Biochemical and structural studies on native and recombinant *Glycine max* UreG: a detailed characterization of a plant urease accessory protein. Plant Mol. Biol. **78**: 461-475.

25. **Srikanth, R., Wilson, J., Burns, C. S., and Vachet, R. W.** 2008. Identification of the copper(II) coordinating residues in the prion protein by metal-catalyzed oxidation mass spectrometry: evidence for multiple isomers at low copper(II) loadings. Biochemistry **47**: 9258-9268.

26. **Todd, M. J., and Hausinger, R. P.** 1989. Competitive inhibitors of *Klebsiella aerogenes* urease. Mechanisms of interaction with the nickel active site. J. Biol. Chem. **264**: 15835-15842.

27. **Weatherburn, M. W.** 1967. Phenol-hypochlorite reaction for determination of ammonia. Anal. Chem. **39**: 971-974.

CHAPTER 6

Concluding remarks

CONCLUDING REMARKS

My dissertation provides insights into the interactions of the accessory proteins with urease, the role of UreD in the activation of urease, the mechanism of urease activation, and the spectroscopic properties of the oxidized UreA2B2 metallocenter. These studies pave the way for additional investigations by other researchers. Below, I summarize my results in greater detail and describe potential future studies that could be performed.

My analyses of the $(MBP\text{-}UreDFG)_2$ complex and its interaction with urease are described in Chapters 2 and 5. This work detailed the purification and characterization of a soluble dimer of heterotrimeric urease accessory protein complex from *Klebsiella aerogenes* and identified the GTP-dependent conditions that result in the dissociation of UreG. Of great importance, ion mobility mass spectrometry was used to demonstrate the complex dissociates to a monomer of heterotrimers on binding to urease. At this time, no studies have identified whether dimerization of the heterotrimer is functionally important. Prior studies on *Helicobacter pylori* $(UreH:UreF:UreG)_2$ had identified Tyr183 as a residue required for the formation of the dimer of heterotrimers (3), and in that case urease activation was hindered with the variant protein. Future efforts could create an MBP-UreD:UreF(Y155D):UreG complex (where Tyr155 is homologous to Tyr184 in *Hp*UreF), and this purified species could be used to characterize its ability to form a dimer of heterotrimers, test if it activates urease *in vivo*, and ascertain whether stability is affected in the presence of $GTP/Mg^{2+}/Ni^{2+}$. My mutagenesis studies to substitute individual surface residues of UreD, described in Chapter 3, did not prove to be useful for mapping interactions surfaces, but this issue remains a point of interest. Additional future studies can use the soluble accessory protein complex with wild-type components along with urease to explore the urease:accessory protein interfacial site. Prior experiments identified cross-links

between UreB:UreD and UreD:UreC (2), and small angle X-ray scattering studies provided evidence that UreD binds at the vertices of the triangular $(UreABC)_3$ (4). I propose the use of hydrogen/deuterium exchange mass spectrometric studies for characterizing the exposed surfaces of UreABC apoprotein, MBP-UreD, MBP-UreDFG, UreABC:MBP-UreD, and UreABC:MBP-UreDFG. A reduction in deuterium exchange into specific residues of urease or MBP-UreD for the complexes versus the non-complexed proteins would identify the potential binding site, which could be further characterized by mutagenesis studies.

Chapter 3 defines a clear nickel-transfer role for UreD in the activation of urease and provides evidence for a buried water tunnel being used for this purpose. While the evidence presented in this chapter is strong, it does not address the identity of any nickel-coordinating residues. To this end, one could compare the nickel-binding properties of wild-type and variant forms of MBP-UreD (specifically the UreD variants that affect urease activation) by X-ray absorption spectroscopy for changes in coordination number or ligating residues. Variants found to have changes could be further studied to characterize nickel binding affinity and the number of bound nickels per MBP-UreD via equilibrium dialysis or isothermal titration calorimetry. The effects of UreD substitutions on urease activation *in vitro* should also be investigated to determine if these changes affect the rate of activation or increase the susceptibility toward contaminating metals. Finally, the feasibility of the water tunnel functioning in cation transfer is not fully addressed in Chapter 3. Ongoing studies by our collaborators in the Feig group are performing *in silico* molecular dynamics studies of the wild-type UreD homology model and the variant proteins. Additional analysis could examine the energetics of a transfer tunnel using the optimized UreD homology model to estimate whether nickel transfer is energetically favored and which portions of the protein lead to energetic barriers. I recognize the hazards with carrying out

such simulations on a homology model, but at this time we don't have a crystal structure coordinates of the protein.

The studies on UreA2B2 in Chapters 4 and 5 provide more information on the oxidized site of iron urease, but several aspects of the metallocenter were not fully addressed. The assignment of a terminal Fe-OH stretch for the $D_2O/H_2{}^{18}O$-sensitive feature at ~530 cm^{-1} could be strengthened by repeating these studies at varied pH, based on the assumption that low pH studies may result in the loss of this feature due to protonation. The issue of protein precipitation was noted in Chapter 4 at lower (6.4) and higher (9.4) pH, but this problem can be circumvented by using rapid pH changes with concentrated buffers at the desired final pH. The observation that phenyl phosphorodiamidate (PPD), but not acetohydroxamic acid, causes a downshift in the 500 cm^{-1} feature gives evidence that PPD coordinates to the diferric site of UreA2B2 in a manner similar to urea, but this interpretation needs to be further explored. Rapid bulk-solvent exchange of ^{16}O- or ^{18}O-bridged UreA2B2 can be undertaken in the absence or presence of PPD or urea and analyzed by resonance Raman spectroscopy to determine if the observed isotopic-solvent sensitivities are similar between the molecules or if they differ. A loss of the terminal solvent mode would imply the binding of PPD in oxidized UreA2B2 adopts a similar orientation to that of PPD shown in the *Sporosarcina pasteurii* structure (1), while it also gives evidence that urea-binding does not result in the displacement of terminal waters at both irons of the metallocenter.

In total, my results have led to significant advances in understanding of both the conventional nickel urease activation machinery and the spectroscopic properties of iron urease. Nevertheless, many questions about these systems remain to be answered and investigations to extend our understanding of urease and its activation remain an exciting area for future research.

BIBLIOGRAPHY

BIBLIOGRAPHY

1. **Benini, S., Rypniewski, W. R., Wilson, K. S., Miletti, S., Ciurli, S., and Mangani, S.** 1999. A new proposal for urease mechanism based on the crystal structures of the native and inhibited enzyme from *Bacillus pasteurii*: why urea hydrolysis costs two nickels. Structure **7**: 205-216.

2. **Chang, Z., Kuchar, J., and Hausinger, R. P.** 2004. Chemical cross-linking and mass spectrometric identification of sites of interaction for UreD, UreF, and urease. J. Biol. Chem. **279**: 15305-15313.

3. **Fong, Y. H., Wong, H. C., Yuen, M. H., Lau, P. H., Chen, Y. W., and Wong, K. B.** 2013. Structure of UreG/UreF/UreH complex reveals how urease accessory proteins facilitate maturation of *Helicobacter pylori* urease. PLoS. Biol. **11**: e1001678.

4. **Quiroz-Valenzuela, S., Sukuru, S. C., Hausinger, R. P., Kuhn, L. A., and Heller, W. T.** 2008. The structure of urease activation complexes examined by flexibility analysis, mutagenesis, and small-angle X-ray scattering. Arch. Biochem. Biophys. **480**: 51-57.

APPENDIX

Table A.1: Plasmids used in this dissertation.

Plasmid used	Description	Source
pUC8	High-copy number, pBR322-derived vector conferring *Amp*^{R}	(6)
pKK17	Wild-type *K. aerogenes* urease cluster (*ureDABCEFG*) placed into pKK223-3	(5)
pKK17D*, -V37L, -Y42D, -E46A, -E46Q, -C48A, -H49A, -H54A, -I59Y, -D63A, -D63Q, -L65I, -L65W, -S85K, -K86A, -Y88V, -Y88F, -R89A, -W111Y, -T128E, -D142A, -R148M, -E153A, -E153Q, -R163A, -E165A, -D169A, -E176A, -E176Q, -T196K, -R211A, -R233A	EcoRI-AgeI *5'UTR-ureD* fragment from pMF001L* ligated into similarly digested pKK17	This work
pKKG	PstI-KpnI *ureG*$_{Str}$ fragment ligated into similarly digested pKK17 resulting in replacement of UreG with one containing a *C*-terminal *Strep*-tag II (*ureDABCEFG*$_{Str}$)	(2)
pKKD*G, -D63A, -D63Q. –S85K, -D142A, -E176A, -E176Q, R211A	EcoRI-AgeI *5'UTR-ureD* fragment from pMF001L* ligated into similarly digested pKKG	This work
pEC002	pMAL-c2X derived vector for the overproduction of maltose binding protein fused at the *N*-terminus of UreD	(3)
pEC005	KpnI-XbaI *ureFG* fragment cloned into similarly digested pACT3	(3)
pEC005-UreF-K165A	Single-site mutation of pEC005 that encodes the K165A variant of UreF along with UreG	(1)
pMF001	EcoRI-HindIII *ureD* fragment from pEC002 ligated into similarly digested pUC8	This work
pMF001L	EcoRI-AgeI *5'UTR-ureD* fragment from pKK17 ligated into similarly digested pMF001	This work
pEC015	BamHI-PstI *ureA2B2* fragment cloned into similarly digested pEXT20	(4)

BIBLIOGRAPHY

BIBLIOGRAPHY

1. **Boer, J. L., and Hausinger, R. P.** 2012. *Klebsiella aerogenes* UreF: identification of the UreG binding site and role in enhancing the fidelity of urease activation. Biochemistry **51**: 2298-2308.

2. **Boer, J. L., Quiroz-Valenzuela, S., Anderson, K. L., and Hausinger, R. P.** 2010. Mutagenesis of *Klebsiella aerogenes* UreG to probe nickel binding and interactions with other urease-related proteins. Biochemistry **49**: 5859-5869.

3. **Carter, E. L., and Hausinger, R. P.** 2010. Characterization of the *Klebsiella aerogenes* urease accessory protein UreD in fusion with the maltose binding protein. J. Bacteriol. **192**: 2294-2304.

4. **Carter, E. L., Tronrud, D. E., Taber, S. R., Karplus, P. A., and Hausinger, R. P.** 2011. Iron-containing urease in a pathogenic bacterium. Proc. Natl. Acad. Sci. U.S.A. **108**: 13095-13099.

5. **Colpas, G. J., Brayman, T. G., Ming, L. J., and Hausinger, R. P.** 1999. Identification of metal-binding residues in the *Klebsiella aerogenes* urease nickel metallochaperone, UreE. Biochemistry **38**: 4078-4088.

6. **Vieira, J. and Messing, J.** 1982. The pUC plasmids, an M13mp7-derived system for insertion mutagenesis and sequening with synthetic universal primers. Gene **19**: 259-68.